Winter 12-7-2015

Ellipsometric Characterization of Silicon and Carbon Junctions for Advanced Electronics

Alexander G. Boosalis
University of Nebraska-Lincoln, alex.boosalis@huskers.unl.edu

ELLIPSOMETRIC CHARACTERIZATION OF SILICON AND CARBON JUNCTIONS FOR ADVANCED ELECTRONICS

by

Alexander George Boosalis

A DISSERTATION

Presented to the Faculty of

The Graduate College at the University of Nebraska

In Partial Fulfillment of Requirements

For the Degree of Doctor of Philosophy

Major: Electrical Engineering

Under the Supervision of Professors Mathias Schubert and Tino Hofmann

Lincoln, Nebraska

December, 2015

ELLIPSOMETRIC CHARACTERIZATION OF SILICON AND CARBON JUNCTIONS FOR ADVANCED ELECTRONICS

Alexander George Boosalis, Ph.D.

University of Nebraska, 2015

Advisers: Mathias Schubert, Tino Hofmann

Ellipsometry has long been a valuable technique for the optical characterization of layered systems and thin films. While simple systems like epitaxial silicon dioxide are easily characterized, complex systems of silicon and carbon junctions have proven difficult to analyze. Traditional model dielectric functions for layered silicon homojunctions, a system with a similar structure to modern transistors, often have correlated parameters during ellipsometric data analysis. Similarly, epitaxial graphene as grown from thermal sublimation of silicon from silicon carbide or through chemical vapor deposition, tend to have model dielectric function parameters that correlate with the optical thickness of the graphene due to its extreme thinness. In the case of highly oriented pyrolytic graphite (HOPG), the exact optical properties of the material are difficult to quantify due to an inability to perform ellipsometry measurements perpendicular to the optical axis.

It is the goal of this work to identify key methods and models appropriate for analyzing ellipsometric data including but not limited to: iso- and aniso-type silicon homojunctions, silicon carbide, epitaxial graphene, and bulk HOPG. Though a variety of models and techniques are used, the common theme of this work is the reduction of model parameters by enforcing physical models during the data fitting process. Iso-type silicon junctions were successfully characterized using terahertz to mid-infrared standard ellipsometry measurements coupled with a physically appropriate model that

enforces drift, diffusion, and depletion effects. In contrast, characterization of free charge carriers within epitaxial graphene requires use of magneto-optic generalized ellipsometry and the optical Hall effect, but allows the independent determination of the mobility, effective mass, and free charge carrier density. Characterizing epitaxial graphene and HOPG in the visible to ultra-violet spectral range requires development of a model dielectric function based on the tight binding band structure of graphene, and is verified by ellipsometry data of graphene grown by chemical vapor deposition. This model can be extended for use in analyzing HOPG phenomenologically. Alongside appropriate use of effective medium approximations, the model dielectric function for graphene developed here can be used for non-ideal samples of epitaxial graphene grown on silicon carbide.

ACKNOWLEDGMENTS

First I would like to thank my advisory committee including professors Mathias Schubert, Tino Hofmann, Natale Ianno, Peter Dowben, and Alexander Sinitskii, whose ready willingness to serve was encouraging and whose comments and questions were key to shaping this work.

Specifically I would like to thank my co-advisers, professors Mathias Schubert and Tino Hofmann. Dr. Schubert's enthusiasm in the classroom is what enticed me to become a graduate student and without his guidance and vision I might never have completed this research. Dr. Hofmann has been a continuous source of help throughout my career and whether it was through discussion of complex experiments and analysis, or simply helping design a poster, his optimism and determination made all the difference.

I am indebted to Dr. David Gundlach and Dr. Curt Richter, who gave me the opportunity to conduct some of this research at the National Institute of Standards and Technology, who pushed me to become a better scientist, and whose hospitality was always offered and always appreciated.

This work was only possible because of my collaborators who were willing to provide quality samples. I have had the opportunity to work with some of the best in the world, including:

- Dr. Kurt Gaskill, Dr. Josh Caldwell, Dr. Luke Nyakiti, Dr. Rachel Myers-Ward, and Dr. Virginia Wheeler of the Naval Research Laboratory,
- Dr. Nhan Nguyen, Dr. Wei Li, and Dr. Rand Elmquist of the National Institute of Standards and Technology,

- Dr. Rositsa Yakimova, Dr. Vanya Darakchieva, and Chamseddine Bouhafs of Linköping University in Sweden,
- Dr. Jan Šik of ON Semiconductor.

Thank you all, you have made an immense contribution.

Thanks to the J.A. Woollam company for providing excellent scientific equipment and the support to make it work. Specifically I would like to thank Dr. Craig Herzinger whose assistance with software and hardware alike was invaluable, and Ron Synowicki who performed the graphite measurements in this work.

Thanks to all my fellow graduate students; Dr. Keith Rodenhausen, Dr. Stefan Schöche, Dr. Philipp Kühne, Dr. Tadas Kasputis, Derek Sekora, Charles Rice, Chad Briley, Alyssa Mock, and Eric Montgomery, among others, for your helpful discussions and distractions!

Finally I would like to thank Sara Tangdall and my family, Pam, Deeno, and Nick Boosalis, for their love, encouragement, support, and patience during my time as a student!

GRANT INFORMATION

This work was supported by the National Institute of Standards and Technology under grant number 70NANB11H165, the U.S. Army Research Office under the small business technology transfer program (STTR) grant number A08-T013, the National Science Foundation under grant numbers MRSEC DMR-0820521, DMR-0907475, and EPS-1004094, the University of Nebraska-Lincoln, the J.A. Woollam Foundation and the J.A. Woollam Company.

Table of Contents

List of Tables

List of Figures

Chapter 1

Introduction

Silicon is perhaps the most well understood material in the world, having been the focus of transistor technology for over half a century, bringing the miniaturization of advanced electronics and the advent of commonplace computing. In contrast the two dimensional sheet of carbon known as graphene has recently become a popular research material, with applications for high-speed transistors, having been the focus of global research efforts only since the discovery of its extremely high electron mobility at room temperature [1]. However, graphene has more in common with silicon than being a replacement material for high-speed electronics. Thermally grown silicon dioxide on silicon is the most common choice as a transfer substrate for epitaxial graphene [2, 3], and remains a popular test bed for conducting experiments on all types of graphene (see references 4–8, for examples). Epitaxial graphene is also commonly grown by thermal sublimation of silicon from silicon carbide [9–14], linking the development of graphene based electronics directly to silicon based electronics once again. Silicon carbide is itself under research as a suitable material for high-power electronics. Graphene and silicon carbide can be easily envisioned in a multitude of tomorrow's electronics from devices as simple as liquid crystal displays with silicon carbide front panels and graphene based transparent conductors, to high-speed gra-

phene transistors supported by silicon logic and silicon carbide based power delivery. Either way research efforts and industrial scale development hinge on the ability to accurately characterize complex silicon and silicon carbide structures, and atomically thin epitaxial graphene devices. Complete electronic and morphological optical characterization would prove an invaluable tool for production of advanced carbon and silicon based electronics, as it would provide a non-contact measurement method that can be directly integrated into both laboratory and industrial facilities.

Spectroscopic ellipsometry is a proven technique for determining the thickness, morphology, and dielectric response of thin films [15–17], and is an ideal characterization tool for complex silicon and carbon devices. Light based characterization is in general preferable to intrusive characterization methods like spreading resistance profiling or transmission electron microscopy, which require destruction of the sample in order to perform an experiment. Ellipsometry has several advantages over other light based characterization techniques. Traditional transmission and reflection experiments require both values to be measured in order to produce similar results to standard spectroscopic ellipsometry experiments, and cannot approach the wealth of information produced by a generalized ellipsometry experiment. Ellipsometry measures the change in polarization induced by a reflection from or transmission through a sample, with the analysis conducted under the assumption that the sample is comprised of plane parallel interfaces between layers of uniform materials. In this context ellipsometry is an ideal technique for the non-invasive characterization of two-dimensional graphene, or complex stratified layers of silicon carbide or silicon. Chapter 2 focuses on the necessary mathematical background to describe polarization states, the dielectric response to an impinging electromagnetic wave, and specifics on performing and analyzing the results of spectroscopic ellipsometry measurements. Because new methods of ellipsometric data analysis are presented in this work, techniques which

can validate or invalidate the ellipsometry results. Corroborative experiments include spreading resistance profiling, low energy electron microscopy, and low energy electron diffraction, all of which are also described in chapter 2.

Complex silicon based devices are ubiquitous, but one particular structure, the iso-type homojunction, has been diffcult to both model and measure. Iso-type homojunctions are composed of a doped material mated to the same material with the same doping, but with a differing density of free charge carriers. Ideally both free charge carriers and the related dopant ions would be locked into their specific layers. In reality drift and diffusion processes balance to create a controlled spill of charge carriers from high to low density. Chapter 3 investigates how mid-infrared and terahertz frequency generalized ellipsometry can characterize both iso-type and aniso-type homojunctions in a single device without the need for destructive spreading resistance profiling. Terahertz frequencies are especially useful for this task, since the dielectric response of free charge carriers is largest at lower frequency [18]. To this end a custom terahertz frequency ellipsometer was developed, with the layout and operation shown in chapter 2.

The custom terahertz frequency instrumentation is also useful for characterizing the free charge carriers present within a graphene mono-layer, as demonstrated in chapter 4. Rather than focus on characterizing a complex structure, chapter 4 utilizes generalized ellipsometry measurements to determine the concentration, mobility, and effective mass of charge carriers within an epitaxial graphene layer. Not only is this technique non-contact and non-destructive, but by leveraging the optical Hall effect the concentration, mobility, and effective mass of free charge carriers can be determined within a single measurement.

Infrared ellipsometry is a useful tool for characterizing large structures and free charge carrier response, but is less useful in characterizing the morphology of mono-

atomic films like graphene, or interpreting their band structure. In the visible to vacuum-ultra-violet spectral range, sensitivity of an ellipsometry experiment to the morphology of nano-scale films is enhanced with the decreasing wavelength of the probe beam. Features of the band structure can also be identified, such as the two dimensional saddle point present at the **M**-point in the graphene band structure [19]. By monitoring this critical point, as it is expressed in the dielectric function of graphene, we hope to determine the number of graphene layers present and make an estimate the quality of epitaxial graphene layers. Chapter 5 investigates the dielectric response of epitaxial graphene as grown by sublimation of silicon from 3C, and the silicon and carbon faces of 4H silicon carbide, and attempts to identify causes for discrepancies in the dielectric response of the samples.

Chapter 5 attempts to analyze the dielectric response of epitaxial graphene with the framework of dual oscillators in the line-shape of a saddle point in the band structure. Several non-idealities were introduced in chapter 5 in order to deal with the particular morphology of epitaxial graphene as grown on silicon carbide. Chapter 6 attempts to derive a model dielectric function for graphene based on the tight-binding band structure with a perturbation in the probability added to account for excitonic absorption. Using a model with physically relevant parameters allows exposes the causes of the non-idealities introduced in chapter 5. Epitaxial graphene grown by chemical vapor deposition and transfered to a fused silica substrate serves as an ideal graphene sample, which is compared to highly ordered pyrolitic graphite serving as an ideal bulk sample. The goal of this investigation is to identify physically relevant parameters which can be used to characterize the number of layers, strain, and overall quality of an epitaxial graphene sample.

Building off of the results of chapter 6, chapter 7 explores the limitations of the band structure based model dielectric function for graphene as applied to epitaxial

graphene grown from 3C silicon carbide. The chaotic nature of epitaxial graphene on silicon carbide is a challenge for visible to ultra-violet spectrum ellipsometry measurements which is extremely sensitive to morphological changes in the graphene structure. Ultimately spectroscopic ellipsometry mapping is needed to fully characterize the carbon thin film. Low energy electron diffraction and microscopy experiments are used to verify the ellipsometry results.

Chapter 2

Techniques, Data Acquisition, and Analysis

2.1 Spectroscopic Ellipsometry

Spectroscopic ellipsometry is an optical technique which determines the relative change of the polarization state of electromagnetic plane waves upon reflection from or transmission through a sample. The polarization state is defined by the orthogonal, complex, and periodic electric field amplitudes E_p and E_s*, as shown in figure 2.1.

In general, spectroscopic ellipsometry data depend on a variety of parameters. For

*The letters p and s stand for "*parallel*" and "*senkrecht*" (German for parallel and perpendicular, respectively), and refer to the directions with respect to the plane of incidence.

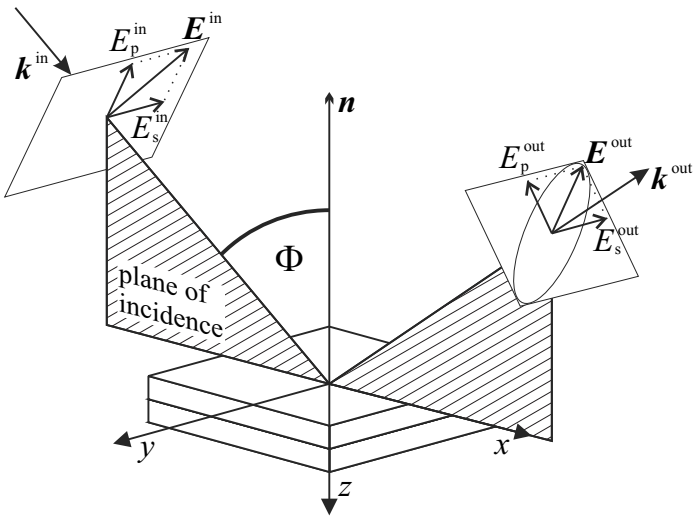

Figure 2.1: The wavevector $\mathbf{k}^{\text{in}}$ of the incoming electromagnetic plane wave and the sample normal $\mathbf{n}$ define the angle of incidence Φ and the plane of incidence. The amplitudes of the electric field of the incoming $\mathbf{E}^{\text{in}}$ and the reflected $\mathbf{E}^{\text{out}}$ plane wave, can be decomposed into complex field amplitudes E_p^{in}, E_s^{in}, E_p^{out} and E_s^{out}, where the indices p and s stand for parallel and perpendicular to the plane of incidence, respectively.

layered samples with parallel interfaces, parameters can be the photon energy $E = \hbar\omega$ of the incoming plane electromagnetic wave, the angle incidence Φ, the dielectric tensor $\boldsymbol{\varepsilon}$ and the thickness d of each layer, the interface and surface roughness, the order of the layers, the external magnetic field $\mathbf{B}$, the sample temperature T, etc. To determine physically relevant parameters from ellipsometric data of non-depolarizing samples with plane-parallel, optically homogeneous layers, non-linear model calculations are needed. Spectroscopic ellipsometry data analysis is based on the 4×4 matrix formalism, where a thickness d and a dielectric tensor $\boldsymbol{\varepsilon}$ is assigned to each layer of the sample model layer stack.

There are two major types of spectroscopic ellipsometry that are widely applied in industry and the scientific community, standard ellipsometry and generalized ellipsometry. Standard ellipsometry determines two parameters (Ψ, Δ), which provide sufficient information to fully characterize sample induced changes in the polarization state, as long as the sample does not convert p- into s-polarized light or vice versa (see section 2.1.4). If the impingent electromagnetic plane waves interact with an anisotropic sample such that the dielectric tensor possesses non-vanishing off-diagonal elements, p-s-polarization mode-conversion will occur and standard ellipsometry can no longer describe the change in the polarization state. In this case generalized ellipsometry must be used. Generalized ellipsometry data can be represented in terms of the Jones or the Mueller matrix. Every Jones matrix can be converted into a Mueller matrix but the inversion is not always possible, as depolarization cannot be represented in terms of the Jones matrix.

2.1.1 Dielectric Functions and Tensors

In the case of a bulk isotropic sample the final polarization state ($E_p^{out},\ E_s^{out}$) shown in figure 2.1 can be determined if the angle of incidence Φ of the incoming electromagnetic wave and input polarization ($E_p^{in},\ E_s^{in}$) are known. Basic knowledge of Maxwell's equations to establish boundary conditions and Snell's law can be applied to determine the relationship between the incoming and reflected wave amplitudes, commonly called the Fresnel reflection coefficients [20]. The complex Fresnel reflection coefficients for this case can be expressed as [17]:

$$r_p \equiv \left(\frac{E_p^{out}}{E_p^{in}}\right) = \frac{\varepsilon\cos\Phi - (\varepsilon - \sin^2\Phi)^{1/2}}{\varepsilon\cos\Phi + (\varepsilon - \sin^2\Phi)^{1/2}},$$
$$r_s \equiv \left(\frac{E_s^{out}}{E_s^{in}}\right) = \frac{\cos\Phi - (\varepsilon - \sin^2\Phi)^{1/2}}{\cos\Phi + (\varepsilon - \sin^2\Phi)^{1/2}}. \tag{2.1}$$

The last unknown is then the dielectric function of the material ε, making this the ideal starting point for our introduction of spectroscopic ellipsometry as a technique.

The dielectric function $\varepsilon(\omega)$ or dielectric tensor $\boldsymbol{\varepsilon}$ is a measure for the optical response of a medium, and can be defined by the electric displacement field $\mathbf{D}$, which is an auxiliary quantity used in the Maxwell equations. The electric displacement field describes the electric flux density at the surface of a medium, and can be written as

$$\mathbf{D} = \varepsilon_0\mathbf{E} + \mathbf{P} = \varepsilon_0\mathbf{E} + \boldsymbol{\chi}\mathbf{E} = \varepsilon_0\left(\mathbf{I} + \boldsymbol{\chi}\right)\mathbf{E} = \varepsilon_0\boldsymbol{\varepsilon}\mathbf{E}\ , \tag{2.2}$$

where ε_0, $\mathbf{E}$, $\mathbf{P}$, and $\boldsymbol{\chi}$ denote the electric vacuum permittivity, the electric field vector, the electric polarization vector and the electric susceptibility tensor of the medium, respectively. If the optical response of the material is linear, the total dielectric tensor

can be written as the sum of electric susceptibility tensors

$$\boldsymbol{\varepsilon} = \mathbf{I} + \boldsymbol{\chi} = \mathbf{I} + \sum_k \boldsymbol{\chi}_k \ , \tag{2.3}$$

where each $\boldsymbol{\chi}_k$ describes an independent mechanism of polarization within the medium, such as phonon modes or electronic transitions. The electric susceptibility and dielectric tensor are second-rank tensors. In general, in Cartesian coordinates (x, y, z), the dielectric tensor takes the form

$$\boldsymbol{\varepsilon}_{x,y,z} = \begin{pmatrix} \varepsilon_{xx} & \varepsilon_{xy} & \varepsilon_{xz} \\ \varepsilon_{yx} & \varepsilon_{yy} & \varepsilon_{yz} \\ \varepsilon_{zx} & \varepsilon_{zy} & \varepsilon_{zz} \end{pmatrix} = \mathbf{I} + \begin{pmatrix} \chi_{xx} & \chi_{xy} & \chi_{xz} \\ \chi_{yx} & \chi_{yy} & \chi_{yz} \\ \chi_{zx} & \chi_{zy} & \chi_{zz} \end{pmatrix} \ . \tag{2.4}$$

Diagonalization of Dielectric Tensors

In many cases, the dielectric tensor can be diagonalized by representing it in an appropriate coordinate system (eigensystem). More general, the transformation from its eigensystem (ξ, ψ, ς) into the laboratory coordinate system (x, y, z) of independent contributions to the electric susceptibility tensor $\boldsymbol{\varepsilon}_{\xi,\psi,\varsigma} \xrightarrow{\mathbf{A}} \boldsymbol{\varepsilon}_{x,y,z}$ can be written as

$$\begin{aligned} \boldsymbol{\varepsilon}_{x,y,z} &= \mathbf{A}^{-1} \boldsymbol{\varepsilon}_{\xi,\psi,\varsigma} \mathbf{A} \\ &= \mathbf{I} + \sum_k \mathbf{A}^{-1} \begin{pmatrix} \chi_{\xi_k} & 0 & 0 \\ 0 & \chi_{\psi_k} & 0 \\ 0 & 0 & \chi_{\varsigma_k} \end{pmatrix} \mathbf{A} \ , \end{aligned} \tag{2.5}$$

where k denotes the index for each independent mechanism of polarization within the medium, $\mathbf{A}$ is the invertible coordinate transformation matrix with $(x, y, z) = \mathbf{A}(\xi, \psi, \varsigma)^{\mathrm{T}}$, and $\chi_{\xi_k}, \chi_{\psi_k}, \chi_{\varsigma_k}$ are the orthogonal electric susceptibilities of the k^{th}

independent mechanism of polarization in the corresponding eigensystem.

A special case are optically isotropic materials with $\chi_{\xi_k} = \chi_{\psi_k} = \chi_{\varsigma_k}$ (for all k). Since the transformation matrices are invertible, the dielectric tensors take the same shape in the laboratory coordinate system and the eigensystem $\boldsymbol{\varepsilon}_{x,y,z} = \boldsymbol{\varepsilon}_{\xi,\psi,\varsigma}$. Therefore the dielectric tensor can be replaced by the scalar dielectric function ε, with $\boldsymbol{\varepsilon} = \varepsilon\,\mathbf{I}$, as in the example at the beginning of section 2.1.1.

Coordinate System Rotations

Coordinate transformations by the rotation of the eigensystem using the z-x'-z''-convention* are given by

$$\mathbf{A}^{(\mathrm{R})}_{\alpha,\beta,\gamma} = \begin{pmatrix} \cos\gamma & \sin\gamma & 0 \\ -\sin\gamma & \cos\gamma & 0 \\ 0 & 0 & 1 \end{pmatrix} \begin{pmatrix} 1 & 0 & 0 \\ 0 & \cos\beta & \sin\beta \\ 0 & -\sin\beta & \cos\beta \end{pmatrix} \begin{pmatrix} \cos\alpha & \sin\alpha & 0 \\ -\sin\alpha & \cos\alpha & 0 \\ 0 & 0 & 1 \end{pmatrix} . \qquad (2.6)$$

In the z-x'-z''-convention, the first rotation is performed around the z-axis by the Euler angle α, the coordinate system is then rotated by the Euler angle β around the new x'-axis, and finally a rotation by the Euler angle γ around the new z''-axis is performed. A coordinate system transformation of an electric susceptibility tensor in diagonal form, using $\mathbf{A}^{(\mathrm{R})}_{\alpha,\beta,\gamma}$, results in an electric susceptibility and therefore a dielectric tensor with symmetric off-diagonal elements and $\varepsilon_{lm} = \varepsilon_{ml}$.

2.1.2 4×4 Matrix Formalism

As seen in section 2.1.1, samples often do not have isotropic dielectric functions but whole anisotropic dielectric tensors. Compounding this complexity, samples often

*Alternative definitions such as the z-y'-z''-convention can be used.

have multiple layers, assumed from now on to have plane parallel interfaces and finiteness only in the z direction. To continue we require a more eloquent mathematical description of how electromagnetic plane waves interact with layered samples with multiple mediums. Based on the work of Berreman [21], Schubert introduced a new 4×4 formalism [22], enabling fast numerical modeling of electromagnetic field amplitudes for arbitrary anisotropic media [17, 18, 23, 24]. In Schubert's version of the 4×4 formalism Berreman's first-order differential equation

$$\frac{\partial \mathbf{\Psi}}{\partial z} = \mathrm{i}\frac{\omega}{c}\mathbf{\Delta}_B \mathbf{\Psi} \ , \tag{2.7}$$

for the measurable electromagnetic fields components $\mathbf{\Psi} = (E_\mathrm{x}, E_\mathrm{y}, H_\mathrm{x}, H_\mathrm{y})^\mathrm{T}$, is replaced by the transfer matrix equation

$$\begin{pmatrix} E_p^\mathrm{I} \\ E_s^\mathrm{I} \\ E_p^\mathrm{R} \\ E_s^\mathrm{R} \end{pmatrix} = \mathbf{L} \begin{pmatrix} E_p^\mathrm{T} \\ E_s^\mathrm{T} \\ E_p^\mathrm{B} \\ E_s^\mathrm{B} \end{pmatrix} \ , \tag{2.8}$$

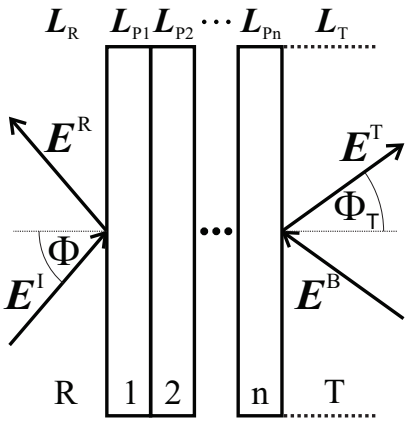

Figure 2.2: Schematic presentation of the, under the angle Φ, incoming electromagnetic wave $\mathbf{E}^\mathrm{I}$, and the reflected $\mathbf{E}^\mathrm{R}$, transmitted $\mathbf{E}^\mathrm{T}$ and back traveling electromagnetic waves $\mathbf{E}^\mathrm{B}$ used in the 4×4 matrix formalism. The medium into which the wave is reflected (transmitted) is labeled R (T). Between the media R and T, n slabs of parallel layers with homogenous optical properties are placed. Back traveling waves $\mathbf{E}^\mathrm{B}$ in the medium T are permitted.

for the electric fields amplitudes E_p (E_s) parallel (perpendicular) to the plane of incidence, of the incoming (I), reflected (R), transmitted (T) and back traveling (B) electromagnetic waves. The medium in which the reflected electromagnetic plane wave travels shall be called R, the medium in which the transmitted wave travels T. Between mediums R and T, n number of layers with parallel interfaces and homogenous optical properties are embedded. For optically isotropic media R and T*, the complex-valued 4×4 transfer matrix $\mathbf{L}$ can be expressed as the product

$$\mathbf{L} = \mathbf{L}_{\mathrm{R}}^{-1} \left(\prod_{k=1}^{n} \mathbf{L}_{\mathrm{P}k} \right) \mathbf{L}_{\mathrm{T}} \,, \tag{2.9}$$

which includes the inverse of the incident matrix $\mathbf{L}_{\mathrm{R}}$

$$\mathbf{L}_{\mathrm{R}}^{-1} = \frac{1}{2} \begin{pmatrix} 0 & 1 & -(\sqrt{\varepsilon_{\mathrm{R}}} \cos \Phi)^{-1} & 0 \\ 0 & 1 & (\sqrt{\varepsilon_{\mathrm{R}}} \cos \Phi)^{-1} & 0 \\ (\cos \Phi)^{-1} & 0 & 0 & \sqrt{\varepsilon_{\mathrm{R}}}^{-1} \\ -(\cos \Phi)^{-1} & 0 & 0 & \sqrt{\varepsilon_{\mathrm{R}}} \end{pmatrix} , \tag{2.10}$$

the partial transfer matrix of each layer k

$$\mathbf{L}_{\mathrm{P}k} = \exp(\mathrm{i} \frac{\omega}{c} \mathbf{\Delta}_k d_k) = \sum_{j=0}^{3} \beta_{jk} \mathbf{\Delta}_k^j \,, \tag{2.11}$$

and the exit matrix

$$\mathbf{L}_{\mathrm{T}} = \begin{pmatrix} 0 & 0 & \cos \Phi_{\mathrm{T}} & \cos \Phi_{\mathrm{T}} \\ 1 & 1 & 0 & 0 \\ -\sqrt{\varepsilon_{\mathrm{T}}} \cos \Phi_{\mathrm{T}} & \sqrt{\varepsilon_{\mathrm{T}}} \cos \Phi_{\mathrm{T}} & 0 & 0 \\ 0 & 0 & \sqrt{\varepsilon_{\mathrm{T}}} & \sqrt{\varepsilon_{\mathrm{T}}} \end{pmatrix} . \tag{2.12}$$

*The general case for anisotropic media can be found in Refs. [17, 18, 23, 24]

The angle Φ_{T} under which the electromagnetic plane wave is transmitted into medium T is given by

$$\cos\Phi_{\mathrm{T}} = \sqrt{1 - (\varepsilon_{\mathrm{R}}/\varepsilon_{\mathrm{T}})\sin^2\Phi}\,, \tag{2.13}$$

eventually leading to the terms in eqn. 2.1. The matrix $\mathbf{\Delta}_k$ for layer k is defined by the components of the dielectric tensor $\boldsymbol{\varepsilon}^{(k)}$ of the k^{th} layer (the index k is dropped)

$$\mathbf{\Delta} = \begin{pmatrix} -k_x\frac{\varepsilon_{zx}}{\varepsilon_{zz}} & -k_x\frac{\varepsilon_{zy}}{\varepsilon_{zz}} & 0 & 1-\frac{k_x^2}{\varepsilon_{zz}} \\ 0 & 0 & -1 & 0 \\ -\varepsilon_{yx}+\varepsilon_{yz}\frac{\varepsilon_{zx}}{\varepsilon_{zz}} & k_x^2-\varepsilon_{yy}+\varepsilon_{yz}\frac{\varepsilon_{zy}}{\varepsilon_{zz}} & 0 & k_x\frac{\varepsilon_{yz}}{\varepsilon_{zz}} \\ \varepsilon_{xx}-\varepsilon_{xz}\frac{\varepsilon_{zx}}{\varepsilon_{zz}} & \varepsilon_{xy}-\varepsilon_{xz}\frac{\varepsilon_{zy}}{\varepsilon_{zz}} & 0 & -k_x\frac{\varepsilon_{xz}}{\varepsilon_{zz}} \end{pmatrix}, \tag{2.14}$$

where $k_x = n_{\mathrm{R}}\sin\Phi$ is the projection of the wave vector of the incoming electromagnetic plane wave onto the x-axis. The complex sclars β_{jk} $(j = 0\ldots3)$ are defined by (the index k is dropped)

$$\beta_n = \sum_{j=0}^{3}\alpha_n\frac{\exp(\mathrm{i}\omega q_j(-d)/c)}{(q_j-q_k)(q_j-q_l)(q_j-q_m)}\,, \tag{2.15}$$

with the parameters

$$\begin{aligned} \alpha_0 &= -q_kq_lq_m\,, & \alpha_1 &= q_kq_l+q_kq_m+q_lq_m\,, \\ \alpha_2 &= -(q_k+q_l+q_m)\,, & \alpha_3 &= 1\,, \end{aligned} \tag{2.16}$$

with $\{k,l,m\} = \{0,1,2,3\}\setminus\{j\}$.* The four complex-valued eigenvalues of the matrix $\mathbf{\Delta}$ for layer k are denoted as q_j $(j = 0\ldots3)$. Two eigenvalues q_j, associated with the eigenmodes Ξ_j within each layer k, have positive real parts and correspond to the transmitted (forward traveling) electromagnetic plane. Accordingly, the two eigenval-

*Example: $j = 2 \rightarrow \{k,l,m\} = \{0,1,3\}$

ues with negative real parts belong to backward-traveling electromagnetic waves.

The Fresnel reflection coefficients can now be redefined as:

$$r_{pp} \equiv \left(\frac{E_p^{\text{out}}}{E_p^{\text{in}}}\right)_{E_s^{\text{in}}=0} = \frac{L_{11}L_{43} - L_{13}L_{41}}{L_{11}L_{33} - L_{13}L_{31}}\,, \qquad r_{ps} \equiv \left(\frac{E_s^{\text{out}}}{E_p^{\text{in}}}\right)_{E_s^{\text{in}}=0} = \frac{L_{33}L_{41} - L_{31}L_{43}}{L_{11}L_{33} - L_{13}L_{31}}\,,$$
$$r_{sp} \equiv \left(\frac{E_p^{\text{out}}}{E_s^{\text{in}}}\right)_{E_p^{\text{in}}=0} = \frac{L_{11}L_{23} - L_{13}L_{21}}{L_{11}L_{33} - L_{13}L_{31}}\,, \qquad r_{ss} \equiv \left(\frac{E_s^{\text{out}}}{E_s^{\text{in}}}\right)_{E_p^{\text{in}}=0} = \frac{L_{33}L_{21} - L_{31}L_{23}}{L_{11}L_{33} - L_{13}L_{31}}\,, \tag{2.17}$$

where E_p^{in}, E_s^{in}, E_p^{out} and E_s^{out} are the projections of the electric field vectors into the plane parallel (p) and perpendicular (s) to the plane of incidence of the incoming (in) and outgoing (out) wave, and are calculated from the elements L_{ij} of the transfer matrix $\mathbf{L}$ [Eqn. (2.9)].

Using the 4×4 matrix formalism it can be shown that, if the dielectric tensors of all k layers have diagonal shape $\varepsilon_{lm} = 0$ (with $l \neq m$), the off-diagonal elements of the Jones matrix vanish $r_{ps} = r_{sp} = 0$. Thus, isotropic media and anisotropic media in special measurement configurations (crystallographic or magnetic field orientations) exhibit no p-s-polarization mode-conversion. Therefore, the p-s-polarization mode-conversion describing Jones matrix ellipsometry parameters vanish $\Psi_{ps} = \Psi_{sp} = 0$. Accordingly, the elements of the off-diagonal-blocks of the Mueller matrix vanish in such cases.

2.1.3 Jones and Mueller Matrix Calculus

Jones formalism

It is clear from inspection of Eqn. 2.17 that the complex Fresnel reflection coefficients can be cast as a transition matrix $\mathbf{J}$ for the electric field vectors* $\mathbf{E}^{\text{in}}$ and $\mathbf{E}^{\text{out}}$

$$\mathbf{E}^{\text{out}} = \mathbf{J}\mathbf{E}^{\text{in}} \ . \tag{2.18}$$

The matrix $\mathbf{J}$, called Jones matrix [25], is a dimensionless, complex valued 2×2 matrix, and can be written as

$$\mathbf{J} = \begin{pmatrix} r_{pp} & r_{ps} \\ r_{sp} & r_{ss} \end{pmatrix} \ . \tag{2.19}$$

If the sample does not depolarize light, the Jones matrix represents a complete mathematical description of the reflection of a plane electromagnetic wave on a surface [23, 26, 27].

Mueller matrix formalism

Instead of electric field amplitudes, the Mueller matrix formalism describes the transformation of the polarization state of a plane electromagnetic wave based on intensities. Using intensities, the polarization state of a plane electromagnetic wave can be quantified by the real-valued Stokes vector $\mathbf{S}$. The Stokes vector has four components†, and can be expressed in terms of the p- and s-coordinate system. Its individual

*Note that electric field vectors $\mathbf{E}$ contain four independent pieces of information. The four parameters can be used to characterize the electric field amplitude, absolute phase, ellipticity and orientation of the polarization ellipse.

†Note the four independent pieces of information contained in the Stokes vector. The four parameters can be used to characterize the total light intensity, degree of polarization, ellipticity and orientation of the polarization ellipse.

components are then defined by

$$\begin{pmatrix} S_1 \\ S_2 \\ S_3 \\ S_4 \end{pmatrix} = \begin{pmatrix} I_p + I_s \\ I_p - I_s \\ I_{+45} - I_{-45} \\ I_{\sigma+} - I_{\sigma-} \end{pmatrix} = \begin{pmatrix} E_p E_p^* + E_s E_s^* \\ E_p E_p^* - E_s E_s^* \\ E_p E_s^* + E_p^* E_s \\ \mathrm{i}(E_p E_s^* - E_p^* E_s) \end{pmatrix} , \tag{2.20}$$

with I_p, I_s, I_{+45}, I_{-45}, I_{σ_+}, and I_{σ_-} being the intensities for the p-, s-, +45°, -45°, right- and left-handed circularly polarized light components, respectively [23, 28]. The Mueller matrix $\mathbf{M}$ is the transformation matrix for Stokes vectors $\mathbf{S}$ [17, 23]

$$\mathbf{S}^{\mathrm{out}} = \mathbf{M}\mathbf{S}^{\mathrm{in}} \tag{2.21}$$

where $\mathbf{S}^{\mathrm{out}}$ and $\mathbf{S}^{\mathrm{in}}$ denote the Stokes vectors of the electromagnetic plane wave before and after the transformation. The Mueller matrix is a dimensionless, real-valued 4×4 matrix

$$\mathbf{M} = \begin{pmatrix} M_{11} & M_{12} & M_{13} & M_{14} \\ M_{21} & M_{22} & M_{23} & M_{24} \\ M_{31} & M_{32} & M_{33} & M_{34} \\ M_{41} & M_{42} & M_{43} & M_{44} \end{pmatrix} . \tag{2.22}$$

The degree of depolarization* can be calculated from the matrix elements of the Mueller matrix by [29]

$$D = \frac{1}{3}(4 - D') = \frac{1}{3}(4 - \sum_{i,j}^{4} \frac{M_{ij}^2}{M_{11}^2}) , \tag{2.23}$$

with $1 \leq D' \leq 4$. If depolarization can be neglected ($D = 0$), then the Jones- and

*Note the replacement of the absolute phase information in the Jones calculus by the degree of polarization in the Mueller calculus.

Mueller matrix formalisms are equivalent.

Mathematical relations between Jones and Mueller matrix

Each Jones matrix can be converted to a Mueller matrix, but the inversion is not possible in all cases. Individual Mueller Matrix elements can be calculated from the Jones matrix by [27]

$$M_{ij} = \frac{1}{2}\mathrm{Tr}\left(\mathbf{J}\boldsymbol{\sigma}_i\mathbf{J}^\dagger\boldsymbol{\sigma}_j\right) \ , \tag{2.24}$$

where $\mathbf{J}^\dagger$ is the Hermitian conjugate of the Jones matrix, and $\boldsymbol{\sigma}_i$ is a set of 2×2 matrices comprising of the unity matrix and the Pauli matrices [27]

$$\boldsymbol{\sigma}_1 = \begin{pmatrix} 1 & 0 \\ 0 & 1 \end{pmatrix} \ , \qquad \boldsymbol{\sigma}_2 = \begin{pmatrix} 1 & 0 \\ 0 & -1 \end{pmatrix} \ , \qquad \boldsymbol{\sigma}_3 = \begin{pmatrix} 0 & 1 \\ 1 & 0 \end{pmatrix} \ , \qquad \boldsymbol{\sigma}_4 = \begin{pmatrix} 0 & -\mathrm{i} \\ \mathrm{i} & 0 \end{pmatrix} \ . \tag{2.25}$$

The resulting Mueller matrix can be expressed as the sum of two matrices

$$\mathbf{M} = \mathbf{M}_{\mathrm{iso}} + \mathbf{M}_{\mathrm{an}} \ , \tag{2.26}$$

with the isotropic Mueller matrix $\mathbf{M}_{\mathrm{iso}}$ including all terms independent of r_{ps} and r_{sp}

$$\mathbf{M}_{\mathrm{iso}} = \begin{pmatrix} \frac{1}{2}\left(r_{pp}r_{pp}^* + r_{ss}r_{ss}^*\right) & \frac{1}{2}\left(r_{pp}r_{pp}^* - r_{ss}r_{ss}^*\right) & 0 & 0 \\ \frac{1}{2}\left(r_{pp}r_{pp}^* - r_{ss}r_{ss}^*\right) & \frac{1}{2}\left(r_{pp}r_{pp}^* + r_{ss}r_{ss}^*\right) & 0 & 0 \\ 0 & 0 & \Re\mathrm{e}\left(r_{pp}r_{ss}^*\right) & \Im\mathrm{m}\left(r_{pp}r_{ss}^*\right) \\ 0 & 0 & -\Im\mathrm{m}\left(r_{pp}r_{ss}^*\right) & \Re\mathrm{e}\left(r_{pp}r_{ss}^*\right) \end{pmatrix} , \tag{2.27}$$

and the anisotropic Mueller matrix $\mathbf{M}_{\text{an}}$ including all p-s polarization mode-conversion effects

$$\mathbf{M}_{\text{an}} = \begin{pmatrix} \frac{1}{2}\left(r_{ps}r_{ps}^{*} + r_{sp}r_{sp}^{*}\right) & -\frac{1}{2}\left(r_{ps}r_{ps}^{*} - r_{sp}r_{sp}^{*}\right) & \Re\mathrm{e}\left(r_{pp}r_{ps}^{*} + r_{ss}r_{sp}^{*}\right) & \Im\mathrm{m}\left(r_{pp}r_{ps}^{*} - r_{ss}r_{sp}^{*}\right) \\ \frac{1}{2}\left(r_{ps}r_{ps}^{*} - r_{sp}r_{sp}^{*}\right) & -\frac{1}{2}\left(r_{ps}r_{ps}^{*} + r_{sp}r_{sp}^{*}\right) & \Re\mathrm{e}\left(r_{pp}r_{ps}^{*} - r_{ss}r_{sp}^{*}\right) & \Im\mathrm{m}\left(r_{pp}r_{ps}^{*} + r_{ss}r_{sp}^{*}\right) \\ \Re\mathrm{e}\left(r_{pp}r_{sp}^{*} + r_{ss}r_{ps}^{*}\right) & \Re\mathrm{e}\left(r_{pp}r_{sp}^{*} - r_{ss}r_{ps}^{*}\right) & \Re\mathrm{e}\left(r_{ps}r_{sp}^{*}\right) & -\Im\mathrm{m}\left(r_{ps}r_{sp}^{*}\right) \\ -\Im\mathrm{m}\left(r_{pp}r_{sp}^{*} - r_{ss}r_{ps}^{*}\right) & -\Im\mathrm{m}\left(r_{pp}r_{sp}^{*} + r_{ss}r_{ps}^{*}\right) & -\Im\mathrm{m}\left(r_{ps}r_{sp}^{*}\right) & -\Re\mathrm{e}\left(r_{ps}r_{sp}^{*}\right) \end{pmatrix}. \tag{2.28}$$

Eqn. (2.27) and Eqn. (2.27) display that the Mueller matrix can be decomposed in 4 sub-matrices, where the matrix elements of the two off-diagonal-blocks $\begin{bmatrix} M_{13} & M_{14} \\ M_{23} & M_{24} \end{bmatrix}$ and $\begin{bmatrix} M_{31} & M_{32} \\ M_{41} & M_{42} \end{bmatrix}$ only deviate from zero if p-s-polarization mode-conversion appears *e.g.* $r_{ps} \neq 0 \vee r_{sp} \neq 0$. The matrix elements in the two on-diagonal-blocks $\begin{bmatrix} M_{11} & M_{12} \\ M_{21} & M_{22} \end{bmatrix}$ and $\begin{bmatrix} M_{33} & M_{34} \\ M_{43} & M_{44} \end{bmatrix}$ are typically non-zero and contain information about p-s-polarization mode-conserving processes.

Note that, since defined by intensities, the Stokes vectors do not contain any phase information about the electromagnetic plane wave. Therefore, the absolute phase information contained in the Jones matrix is lost in the transformation described by Eqn. (2.24), and the Mueller matrix in Eqn. (2.24) provides seven independent pieces of information [27].

Systems of optical elements

If an electromagnetic plane wave undergoes several incoherently coupled transformations, assuming the spacial separation is higher than the coherence length of the wave, the total effect on the polarization state can be expressed as the product of the Jones

or Mueller matrices of the individual transformations

$$\mathbf{J} = \prod_i \mathbf{J}_i \quad \text{and} \tag{2.29a}$$

$$\mathbf{M} = \prod_i \mathbf{M}_i \ . \tag{2.29b}$$

This is especially useful for describing interactions with multiple optical elements like polarizers, phase retarders or a sample, as found in ellipsometry measurement instrumentation. An additional transformation of the polarization state, not generated by the interaction with matter, is caused by the rotation of the ellipsometric p-s coordinate system (see section 2.1.1). Jones and Mueller matrix representation of common optical elements like polarizers, compensators, samples (here isotropic), depolarizers, and coordinate system rotations are summarized in Table 2.1*.

2.1.4 Standard Ellipsometry

In standard spectroscopic ellipsometry it is assumed that no p-s-polarization mode-conversion occurs, which is expressed as vanishing off-diagonal elements in the Jones matrix [Eqn. (2.19)] $r_{ps} = r_{sp} = 0$. Under this assumption, the relative† change of the polarization state does not depend on the polarization of the incoming plane electromagnetic wave, since the p- and s-polarized channels of the electromagnetic plane wave are independent. Standard ellipsometry provides two pieces of information, traditionally expressed by the parameters Ψ and Δ, defined by the complex-valued ratio ρ of the reflection coefficients $r_p = r_{pp}$ and $r_s = r_{ss}$

$$\rho = \frac{r_p}{r_s} = \tan\Psi \exp(\mathrm{i}\Delta) \ . \tag{2.30}$$

*With exception of the depolarizer, all elements are assumed to be ideal *e.g.* $D = 0$.

†The term "relative" indicates that the absolute phase of the incoming and outgoing wave is neglected.

Table 2.1: Jones and Mueller matrix representations of selected, ideal optical elements. The quantities Ψ and Δ are the two ellipsometric parameters used in standard ellipsometry [17]

optical element	Jones matrix representation	Mueller matrix representation
$\mathbf{P} = \mathbf{A}$: linear polarizer (analyzer) field in x-direction	$\begin{bmatrix} 1 & 0 \\ 0 & 0 \end{bmatrix}$	$\begin{bmatrix} 1 & 1 & 0 & 0 \\ 1 & 1 & 0 & 0 \\ 0 & 0 & 0 & 0 \\ 0 & 0 & 0 & 0 \end{bmatrix}$
$\mathbf{C}(\delta)$: compensator with phase shift δ	$\begin{bmatrix} 1 & 0 \\ 0 & \exp(\mathrm{i}\delta) \end{bmatrix}$	$\begin{bmatrix} 1 & 0 & 0 & 0 \\ 0 & 1 & 0 & 0 \\ 0 & 0 & \cos\delta & \sin\delta \\ 0 & 0 & -\sin\delta & \cos\delta \end{bmatrix}$
$\mathbf{R}(\theta)$: rotation of coordinate system by angle θ	$\begin{bmatrix} \cos\theta & \sin\theta \\ -\sin\theta & \cos\theta \end{bmatrix}$	$\begin{bmatrix} 1 & 0 & 0 & 0 \\ 0 & \cos 2\theta & \sin 2\theta & 0 \\ 0 & -\sin 2\theta & \cos 2\theta & 0 \\ 0 & 0 & 0 & 1 \end{bmatrix}$
$\mathbf{D}$: non absorbing depolarizer	–	$\begin{bmatrix} 1 & 0 & 0 & 0 \\ 0 & 0 & 0 & 0 \\ 0 & 0 & 0 & 0 \\ 0 & 0 & 0 & 0 \end{bmatrix}$
$\mathbf{S}$: isotropic sample	$\begin{bmatrix} \tan\Psi\exp(\mathrm{i}\Delta) & 0 \\ 0 & 1 \end{bmatrix}$	$\begin{bmatrix} 1 & -\cos(2\Psi) & 0 & 0 \\ -\cos 2\Psi & 1 & 0 & 0 \\ 0 & 0 & \sin 2\Psi\cos\Delta & \sin 2\Psi\sin\Delta \\ 0 & 0 & -\sin 2\Psi\sin\Delta & \sin 2\Psi\cos\Delta \end{bmatrix}$

If all layers of a sample are optically isotropic* and homogenous materials, standard ellipsometry provides a complete description of the relative change in the polarization state caused by the interaction with the sample.

2.1.5 Generalized Ellipsometry

If p-s polarization mode-conversion occurs, *e.g.* $r_{ps} \neq 0 \vee r_{sp} \neq 0$, the relative change in the polarization state of a electromagnetic wave depends on the polarization state of incident plane wave. Therefore, the standard ellipsometry parameters Ψ and Δ provide no longer a unique quantification of the relative change in the polarization state of the electromagnetic plane wave, and generalized ellipsometry has to be applied. Generalized ellipsometry uses either Jones matrix or Mueller matrix formalism to describe the polarization state.

For non-depolarizing samples Jones matrix ellipsometry provides a unique quantification and a complete description of the change in the polarization state†

$$\rho_{pp} = \frac{r_{pp}}{r_{ss}} = \tan\Psi_{pp}\exp(\mathrm{i}\Delta_{pp}) \;, \tag{2.31a}$$

$$\rho_{ps} = \frac{r_{ps}}{r_{pp}} = \tan\Psi_{ps}\exp(\mathrm{i}\Delta_{ps}) \;, \tag{2.31b}$$

$$\rho_{sp} = \frac{r_{sp}}{r_{ss}} = \tan\Psi_{sp}\exp(\mathrm{i}\Delta_{sp}) \;. \tag{2.31c}$$

Note that the Jones matrix [Eqn. (2.19)] contains four complex values, and therefore eight pieces of information [27]. Due to the neglect of the absolute phase and amplitude of the p- and s-polarized components of the electromagnetic wave, the ellipsometric parameters Ψ_{pp}, Δ_{pp}, Ψ_{ps}, Δ_{ps}, Ψ_{sp} and Δ_{sp} only provide six independent

*This is equivalent to p-s-polarization mode-preservation, which is the case for all sample where the dielectric tensor takes diagonal shape in the measurement configuration (see section 2.1.2).

†This definition is convenient for rotating analyzer ellipsometers [18]. An alternative definition for Eqn. (2.31b) is $\rho'_{ps} = \frac{r_{ps}}{r_{ss}} = \tan\Psi'_{ps}\exp(\mathrm{i}\Delta'_{ps}) = \rho_{ps}\rho_{pp}$ [17]

pieces of information.

For depolarizing samples Mueller matrix ellipsometry provides a unique quantification and a complete description of the change in the polarization state. Mueller matrix ellipsometry determines the Mueller matrix, or parts of the Mueller matrix [Eqn. (2.22)]. The determined elements of the Mueller matrix are typically normalized by the Mueller matrix element M_{11}.

Magneto-Optic Generalized Ellipsometry

Magneto-optic generalized ellipsometry is a specialized variant of generalized ellipsometry in which a static magnetic field ($\mathbf{B}$) is applied to the sample through the duration of the ellipsometry experiment, attempting to measure the optical Hall effect. The optical Hall effect is a physical phenomenon best described as the occurrence of transverse and longitudinal magnetic field-induced birefringence, as caused by the nonreciprocal [30] magneto-optic response of electric charge carriers. The term optical Hall effect is used similarly to the classic electrical Hall effect [31], since the electrical Hall effect and certain cases of optical Hall effect can be explained by extensions of the Drude model for the transport of electrons in matter [32]. Analysis of optical Hall effect data provides insight into the high frequency properties of free charge carriers in complex layered samples, [33–38], grants access to effective mass parameters, [36, 39–46] and can even be used to study quantum mechanical effects [47–49].

The optical Hall effect is typically quantified by wavelength dependent changes in the Mueller matrix, as measured experimentally by generalized ellipsometry. Optical Hall effect data $\mathbf{M}^{\pm}$ is hereby defined as Mueller matrix data from an optical Hall effect experiment with magnetic field $\pm\mathbf{B}$

$$\mathbf{M}^{\pm} = \mathbf{M}(\boldsymbol{\varepsilon}^{(k)}_{\mathrm{OHE}}(\pm\mathbf{B})) = \mathbf{M}(\boldsymbol{\varepsilon}^{(k)}_{\mathbf{B}=0} + \Delta\boldsymbol{\varepsilon}^{(k)}_{\pm\mathbf{B}}) \,, \tag{2.32}$$

where $\Delta\boldsymbol{\varepsilon}^{(k)}_{\pm\mathbf{B}}$ is the magnetic field induced change of the k^{th} dielectric tensors of a sample with k layers (see 4×4 matrix formalism, section 2.1.2).

Furthermore, derived optical Hall effect datasets $\delta\mathbf{M}^{\pm}$ are hereby defined as difference datasets between optical Hall effect datasets, measured at the magnetic field $\pm\mathbf{B}$, and the corresponding generalized ellipsometry datasets ($B = 0$)

$$\begin{aligned} \delta\mathbf{M}^{\pm} &= \mathbf{M}^{\pm} - \mathbf{M} \\ &= \Delta\mathbf{M}(\boldsymbol{\varepsilon}^{(k)}_{\mathbf{B}=0}, \Delta\boldsymbol{\varepsilon}^{(k)}_{\pm\mathbf{B}}) \ , \end{aligned} \tag{2.33}$$

where $\Delta\mathbf{M}(\boldsymbol{\varepsilon}^{(k)}_{\mathbf{B}=0}, \boldsymbol{\varepsilon}^{(k)}_{\pm\mathbf{B}})$ is the magnetic field induced change of the Mueller matrix. This form of presentation is in particular advantageous when the magnetic field induces only small changes in the Mueller matrix, and provides improved sensitivity to magnetic field dependent model parameters during data analysis. Another form of presentation for derived optical Hall effect data is

$$\begin{aligned} \delta\mathbf{M}^{+} \pm \delta\mathbf{M}^{-} \ &= \ \Delta\mathbf{M}(\boldsymbol{\varepsilon}^{(k)}_{\mathbf{B}=0}, \Delta\boldsymbol{\varepsilon}^{(k)}_{+\mathbf{B}}) \\ &\quad \pm\Delta\mathbf{M}(\boldsymbol{\varepsilon}^{(k)}_{\mathbf{B}=0}, \Delta\boldsymbol{\varepsilon}^{(k)}_{-\mathbf{B}}) \ , \end{aligned} \tag{2.34}$$

which can be used to inspect symmetry properties of magneto-optic Mueller matrix data, and can help to improve the sensitivity to magnetic field dependent model parameters during data analysis.

Note that all Mueller matrix elements of generalized ellipsometry datasets presented in this work are normalized by the element M_{11}, therefore $M_{11} \stackrel{!}{=} 1$, $|M_{ij}| \leq 1$, $|\delta M^{\pm}_{ij}| \leq 2$, and $\delta M^{\pm}_{11} \stackrel{!}{=} 0$

2.1.6 Data Acquisition

All of the spectroscopic ellipsometers used for data collection in this dissertation are rotating element ellipsometers; alternative ellipsometer types can be found in Ref. 23. Spectroscopic ellipsometers with rotating optical elements can be classified into three categories: [17] (i) rotating analyzer ellipsometers (RAE) [17, 50–52] in polarizer-sample-rotating-analyzer (PSA_R) or rotating-polarizer-sample-analyzer (P_RSA) configuration are capable of measuring the upper left 3×3 block of the Mueller matrix; (ii) rotating compensator ellipsometers (RCE) [17, 50, 53–56] in polarizer-sample-rotating-compensator-analyzer (PSC_RA) or polarizer-rotating-compensator-sample-analyzer (PC_RSA) configurations are capable of measuring the upper left 3×4 or 4×3 block of the Mueller matrix, respectively; (iii) multiple-rotating element ellipsometers, including the dual-rotating-compensator ellipsometer (RC2) [57, 58], which are capable of measuring the full 4×4 Mueller matrix. Each of these types is capable of performing complete standard ellipsometry measurements.

Mathematically the operation of all spectroscopic ellipsometers with rotating optical elements can be described by the ordered multiplication of either Jones or Mueller matrices [Eqn. (2.29)], corresponding to their consecutive optical elements (including the sample) and coordinate rotations [17]. The Jones and Mueller matrices of polarizers $\mathbf{P}$, analyzers $\mathbf{A}$, compensators $\mathbf{C}(\delta)$ with phase shift δ, coordinate rotations along beam path $\mathbf{R}(\theta)$ by the angle α, and of samples $\mathbf{S}$ are given in Table 2.1.

Execution of the matrix multiplication characteristic to the corresponding ellipsometer type [17] shows that, due to the rotation of optical elements, the measured intensity at the detector is periodic. Fourier analysis of the detector signal determines Fourier coefficients, which are converted into the Jones or Mueller matrix of the sample. For example, an ideal PSA_R or P_RSA ellipsometer will measure the intensity

(assuming a 45 degree incident polarization)

$$I = I_0/2(1 - \cos 2\Psi \cos 2A + \sin 2\Psi \cos \Delta \sin 2A), \tag{2.35a}$$

$$= I_0/2(1 + S_1 \cos 2A + S_2 \sin 2A), \tag{2.35b}$$

$$= I_0/2(1 + \alpha \cos 2\omega t + \beta \sin 2\omega t), \tag{2.35c}$$

such that the ellipsometry parameters Ψ and Δ, or alternatively the Stokes vector elements S_1 and S_2, can be immediately identified in terms of the Fourier coefficients α and β and the angular frequency of the analyzer rotation ω. In order to acquire the last Stokes vector element S_3, a compensator must be added to the system. With a $PSCA_R$ ellipsometer, the measured intensity has the form

$$I = I_0/2(1 + S_1 \cos 2A + (S_2 \cos \delta - S_3 \sin \delta) \sin 2A), \tag{2.36}$$

where δ is the phase shift introduced by the compensator as per Table 2.1. In order to separate S_2 from S_3 measurements must be made with two different orientations of the compensator. This can be alleviated with a rotating-compensator system. Ellipsometry is considered an intensity-independent technique, as the Fourier analysis removes any DC component and thus only the ratio of intensities I/I_0 is important, provided there is enough intensity to complete the measurement.

While it is generally better to utilize generalized ellipsometry for depolarizing samples, it is possible to find the degree of polarization using standardized ellipsometry if the ellipsometer is equipped with a compensator. The intensity equation 2.35c can then be rewritten as

$$\begin{aligned} I &\simeq w_\chi(1+\alpha\cos 2A+\beta\sin 2A)+(1-w_\chi)(1+\alpha'\cos 2A+\beta'\sin 2A) \\ &\simeq 1+\tilde{\alpha}\cos 2A+\tilde{\beta}\sin 2A \end{aligned} \tag{2.37}$$

where w_χ is the probability of measuring an intensity with Fourier parameters α and β and $(1-w_\chi)$ is the probability of measuring an intensity with Fourier parameters α' and β'. This formulation is useful for describing inhomogeneous samples. The parameters $\tilde{\alpha}$ and $\tilde{\beta}$ are related to the ellipsometry angles Ψ and Δ by

$$\tilde{\alpha}=P_\chi\frac{\tan^2\Psi-1}{\tan^2\Psi+1} \quad \text{and} \quad \tilde{\beta}=P_\chi\frac{2\tan\Psi\cos\Delta}{\tan^2\Psi+1} \tag{2.38}$$

where $P_\chi=2w_\chi-1$ is the degree of polarization, once again assuming a linear input polarization of 45 degrees. By using a PSC_RA type ellipsometer, and repeating measurements with different phase shifts introduced by the compensator as shown in equation 2.36, the degree of polarization P_χ can be found along with the ellipsometry angles Ψ and Δ. A more detailed discussion of this topic can be found in reference 16.

Commercial Instrumentation

Ellipsometric data collection within this work covers a considerable spectral range, from the terahertz to the ultraviolet. In order to accomplish this several ellipsometry instruments were used, including three manufactured by the J.A. Woollam company and listed in table 2.2. Each is in the rotating-analyzer configuration, although the IR-VASE includes a compensator to enable measurement of the first three columns of the Mueller matrix. The IR-VASE employs a silicon carbide globar as the infrared source, using a Bomem MB-100 series interferometer as a monochromator.

The M2000-D instrument is equipped with an x-y translation stage and focusing

Table 2.2: Commercial ellipsometers used for experiments, manufactured by the J.A. Woollam company.

Model Number	Photo	Type	Spectral Range	Light Source
IR-VASE gen. 1		$PSCA_R$	1,250 - 30,000 nm 0.04 - 1 eV 10 - 300 THz	SiC globar
M2000-D		PSA_R	193 - 1690 nm 6.5 - 0.75 eV 180 - 1500 THz	Xenon lamp
VUV-302		PSA_R	130 - 1650 nm 0.75 - 9.5 eV	Xenon lamp Deuterium lamp

probes that reduce the beam spot to ~150×25 µm, allowing spectroscopic ellipsometry mapping measurements at the expense of the angle of incidence being fixed at 65 degrees. This can be a significant restriction as variable angle spectroscopic ellipsometry provides additional independent information of the sample system. For visible measurements a xenon lamp is used to provide white light. In the case of the M2000-D, the white light is spectrally separated with a grating at the detector, and ultimately measured with a mapped CCD camera, enabling simultaneous spectroscopic measurement.

In the case of the VUV-302 vacuum ultraviolet ellipsometer the xenon lamp filtered through a monochromator and each wavelength is measured one at a time. A deuterium lamp is also used in the VUV-302 to provide light intensity in the ultraviolet. The VUV-302 is constantly purged with nitrogen gas in order to alleviate absorption by oxygen in the atmosphere, and consequently requires a sealed sample chamber. Note that the spectral range of each instrument overlaps with the next, allowing a direct comparison between instruments.

Custom THz Instrumentation

The custom THz frequency instrument operates in the rotating-analyzer arrangement (PSA_R) and permits ellipsometric measurements in the spectral range from 0.2 to 1.5 THz. The experimental setup is based on a θ-2θ high precision goniometer which allows for measurements at angles of incidence a from 30° to 90°. A sketch of the experimental setup is given in figure 2.3. A backward wave oscillator (BWO) is employed as the radiation source. The nearly linearly polarized light emitted from the BWO is collimated by a picarin lens. A variable odd-bounce polarization rotation system (see Ref. 59) is used in combination with a polyethylene substrate, wire-grid polarizer to control the incident polarization state. Three mirrors steer the beam and

focus the radiation to the sample stage located on the goniometer. A polyethylene substrate wire-grid polarizer constantly rotating at 0.45 Hz serves as the polarization state analyzer. The terahertz radiation reflected from the sample is focused on to a Golay cell which is used as a detector. The beam is modulated by an optical chopper at a frequency of 12.6 Hz to match the frequency response of the Golay cell.

The BWO tube used here emits nearly linearly polarized light with a very narrow bandwidth of approximately 2 MHz and a very high output power of 0.1âĂŞ0.01 Watts in the frequency range from 107 to 177 GHz. The high output power in this base band is converted to higher frequency bands using a set of planar GaAs Schottky diode frequency multipliers. The spectral ranges from 220 to 350 GHz and from 330 to 525 GHz are covered using a single frequency doubler and a frequency tripler. For the spectral ranges from 650 to 1040 and from 980 to 1580 GHz two-stage frequency multiplier chains are required.

In order to conduct magneto-optic generalized ellipsometry measurements the original sample holder can be replaced with an electro-magnet with a maximum field strength of 2 Tesla. The sample is then mounted directly on the pole face with adhesive, as seen in figure 2.4, to minimize the distance between the pole faces and maximize the applied magnetic field. Limits on the available angles of incidence are imposed by the size of the magnetic coils and the distance between the pole faces, introducing a trade-off between normal generalized ellipsometry and magneto-optic generalized ellipsometry measurements. The instrument no longer exists in its described form, having been upgraded partially to nullify this trade-off (see Ref. 60). For more information about the THz ellipsometer in its described arrangement see Refs. 44, 48.

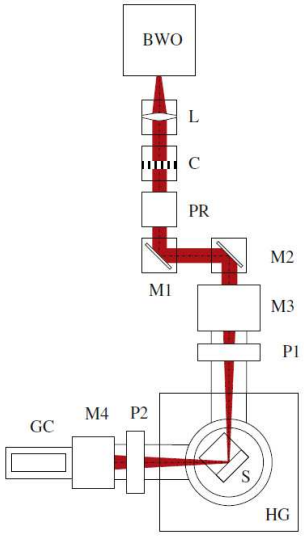

Figure 2.3: THz ellipsometer setup, showing the backwards wave oscillator (BWO), collimating lens (L), signal chopper (C), polarization rotator (PR), mirrors (M1-M4), polarizers (P1,P2), the sample (S) which sits on a goniometer (HG), and the Golay cell detector (GC).

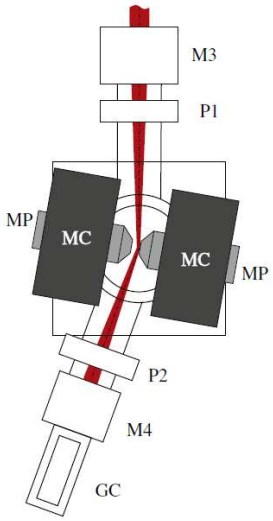

Figure 2.4: Alternative THz ellipsometer arrangement to enable magneto-optic THz ellipsometry. An electromagnet with coils (MC) and magnetic poles (MP) provides the static **B** field, with the MP face doubling as a sample holder.

2.1.7 Data Analysis

Ellipsometry is an indirect experimental technique and therefore data analysis invokes non linear model calculations to determine physical parameters [61]. The analysis follows a set procedure described by the flowchart in figure 2.5.

For a given spectroscopic ellipsometry experiment the user must start by choosing which parameters to vary within the optical model, including the thickness and any model dielectric function parameters, while including initialization values. These initialization values are combined with known physical parameters for the particular data set, including the angle of incidence (Φ), the frequency or photon energy of the test beam (ω,$\hbar\omega$), and the magnetic field **B** if present. The inclusion of data at more than one angle of incidence, while not required, provides internal self-consistency

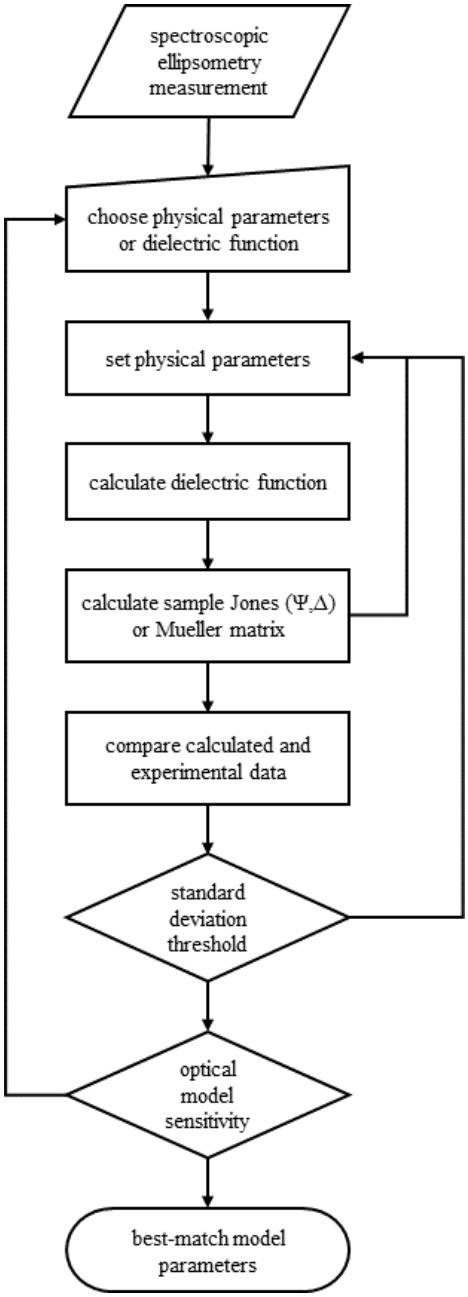

Figure 2.5: Flowchart describing the procedure for determining the best-match model parameters. During analysis of the spectroscopic ellipsometry data, certain parameters such as the angle of incidence, photon energy or wavelength, model dielectric function, and layer thickness, are used to calculate the optical response. The resulting calculation is compared to the experiment using a normalized standard deviation. Once a predefined maximum acceptable value has been reached, and the operator has determined that the dielectric function and thicknesses are appropriate, a set of best-match model parameters has been selected.

checks for the data analysis and also tends to balance available sensitivity to any sample parameters that change with the angle of incidence. Once the parameter group is set, Ψ and Δ for an standard ellipsometry measurement, or Ψ_{ij} and Δ_{ij} or M_{ij} for a generalized ellipsometry measurement, can be readily calculated via the 4×4 matrix formalism. This calculation is repeated until data has been generated for all of the known parameters ($\Phi, \omega, \mathbf{B}$, etc.). Calculated data from the optical model can now be directly compared to the experimental data. The comparison is numerically quantified by the mean squared error, and is given by

$$MSE_{\Psi,\Delta} = \sqrt{\frac{1}{2N-K}\sum_{i=1}^{N}\left[\left(\frac{\Psi^{\mathrm{E}}-\Psi^{\mathrm{G}}}{\sigma_{\Psi}}\right)^{2}+\left(\frac{\Delta^{\mathrm{E}}-\Delta^{\mathrm{G}}}{\sigma_{\Delta}}\right)^{2}\right]} \quad \text{or} \tag{2.39a}$$

$$MSE_{\mathrm{MM}} = \sqrt{\frac{1}{abS-K}\sum_{i=1}^{a}\sum_{j=1}^{b}\sum_{k=1}^{S}\left(\frac{M_{ij,k}^{\mathrm{E}}-M_{ij,k}^{\mathrm{G}}}{\sigma_{M_{ij,k}^{\mathrm{E}}}}\right)^{2}}. \tag{2.39b}$$

In equations 2.39, N, a, b, S, and K denote the total number of Ψ and Δ data point pairs, the number of experimentally determined columns and rows of the Mueller matrix, the total number of Mueller matrix data points, and the total number of parameters varied during the regression process, respectively, which together define the degree of freedom within the regression. The mean squared error is normalized by the total degree of freedom ($2N-K$ or $abS-K$) and by the standard deviation of the measured value (σ). The ellipsometry experiment is repeated over several rotations of the analyzing polarizer such that the experimental value ($\Psi^{\mathrm{E}}, \Delta^{\mathrm{E}}, M_{ij}^{\mathrm{E}}$) represents the average of this set and the standard deviation determines the measurement quality. The resulting mean squared error is therefore unitless, with an mean squared error of unity signifying that the error between the model generated data and the experimental data is equivalent to the standard deviation between experiments.

To ensure a fast convergence of the mean squared error regression, the Levenberg-Marquardt fitting algorithm is used [62]. The Levenberg-Marquardt fitting algorithm is interrupted when the decrease in the mean squared error is smaller than a set threshold, and the resulting parameters are considered to be best-match model parameters. The sensitivity and possible correlation of the varied parameters is checked and, if necessary, the model is changed and the process is repeated [63–65].

2.2 Spreading Resistance Profiling

Spreading resistance profiling is a simple low pressure contact based resistance measurement for determining local resistivity throughout a layered sample, as first demonstrated by Mazur and Dickey [66]. Data collection begins by beveling the sample at a small angle such that differing depths can be accessed by the lateral movement of a probe pair. A small voltage is then applied to the probe tips, and the resulting current is measured. The resistivity is backed out of the equation

$$\frac{V}{I} = R = \frac{\rho}{4a}, \quad \text{where} \quad a = 1.1\left(\frac{Fr}{2}\left[\frac{1}{E_1} + \frac{1}{E_2}\right]\right)^{1/8} \tag{2.40}$$

is the area of the probe tip, V is the test voltage, I is the resulting measured current, ρ is the resistivity of the sample, F is the force applied to the probe tips, r is the radius of curvature of the probe tips, and E_1 and E_2 are the Young's moduli of the sample and tip materials. Equation 2.40 describes the resistance experienced by identical hemispherical probes forming a disk-shaped contact with a semi-infinite sample. The multiple current paths available to the free charge carriers within the sample are concentrated at the probe tips providing excellent sensitivity to the local resistivity (relative to the contact area).

Measurements within this work were conducted on a commercial Solid State Measurements SSM-150 automated spreading resistance probe with the collaboration of Jan Šik of ON Semiconductor.

2.3 LEEM and μ-LEED

Low-energy electron microscopy (LEEM) and micro low-energy electron diffraction (μ-LEED) are complementary surface science techniques where a focused beam of low-energy electrons is reflected from a sample surface. Surface sensitivity is gained by reducing the energy of the incoming electrons with a controllable negative voltage applied to the sample. A low-energy also increases the reflection of electrons from the surface, allowing enough intensity for imaging. In this work LEEM images are all bright-field images, in which the primary diffracted beam is selected with a contrast aperture to form the image. Similarly, an aperture can be placed in the incident beam path to select a specific area of the sample for electron bombardment. In this way specific features in a LEEM image can be investigated with LEED, this technique is then dubbed μ-LEED. Both LEEM and μ-LEED experiments can be conducted with the same instrument, only a change in the aperture location and electrostatic lens focus is required [67].

All LEEM and μ-LEED images presented in this work were taken at the MAX I311 beamline laboratory in Sweden, with the collaboration of Dr. A. Zakharov. A schematic of the instrument is shown in figure 2.6. For LEEM experiments the field of view is between 2 and 50 µm, with a lateral resolution of 10 nm. The electron source is a LB_6 high flux cathode.

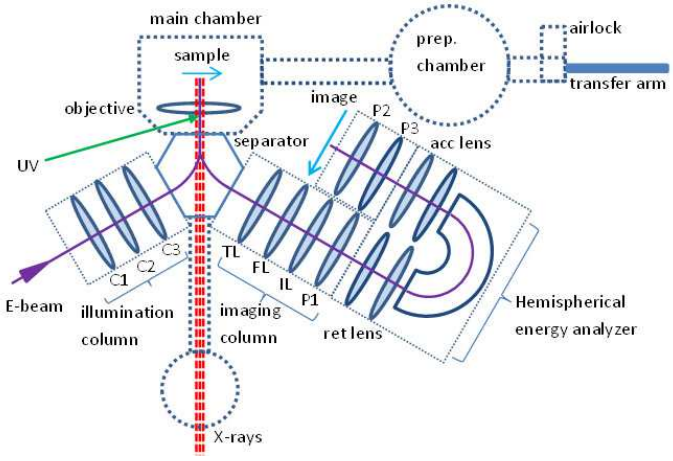

Figure 2.6: Schematic of the LEEM and μ-LEED microscope at the MAX I311 beamline laboratory. The hemispherical energy analyzer allows filtering of electrons with an applied magnetic field. Diffraction images are formed on the rear focal plane of the objective lens. Image credit: maxlab.lu.se.

Chapter 3

Iso- and Aniso-type Si Homojunctions

The ability to measure and mathematically model the electrical and structural properties of silicon homojunctions lies at the core of emerging transistor technologies. Silicon is reaching a scaling limit as processor manufacturers have now delayed planned hardware releases while struggling with the 10 nm node and extreme ultraviolet lithography [68]. Three-sided gate field effect transistors (also called FinFETs) and nanowire transistors designed around quantum tunneling are possible design approaches to overcoming the scaling limit [69, 70]. Both of these approaches rely upon nanoscale fabrication and characterization techniques, and generalized ellipsometry offers ideal non-contact and non-destructive characterization of periodic nanostructures [71–73]. Sensitivity to the birefringence and, by proxy of a model dielectric function, the electronic and structural properties of nanoscale columnar thin films also extends to generalized ellipsometery in the infrared and THz spectral ranges [74]. This chapter aims to show that standard spectroscopic ellipsometry is capable of simultaneous iso- and aniso-type homojunction characterization, including a complete carrier concentration profile comparable to that obtained with spreading resistance measurement.

Iso-type and aniso-type homojunctions are characterized by electric free-charge carrier interactions at the junction interface. In both cases it is assumed that dopant

atoms have zero mobility, so the steady state electric charge distribution is due entirely to free-charge carrier action. An aniso-type homojunction is a material junction where the crystalline bulk is identical on either side of the junction in crystallographic orientation only, but possesses doping materials of opposite carrier types and different doping concentrations. Free-charge carriers of opposing sign create an electric field at the interface, undergoing a drift process in which holes and electrons recombine, leaving ionized dopant atoms behind. This creates a space charge region, or equivalently, a depletion region.

An iso-type homojunction is a material junction where the crystalline bulk is identical on either side of the junction in crystallographic orientation and dopant material, but not in dopant quantity. This type of junction results in diffusion of free-charge carriers. Under the assumption that the dopant atoms are fixed to their original positions in the crystal lattice, a lack of free-charge carriers in the high concentration region and an excess in the low concentration region creates a space charge region. Since this process is driven by diffusion, it is also known as the carrier diffusion region. The space charge region left by the diffusion process produces an electric field that opposes further diffusion, eventually stopping the diffusion process with an quantitatively equal drift process. Unlike the aniso-type homojunction, the iso-type homojunction includes both carrier drift and diffusion processes. Consequently, mathematical modeling of the iso-type homojunction is complicated by a non-seperable second order differential equation, introduced in 3.1.1.

Free-charge carriers are most responsive to slowly-varying electric fields, therefore long-wavelength based electromagnetic investigation techniques are useful tools for their characterization. Initial attempts to measure the charge concentration profile of an iso-type homojunction involved time-domain based THz spectroscopy experiments in transmission configuration. Such measurements have successfully measured charge

concentrations of bulk single crystals, but determination of complex layered structure properties is still a challenge [75, 76]. Transmission techniques are limited by plasma absorption in the THz spectral region. This work utilizes THz and mid-infrared reflection type ellipsometric measurements as an optical method of determining the free-charge carrier concentration profile and thickness parameters of homojunction bounded silicon epilayers. Reflection configuration ellipsometry has been shown as a dependable technique for measuring free-charge carrier properties of layered semiconductor structures in the MIR and THz spectral range [18, 77–79].

3.1 Theory

3.1.1 Homojunction Charge Density Modeling

Any attempt at mathematically defining the diffused charge concentration profile of a planar iso-type homojunction involve the Poisson equation coupled with the semiconductor current density equation based on drift and diffusion, which results in the non-linear second order differential equation:

$$\underbrace{-\frac{d}{dx}\left[\frac{\mu_N D_N}{n(x)}\frac{d}{dx}n(x)\right] = \overbrace{\frac{d}{dx}E(x) = \left[\frac{N_D(x)-n(x)}{\varepsilon_0\varepsilon}\right]}^{\text{Poisson's equation}}}_{\text{drift and diffusion equation}}, \tag{3.1}$$

where $E(x)$ is the electric field in terms of the one dimensional depth x, oriented perpendicular to the junction plane. The electron mobility is represented by μ_N, and ε_0 and ε are the vacuum and material dielectric constants, respectively. Eqn. (3.1) is given only for electrons and makes two assumptions. First, the net current density is zero. Second, $N_D(x)$ and $n(x)$ describe the ionized dopant and free-charge carrier

distributions on both sides of the iso-type homojunction, respectively. Equation (3.1) shows that a changing charge concentration ($n(x)$) creates a space charge region identified in Poisson's equation by the difference between $N_D(x)$ and $n(x)$. This space charge must be balanced by a free charge carrier diffusion (with diffusion constant D_N, the diffusion is represented by $D_N \frac{d}{dx} n(x)$), and a carrier drift ($1/n(x)$). A general analytical solution for $n(x, y, z)$ is not available, thus most solution attempts revolve around numerical analysis or a reduction of dimensions [80, 81]. Since a numerical analysis is difficult to implement in ellipsometric data analysis, the latter approach is considered.

A one-dimensional analytical solution of the isotype homojunction problem was given by Kuznicki [82]. Kuznicki's approach assumes that the semiconductor material is non-degenerate and therefore $n(x)$ follows an energetic Boltzmann distribution. Rather than incorporating the drift and diffusion directly, the spatial charge distribution is linked to the electric potential statistically:

$$n(x) = N_D exp[q\phi(x)/kT], \tag{3.2}$$

where $\phi(x)$ is the electric potential, q is the elementary charge, k is the Boltzmann constant, and T is the temperature in Kelvin. The results are two independent expressions for $n(x)$ on each side of an abrupt iso-type homojunction, where the doping concentration (N, P) is assumed to be constant. The charge density profile for the highly doped side is then given by:

$$n_H(x, L_H) = N^+ exp\left[\left(-\frac{ln(N^+/N^-)}{1+\sqrt{N^+/N^-}}\right) exp(x/L_H)\right], \tag{3.3}$$

where N^+ is the large ionized dopant concentration, N^- is the small ionized dopant

concentration, and L is a characteristic charge screening length. The low-doped charge density profile is governed by a similar formula comprised of the same parameters:

$$n_L(x, L_L) = N^- exp\left[ln\left(\frac{N^+}{N^-}\right) - 2ln\left(exp\left[0.5\left(1 - \frac{N^- ln(N^+/N^-)}{N^+ - N^-}\right)\right] + x/L_L\right)\right]. \tag{3.4}$$

The same equations can be used for acceptor doping rather than donor doping, with only the donor equations listed here for brevity.

In order to employ the equations (3.2), (3.3), and (3.4) the following assumptions from Ref. [82] must be met:

1. Free charge carrier diffusion is limited to one dimension.
2. Every semiconductor layer is non-degenerate.
3. $N(x), P(x)$ can be modeled as an abrupt Heaviside expression with the higher side N^+, P^+ and the lower side N^-, P^-.
4. There is no dopant atom diffusion, i.e. the abrupt iso-type homojunction always occurs at $x = 0$.
5. $N^+ \gg N^-$, with at least $N^+/N^- > 7$, with the same condition required of P.

The last limitation can be overcome with a differing approximation, also given in Ref. 82, which addresses iso-type homojunctions with small doping ratios like those found in previous works [77, 79].

At the aniso-type homojunction interface, the charge carrier action can be modeled with the depletion approximation. The depletion region width (d_{dep}) can be calculated

easily [83], using the relative charge concentrations as parameters:

$$d_{dep} = \left[\frac{2\varepsilon_0 \varepsilon kT}{q^2}\left(\frac{P+N^-}{PN^-}\right) ln\left(\frac{PN^-}{{n_i}^2}\right)\right]^{\frac{1}{2}}, \tag{3.5}$$

where P is the acceptor concentration in the P-type Si epitaxial layer and n_i is the intrinsic carrier concentration of silicon. Exact solutions for the carrier concentration $n(x), p(x)$ would include diffusion of majority carriers into the depletion region, or in other words Sec. 3.1.1 needs to be applied twice, once to each side of the depletion region. Such rigorous treatment of the problem is avoided here, as the limit of free-charge carrier sensitivity for THz-MIR ellipsometry is on the order of 10^{13} cm^{-3} [35, 79, 84], which would add unnecessary complexity to the optical model.

3.1.2 Model Dielectric Function & Optical Model

The free charge carrier contribution to the dielectric function ($\varepsilon(\omega)$) is expressed by the Drude approximation, which consists of a harmonic oscillator with no return force (i.e., possessing a resonant frequency of zero):

$$\varepsilon(\omega) = \varepsilon_{DC} - \frac{nq^2}{\varepsilon_0 m(\omega^2 + i\omega\mu m/q)}, \tag{3.6}$$

where $\varepsilon_{DC} = 11.7$ is the low frequency offset, ω is the incident light angular frequency, q is the elementary charge, m is the effective mass, and μ is the mobility. In order to separate μ and m from n, effective mass parameters were assumed to be 0.26 m_e for electrons and 0.37 m_e for holes (where m_e is the free electron mass)[76]. The mobility (μ) was calculated from n or p using an empirical model described by Jacoboni *et al.* [85]:

$$\mu = \mu_{min} + \frac{\mu_{max} - \mu_{min}}{1 + \left(\frac{n}{N_{ref}}\right)^{\alpha}}, \tag{3.7}$$

where $\mu_{min} = 92$ cm^2/Vs, $\mu_{max} = 1360$ cm^2/Vs, $N_{ref} = 1.3 \times 10^{17}$ cm^{-3}, and $\alpha = 0.91$ for electrons; and $\mu_{min} = 47.7$ cm^2/Vs, $\mu_{max} = 495$ cm^2/Vs, $P_{ref} = 6.3 \times 10^{16}$ cm^{-3}, and $\alpha = 0.76$ for holes.

Two optical models are used fit ellipsometry data, and are compared in Sec. 3.4. The first is a physical model in which consequences of parameter changes are enforced even during the mean squared error regression analysis described in Sec. 2.1.7. An example of this behavior is the width of a depletion region, which is dependent upon the doping concentrations, P and N, on either side of the interface. One potential consequence is diffusion from a highly doped region into a lesser doped region. This diffusion region has a changing carrier concentration, which violates the assumption that individual layers within a given sample are homogenous, as required by the 4×4 matrix formalism used in analysis (see Sec. 2.1.2). This problem is solved by expanding the diffusion region into many individual thin layers in the optical model, each with a homogenous carrier concentration whose value is governed by the functions in Eqns. (3.3) and (3.4). The second optical model allows the individual model parameters, for example N, P, μ or d, to vary freely within the analysis. This optical model does not account for diffusion or depletion of carriers within the sample but offers a more direct analysis.

3.2 Experiments

The investigated sample is composed of a heavily antimony doped n-type Si substrate followed by a low antimony doped n-type Si epitaxial layer and a low boron doped p-type Si epitaxial layer, all with the $\langle 111 \rangle$ orientation. This sample will be referred to in the following as the $N^+/N/P$ sample. The $N^+/N/P$ sample was selected because it contains both types of homojunctions as well as two depletion regions, and is therefore

a suitable test for the proposed depletion and diffusion models.

Spectroscopic ellipsometry (SE) measurements were carried out in the THz and MIR spectral ranges at two different angles of incidence $\Phi_a = 50°$ and 70°. We employed two different instruments for the measurements shown here. A commercially available MIR spectroscopic ellipsometer (J.A. Woollam Co. Inc.) and the custom THz ellipsometer, operating with the $2\times$, $3\times$, and $2+3\times$ waveguide multipliers. See Sec. 2.1.6 for more information on the ellipsometers used.

Upon completion of the ellipsometry experiments the sample was beveled and a spreading resistance measurement was conducted. The bevel angle was 5.73° with 5 µm steps (along the beveled face) between resistance tests. The contact probes were placed 100 µm apart. Spreading resistance instrumentation is covered in Sec. 2.2.

3.3 Results

The THz- and MIR-SE data are presented in Fig. 3.1. The spectral range from 10 to 20 THz is dominated by Fabry-Pérot interference oscillations which decay towards higher frequencies. In the spectral range from 0.2-1.0 THz we observe two strong resonances at $\nu = 0.29$ THz and 0.89 THz. These resonances are attributed to the excitation of surface guided waves (SGW) in TE mode (electric field vector parallel to the interface) radiation fields [86]. The position, amplitude, and broadening of the surface guided waves are extremely sensitive to the free-charge carrier profiles within the sample [48]. For both the physical and free floating optical models discussed in Sec. 3.1.2 a small offset was required for the 50° angle of incidence, and is presented in table 3.1 along with all of the other ellipsometry best-match model parameters.

Ellipsometry data were first analyzed using a 6 phase physical optical model (see top of Fig. 3.2). In addition to the N^+ substrate and the two epitaxial layers (N, P),

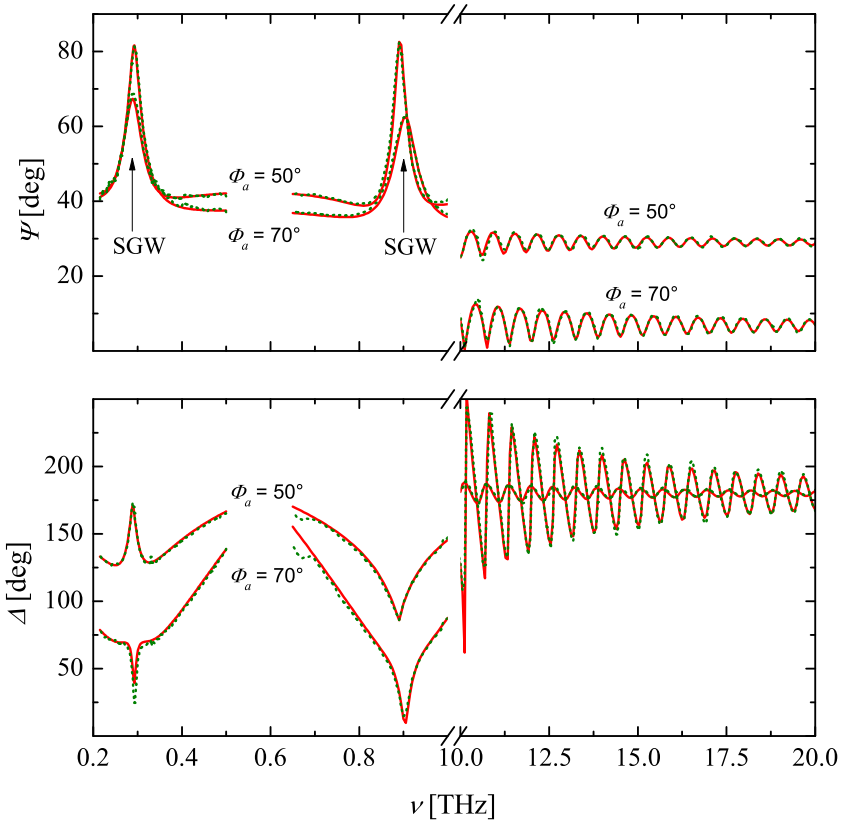

Figure 3.1: Experimental (green dotted lines) and calculated physical model (red solid lines) Ψ and Δ spectra at 50° and 70° angles of incidence for a $N^+/N/P$ sample. Data above 20 THz continues with the Fabry-Pérot interference pattern but was omitted for clarity.

depletion regions and extended diffusion regions have to be included. The resulting free charge carrier profile is depicted in Fig. 3.2. Ellipsometric Ψ and Δ values calculated form this model are shown in Fig. 3.1.

The diffusion region between N^+-Si substrate and N-Si epilayer is governed by free-charge carrier diffusion and drift processes which are analytically incorporated in the layer optical model as described in Sec. 3.1.1. The resulting spatially asymmetric carrier profile is approximated by a discrete variation of the free-charge carrier concentration and mobility within 550 sub-layers with abrupt interfaces. The abrupt interface between the N^+-Si substrate and the N-Si epilayer is the location

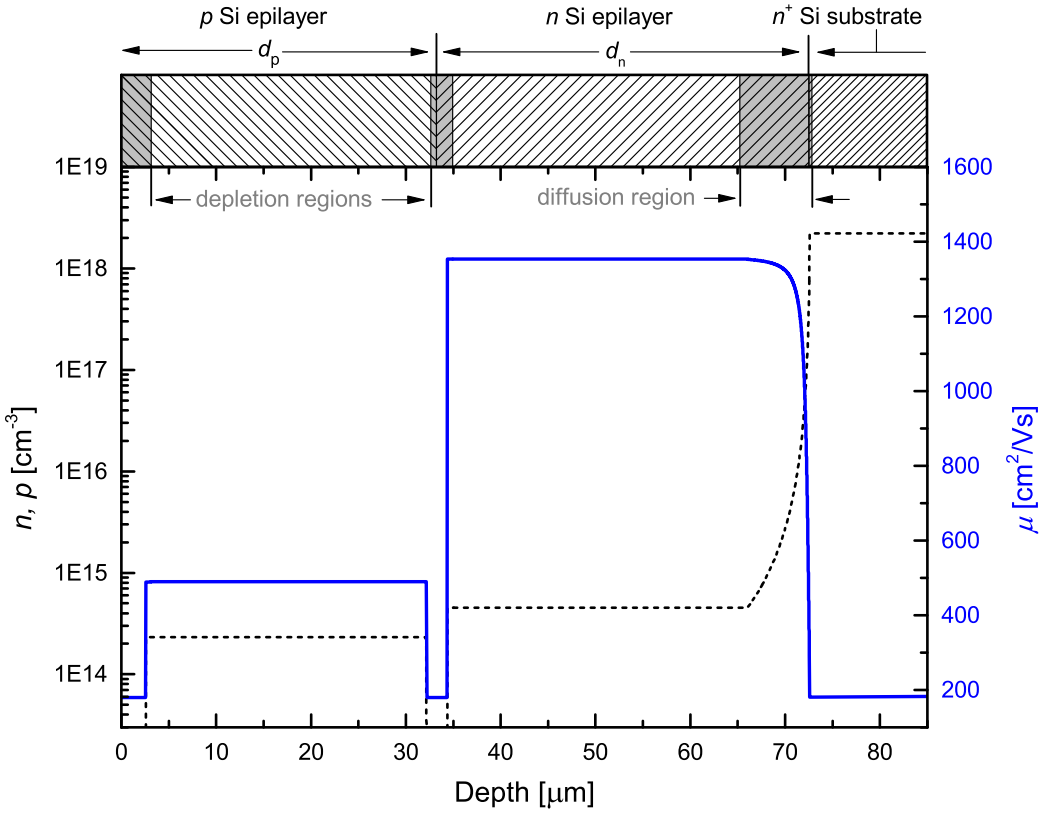

Figure 3.2: FCC concentration (black line) and mobility (blue dotted line) profile as a function of x. Profiles were calculated from best-match model values of the FCC concentration, the characteristic charge screening length, and epilayer thickness. The uppermost bar shows the sample structure. A break in the graph was included to show the entire P-Si epilayer.

where $n_H(x, L_H) = n_L(x, L_L)$. In the substrate Eqn. (3.3) governs the divergence of the carrier concentration from the substrate value N^+ over 50 sub-layers. Inside the N epilayer Eqn. (3.4) governs the accumulation of electrons diffusing from the substrate in excess of N over 500 sub-layers. The overall thickness of the interface region is determined by the parameters L_H and L_L, as only one thickness value allows $N^+ = n_H(-\infty, L_H)$ and $N = n_L(\infty, L_L)$. Because $N^+ \gg N$ the height of the drop region is smaller than 100 nm, and sensitivity to L_H was lost. The parameter L_H was

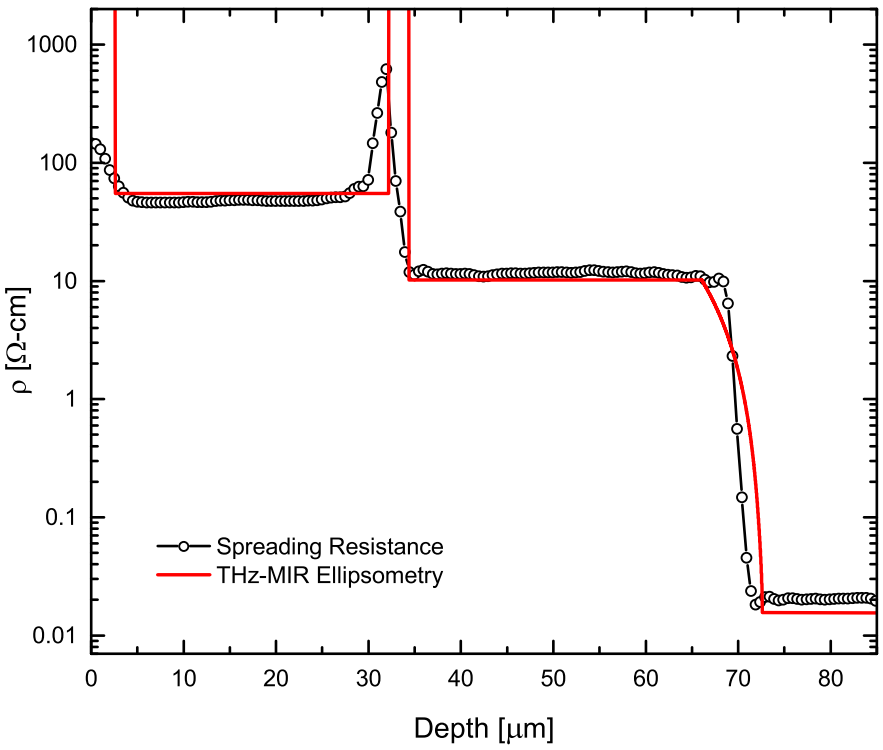

Figure 3.3: Best-match seven layer optical model from THz through MIR data analysis (solid red line) plotted with spreading resistance data (symbols and black line). Symbols represent data point locations with respect to depth, irrespective of error.

then fixed such that the drop off region thickness was equal to 100 nm.

The depletion region between the N-Si epilayer and the P-Si epilayer is modeled with the depletion approximation where it is assumed most free charge carriers have recombined, leaving a space charge region with only the intrinsic resistivity of silicon. The width of this region is dynamically calculated from the carrier concentrations of the bounding interface layers (N and P) as described by Eqn. (3.5). A depletion region is also required at the sample surface, where surface charge produced by dangling silicon bonds recombines with the available holes in the P epilayer. Sensitivity to the quantity surface charge is limited due to the complexity of the sample, and the value was fixed to 8×10^{14} cm^2 as suggested in the literature [87]. For this depletion

region Eqn. 3.5 was modified such that the entire depletion region falls within the P epilayer.

The second optical model used was a three phase model, not including the depletion or diffusion regions, but only the P and N epilayers and the N^+ substrate. The mobility in each layer was allowed to float free of the carrier concentration during the analysis.

Spreading resistance profiling data is presented in Fig. 3.3, alongside resistivity data generated from the best-match physical model. Resistivity was calculated from best-match model parameters as $\rho = 1/(q\mu_n n)$ (or with $\mu_p p$), ignoring minority carriers. The spreading resistance data exhibit sensitivity to both depletion regions and the diffusion region, and compare favorably with the ellipsometry generated data.

Table 3.1: Best-match model parameters for the physical model presented here and a simple free parameter model. The last significant digit of each value is followed by the 90% confidence interval in parenthesis, e.g. 1.1 ± 0.1 is 1.1(1).

Parameter		Physical Model	Free Model
MSE		1.504	1.008
50° offset	[°]	0.86(4)	0.83(3)
L_L		−11.56(7)	N/A
$\log_{10} N^+$	[cm^{-3}]	18.344(4)	18(18)
μ_{N^+}	[cm^2/Vs]	181.530(~0)	243(2)
$\log_{10} N$	[cm^{-3}]	14.657(4)	14.44(1)
μ_N	[cm^2/Vs]	1352.675(~0)	3110(240)
d_N	[µm]	39(2)	51(1)
$\log_{10} P$	[cm^{-3}]	14.367(9)	10(10)
μ_P	[cm^2/Vs]	488.8(2)	0.0(4)
d_P	[µm]	33(2)	22(1)

3.4 Discussion

The application of the physical optical model results in an excellent agreement between best-match calculated and experimental data shown in Fig. 3.2. Accurate $N^+/N/P$ sample analysis relies heavily on the correct description of the diffusion region. A symmetric diffusion profile, as implemented in previous work (see Ref. [79]), was rejected because it leads to increased RMSE values and does not provide access to important structural parameters, such as the abrupt isotype homojunction location. Additionally the asymmetric carrier diffusion profile model contains only physical parameters (e.g. the Debye lengths, active dopant concentrations), where as the previous work relied upon the error function and required a non-physical broadening parameter. Consequently, the asymmetric diffusion model can accurately describe the thickness of the N-Si epilayer, a requirement under the assumption of plane parallel interfaces between sample layers. Non-contact, non-destructive measurement of the abrupt isotype homojunction location and its spatial relationship to diffusion carriers is useful for improving the fabrication process of iso-type homojunction devices, and is only limited by assumptions (3) and (4) in Sec. 3.1.1. The ability to distinguish between carrier concentration profiles is ascribed to the THz measurement, as the evanescent surface guided waves measured in the THz region are bound to the iso- and aniso-type interfaces. The surface guided wave dispersion is obtained from the s-polarized light reflectance (r_s) which is dependent on the depth profile of the dielectric function and the total thickness of the epilayer (see Eqn. (3.6)) [18, 86]. This sensitivity to carrier concentration and thickness is exploited in the physical model analysis.

A comparison between the physical model and the free parameter model reveals that the added flexibility of the free parameter model grants a smaller RMSE value.

Normally the model with the lower RMSE is used as the superior model, but in this case the extra flexibility leads to a complete loss of the N^+ substrate and P epilayer doping density information. In contrast the physical model is extremely sensitive to all of the varied parameters. The mobility given for the physical model in table 3.1 was not a varied parameter but was calculated from the carrier concentration as discussed in Sec. 3.1.2, and thus the error in μ is dependent on the error carrier concentration and ultimately the doping density. In the case of the N^+ and N regions the error in the doping density was small enough that the error in μ was less than 1×10^{-6}, or ~0 when compared with the significant digits of the doping density. The free parameter model is included here because it represents the standard approach for analyzing ellipsometry data for samples of this nature. This analysis highlights the importance of the model dielectric function within ellipsometry data analysis, and displays the potential of broad spectrum ellipsometry to characterize complex semiconductor homojunctions.

Preference for the physical model is validated by the spreading resistance measurement, which shows excellent agreement with the best-match physical model in Fig. 3.3. Starting at the top of the sample, the surface depletion region appears broader than the ellipsometry result. This may be due to the incomplete nature of the depletion approximation, or to added surface carriers induced by damage from the beveling procedure [88]. The depletion region between the P and N epilayers is similar in width to the spreading resistance measurement but is offset by a few µms. Most likely this is due to the diffusion within the depletion region that is not modeled, coupled with the added sensitivity of the THz and mid-infrared radiation to the lower resistivity N epilayer. As the resistivity decreases the material becomes more reflective, and both the surface guided waves and the interference pattern in the ellipsometry data are sensitive to that change. This could also explain the differ-

ence between the ellipsometry model and the spreading resistance data in the N/N^+ diffusion region. It seems that Eqn. 3.4 over estimates the diffusion distance, and minimizing the RMSE results in a compromise between the diffusion location and the magnitude of the N^+ doping density.

3.5 Conclusions

Optical measurement of the electrical and structural properties of a complex multi-junction silicon epilayer sample has been demonstrated. Application of a physical model for iso-type and aniso-type homojunctions to broad spectrum ellipsometry data from 0.2 to 50 THz at multiple angles of incidence allows determination of free charge carrier depth profiles, including diffusion and depletion regions. In addition, the thicknesses and dopant densities of each epilayer can be determined. Comparison of calculated resistivity from best-match parameters to a spreading resistance measurement values reveals excellent agreement and validates use of a complex physical model. THz to mid-infrared ellipsometry measurement has proven a valuable tool for the non-contact, non-destructive determination of complex semiconductor homo-junctions. By adding the results of this work to the known sensitivity of visible ellipsometry to characterize the birefringence of columnar nano-structures, broad spectrum ellipsometry is poised to to be the chacarterization tool of choice for upcoming tunnel field effect transistors.

Chapter 4

Hole-Channel Conductivity in Epitaxial Graphene

Graphene has revealed numerous unique physical and electrical properties, including very high carrier mobilities $\mu > 15,000$ cm^{2}V^{-1}s^{-1}, high carrier velocities $\sim 10^8$ cm s^{-1}, high current densities $> 10^8$ Acm^{-2}, and a long mean free path > 0.5 μm, which have been observed at room temperature [1, 89]. Any single one of these properties can be useful in the design of graphene based electronics. Wafer-scale production of epitaxial graphene can be obtained by Si sublimation from SiC substrates [90, 91]s, and is potentially suitable for production of electronic devices. It has been observed, however, that the highest mobilities achieved in free-standing graphene are orders of magnitude larger then the record mobilities in epitaxial graphene [92]. The identification of the origin of this reduction is of paramount contemporary interest.

Investigation of the free charge carrier properties of graphene has been prolific, with the most samples including custom fabricated contacts for each experiment [1, 5, 6, 89, 93–95]. Electrical contact materials for these experiments included deposited gold, lead, and chromium, and silver paste, perhaps explaining the variance in reported results. Experiments conducted on elaborately suspended samples often only have two contacts, limiting the experiment to measuring the resistivity alone. Experiments with fabricated Hall bars can separate the measured resistivity into free

charge carrier density and mobility much in th same way resistivity was calculated in chapter 3, but have no sensitivity to the carrier effective mass. In addition many of these samples become unusable for further study after deposition of the electrical contacts. Alternatively large epitaxial graphene samples on semi-insulating SiC have been measured using copper pressure contacts in the van der Pauw configuration [96]. Mono-atomic graphene on an insulating substrate is an excellent fit for van der Pauw's method, but requires patterning of the graphene sample in order to mitigate error [97]. It is clear that an alternative technique is desired in order to fully characterize the carrier density, mobility, and effective mass prior to device fabrication, such that device performance can be directly related to the graphene electrical transport properties.

Non-destructive and non-contact optical measurement of free charge carrier mobility, sheet density, and effective mass parameters in epitaxial graphene can be achieved by THz and midinfrared spectroscopic ellipsometry and THz optical Hall effect measurements, as demonstrated here on epitaxial graphene at room temperature. Epitaxial graphene samples were grown by Si sublimation on Si- and C-terminated semi-insulating 6H SiC substrates. Good agreement is found between carrier concentration and mobility parameters determined using OHE and electrical Hall effect techniques.

4.1 Experiments

The two epitaxial graphene samples investigated here were grown on 6H-SiC by thermal sublimation of Si. One graphene film was grown on the Si-terminated 6H-SiC (0001) surface and the other was grown on the C-terminated 6H-SiC $(000\bar{1})$ surface. Both SiC substrates are semi-insulating. Graphene growth took place at $1700°C$ in an Argon atmosphere. Further information on the growth conditions can be found in

Ref. 98 and references therein.

A commercial Fourier transform-based mid-infrared ellipsometer (see table 2.2) was employed for the measurements in the spectral range from 10 to 35 THz (333 to 1200 cm^{-1}) with a resolution of 60 GHz (2 cm^{-1}), for angles of incidence 55° and 75°. Selected experimental data are shown in Fig. 4.1. The custom-built frequency-domain THz ellipsometer discussed in Sec. 2.1.6 was used for the measurements in the spectral range from 0.65 to 1.00 THz with a resolution of 1 GHz at an angle of incidence $\Phi_a = 80°$. Selected experimental data are shown along with the best-match model in Fig. 4.2. The magnetic field direction for the optical Hall effect measurements is oriented perpendicular to the sample surface as per Fig. 2.4 [48, 99].

Room temperature THz-SE and THz-OHE measurements were carried out on both samples at an angle of incidence $\Phi_a = 80°$, as the angle of incidence was constrained by the electromagnet (see Fig. 2.4). During the OHE measurements the samples are exposed to fields from $\mu_0 H = -1.7$ to $+1.7$ T. Mueller matrix difference spectra for the optical Hall effect are shown in Fig. 4.3, while field dependent measurements for specific frequencies (C-face SiC only) are shown in Fig. 4.4.

4.2 Optical Model & Dielectric Function

The experimental THz-SE and THz-OHE ellipsometry data sets were combined in a stratified layer model analysis using parameterized model dielectric functions. All model calculated data were matched simultaneously as closely as possible to the experimental data by varying relevant physical model parameters (best-match model)[61]. The optical Hall effect ultimately determines the anisotropic dielectric response, which is produced by free-charge carrier momentum-energy redistribution under the action of external electric and magnetic fields, as a function of frequency and field

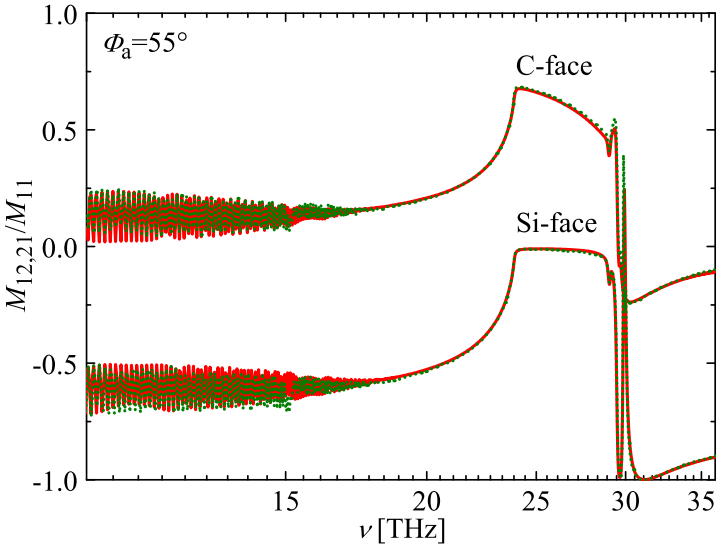

Figure 4.1: Experimental (dotted lines) and best-model calculated (solid lines) $M_{12,21}$-spectra for a graphene layer grown on C-face and Si-face SiC in the 10 to 35 THz domain at an angle of incidence $\Phi_a = 55°$. The C-face grown graphene imposes distinct changes on the reststrahlen band of SiC (23.8-30 GHz). Note that the spectrum for the C-face sample was shifted by 0.7.

strength. The anisotropic dielectric tensor elements at THz frequencies contain information about collision time and effective mass [100]. A plethora of physical model approaches for evaluating the distribution averaged drift mobility exist, which can be implemented to derive physically meaningful parameters. The simplest approach leads to the classical Drude model, where the mobility presents an energy-distribution average over collision times (average momentum-relaxation time). The Drude model has been found to accurately match the ellipsometrically measured dielectric function tensor at long wavelengths from all semiconductor 3D and 2D free carrier densities, and also matches experimental data from epitaxial graphene.

The Drude contribution to the dielectric function is described by the following dielectric tensor which allows the determination of the screened plasma frequency

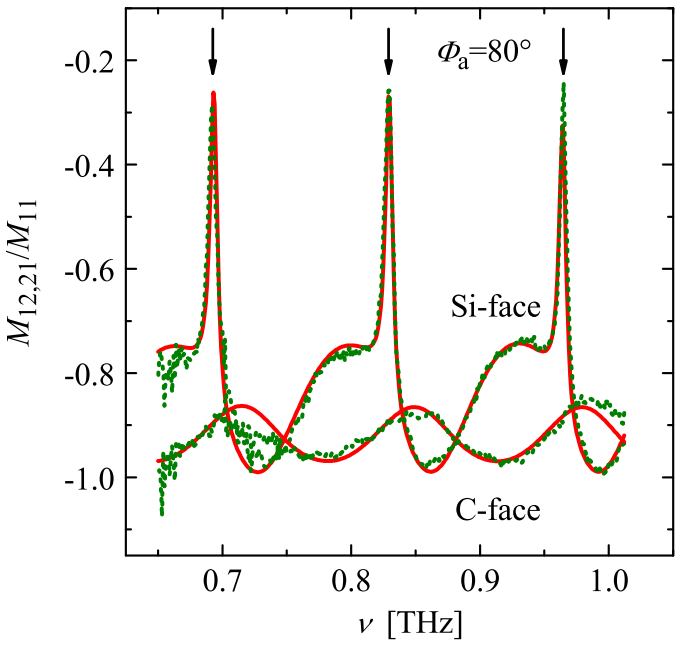

Figure 4.2: Experimental (dotted lines) and best-model calculated (solid lines) $M_{12,21}$-spectra for a graphene layer grown on C-face and Si-face SiC in the THz domain at an angle of incidence $\Phi_a = 80°$. The substrate anisotropy induced Fabry-Pérot pattern (arrows) is strongly suppressed by free-charge carrier absorption in the C-face grown graphene.

tensor $\boldsymbol{\omega}_p$ and the cyclotron frequency tensor $\boldsymbol{\omega}_c$[84, 101]:

$$\boldsymbol{\varepsilon}^{\text{FC-MO}}(\omega) = \varepsilon_{DC}\boldsymbol{I} + \boldsymbol{\omega}_p^2 \times \left[-\omega^2\boldsymbol{I} - i\omega\boldsymbol{\gamma} + i\omega \begin{pmatrix} 0 & b_3 & -b_2 \\ -b_3 & 0 & b_1 \\ b_2 & -b_1 & 0 \end{pmatrix} \boldsymbol{\omega}_c \right]^{-1}, \tag{4.1}$$

where the scattering tensor $\boldsymbol{\gamma}$ is a function of the free-charge carrier mobility tensor $\boldsymbol{\mu}$ given by $\boldsymbol{\gamma} = q/(\boldsymbol{\mu}\boldsymbol{m}^\star)$ and $\boldsymbol{m}^*$ denotes the effective mass tensor in units of the free electron mass m_0. $\boldsymbol{\omega}_p$ is related to the free-charge carrier concentration N and the effective mass tensor $\boldsymbol{m}^*$ by $\boldsymbol{\omega}_p^2 = Nq^2/(\varepsilon_\infty\tilde{\varepsilon}_0\boldsymbol{m}^* m_0)$, where q denotes the charge, $\tilde{\varepsilon}_0$ is the vacuum permittivity, and ε_∞ denotes the high frequency dielectric constant.

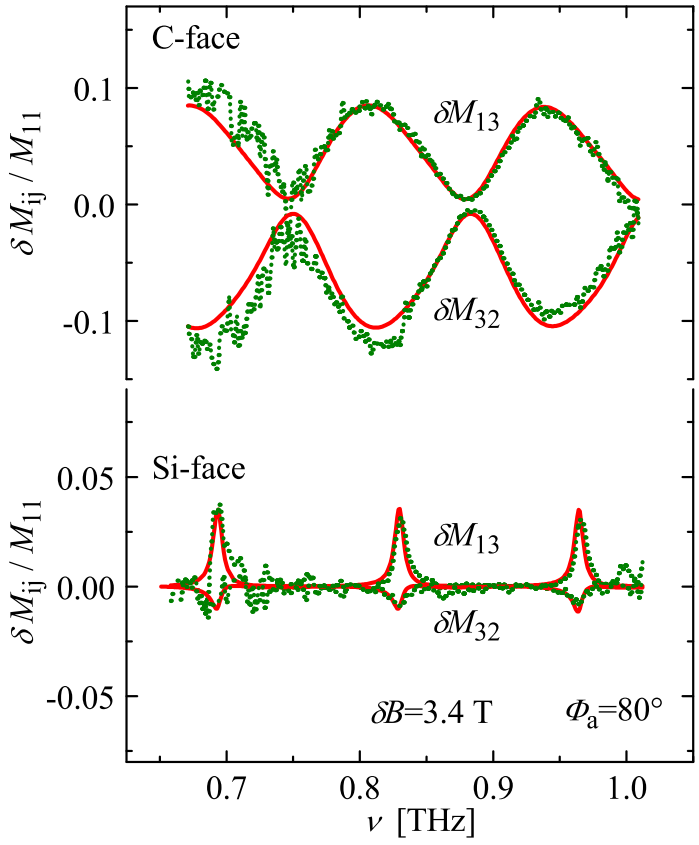

Figure 4.3: Experimental (dotted lines) and best-model calculated (solid lines) Mueller matrix difference spectra ($\delta M_{ij} = M_{ij}(B = +1.7\ T) - M_{ij}(B = -1.7\ T)$) for a graphene layer grown on C-face and Si-face SiC in the THz domain obtained at an angle of incidence $\Phi_a = 80°$.

The cyclotron frequency tensor is defined as $\boldsymbol{\omega}_c = qB/(m_0)\boldsymbol{m}^{*-1}$. The DC dielectric constant is given by ε_{DC} and $\boldsymbol{I}$ is the identity matrix. The external magnetic field is given by $\boldsymbol{B} = B(b_1, b_2, b_3)$ with $|\boldsymbol{B}| = B$.

A three-phase (substrate/high-mobility-graphene layer/low-mobility-graphene layer) model was needed to match calculated and experimental spectra for the C-face sample. Graphene grown on C-face SiC is typically several monolayers thick [102]. When obtaining sheet density parameters N_s, the layer thickness parameter for each layer cancels out mathematically within the ellipsometric equations for thickness parameters much smaller than the probing wavelength, and is thus irrelevant for this data

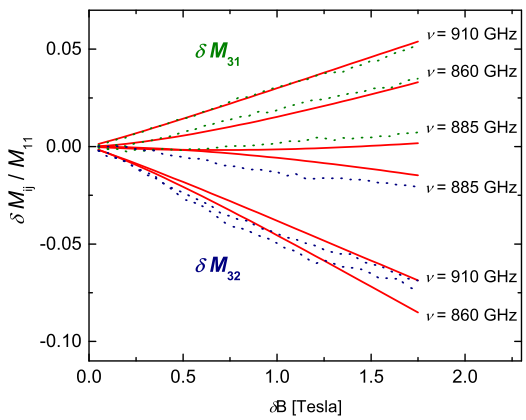

Figure 4.4: Mueller matrix elements M_{31} (green, dotted lines) and M_{32} (blue, dotted lines) for C-face SiC as a function of the applied field **B**, along with best match model calculations assuming a square-root dependence of the effective mass.

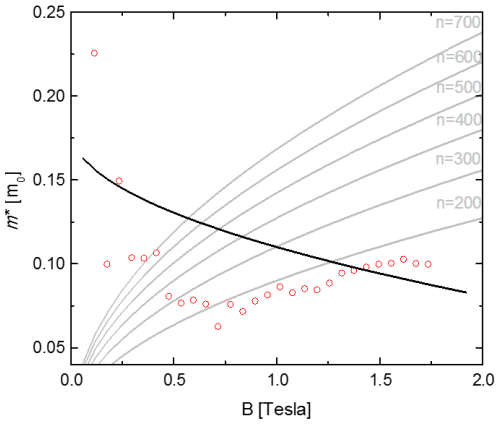

Figure 4.5: Effective mass of carriers within the C-face SiC sample as a function of **B** for individual fits (red circles), along with the square root dependence (black line). Grey lines indicate that this region is not bound by Landau levels.

analysis. A separate Drude model parameter set was used for the high-mobility graphene layer and for the low-mobility graphene layer. For the Si-face graphene, a two phase model composed of the graphene layer and the SiC substrate was found to be sufficient for best-match experimental data description. Graphene layers grown on the Si-face are typically one-to-few monolayers thick [102].

4.3 Results & Discussion

The anisotropic dielectric functions of the c-plane 6H-SiC substrate are parameterized with Lorentzian lineshapes which account for transverse (TO) and longitudinal optic (LO) phonon frequencies, $\omega_{\mathrm{TO},j}$ and $\omega_{\mathrm{LO},j}$, respectively, and the DC dielectric polarizability contributions $\varepsilon_{\mathrm{DC},j}$ for polarization $j =$"$\parallel$", "$\perp$" to the SiC c-axis [103]. The best-model parameters were obtained for $\varepsilon_{\mathrm{DC},\parallel} = 10.09 \pm 0.01$ and $\varepsilon_{\mathrm{DC},\perp} = 9.74 \pm 0.01$ and which are in good agreement with previous Lyddane-Sachs-Teller approxima-

tions [104]. The best-model phonon resonance frequency and broadening parameters ($\omega_{\mathrm{TO},\perp} = (797.7 \pm 0.1)$ cm^{-1}, $\omega_{\mathrm{TO},\perp} = (970.5 \pm 0.1)$ cm^{-1}, $\gamma_{\perp} = (2.9 \pm 0.1)$ cm^{-1}, $\omega_{\mathrm{TO},\parallel} = 788$ cm^{-1} [103], $\omega_{\mathrm{LO},\parallel} = (965.4 \pm 0.1)$ cm^{-1} $\gamma_{\parallel} = (3.7 \pm 0.1)$ cm^{-1}) which been obtained from MIR-SE measurements shown in Fig. 4.1 are in good agreement with literature values [103, 105].

The THz-SE spectra in Fig. 4.2 are governed by Fabry-Pérot interference pattern originating from the SiC substrate. A striking difference can be noted between the spectra of the C-face and the Si-face grown graphene samples. The SiC substrate interference pattern shows very sharp resonances for the Si-face sample (vertical arrows in Fig. 4.2). The spectrum of the C-face grown graphene sample also shows an interference pattern but the oscillations appear much more damped. Considering that the substrate material is identical except for the crystallographic orientation this observation suggests that the damping effect seen for the Si-face sample is connected with the free-charge properties of the few-Ångström thick graphene film.

The MIR-SE spectra shown in Fig. 4.1 reveal the phonon resonances of SiC in the range from 23 to 30 THz. The distinct resonances in the range from 29 to 30.5 THz can be attributed to the anisotropy of SiC [103]. Similar to the effects seen in the THz domain, the free-charge carrier response in the MIR results in a damping of the substrate resonances for the C-face grown sample.

The THz-OHE spectra (differences of the Mueller matrix elements measured at $B = 1.7$ T and -1.7 T) obtained for the two samples are presented in Fig. 4.3. The magnetic field is oriented perpendicular to the sample surface with the sample mounted directly to the magnet's pole face. Similarly to the THz-SE measurements, the THz-OHE data are dominated by Fabry-Pérot interference pattern originating from the SiC substrate. In contrast to the THz-SE spectra, however, the OHE response from the C-face is much stronger than the Si-face sample. The variations

between the sets of data are entirely caused by the different free-charge carrier properties within the epitaxial graphene layers. It is important to note also the strong OHE response (the Mueller matrix differences in M_{32} and M_{13} are proportional to percentage of cross-polarization emerging from the sample under linear or circularly polarized light illumination at the given frequency), which are only produced by the free-charge carriers within the epitaxial graphene layer [18, 84].

The best-match model between experimental and calculated data reveals for the C-face sample two graphene layers with distinctly different properties: a p-type channel towards the substrate with a sheet carrier density $N_{\mathrm{s}} = (5.5 \pm 0.4) \times 10^{13}$ cm^{-2} and mobility $\mu = 1521 \pm 52$ cm^{2}V^{-1}s^{-1}; and a second p-type channel above with higher sheet carrier density $N_{\mathrm{s}} = (3.4 \pm 0.6) \times 10^{14}$ cm^{-2} and lower mobility $\mu = 18 \pm 4$ cm^{2}V^{-1}s^{-1}. The charge carrier mobilities for the two channels are found to be in good agreement with values obtained using electric Hall effect measurements on a large set of samples with sheet carrier density ranging from 10^{12} to 6×10^{14} cm^{-2} [96]. Analysis of the field dependent measurements provided no change of the sheet density and mobility parameters, but revealed a square-root magnetic field dependence of the effective mass parameter for the high-mobility channel towards the substrate: $m^* = (0.19 - 0.08\sqrt{B})m_0$, where B is the magnetic field value in Tesla. The field-dependence can be understood by the surface topology of the C-face grown sample ("giraffe stripes" [102]), which forms flat graphene disrupted by terrace formation and step-bunching. As the magnetic field increases, the carrier drift motion covers smaller areas of the surface under the action of the Lorentz force, and the 2D character of the graphene carriers is revealed (effective mass reduces). This behavior is illustrated in Fig. 4.4 (black line), and is compared to the result if every data set (with respect to B) is fit independently. Similar to chapter 3, the result of fitting parameters individual produces a rather chaotic result. By imposing the consequence of the sample

morphology upon the fit, the effective mass parameters are constrained, the correlation between parameters is reduced, and a more satisfactory result is established. The effective mass in the top layer was $m^* = 0.035\ m_0$ [99], and did not reveal field dependence due to the strong scattering in the disrupted top layer. Electrical (DC) Hall effect measurement revealed p-type conductivity with $\mu = 3407 \pm 250\ \mathrm{cm^2 V^{-1} s^{-1}}$ and $N_\mathrm{s} = (3.0 \pm 0.5) \times 10^{13}\ \mathrm{cm^{-2}}$. The correspondence with electrical and optical-Hall effect data is very good, given that the low-mobility channel is not identified by electrical Hall effect measurements.

Note that the identification of different carrier channels in electrical Hall effect measurements requires magnetic field or temperature dependent measurements which were not performed here. Very recently, Lin et al. identified up to three different carrier channels in magnetic field dependent electrical Hall effect measurements carried out on graphene samples grown on C-face SiC [106]. There are several potential causes for the dual-channel nature of the C-face graphene. Unlike typical semiconductors which contain a band gap, the Dirac cone at the K-point in the graphene band structure can theoretically absorb light throughout the mid-infrared and THz regions. These interband transitions form a constant optical conductivity within the influence of the Dirac cone [107], and since $\sigma/\omega = \varepsilon_2$ the constant conductivity will produce a dielectric absorption that decays with frequency, and could be mistaken with the similar Drude function. If true, this effect should also be seen on the Si-face, and since the Si-face data can be fit with a single channel model this explanation is rejected. Exploration of this topic will continue in chapter 6. More likely, the dual-channel nature of the C-face graphene is indicative of a band structure change. As graphene layers continue to form on the SiC surface, the individual layers have a greater chance of stacking correctly and forming a different band structure with multiple valence band maxima at the K-point (see for example Ref. 108). Normally

these different bands would be seen simultaneously throughout the sample, but since the probing wavelength is much larger than the thickness of the graphene layers the Drude contributions can be separated into individual physical layers within the model [109].

The best-match model parameters for the p-type channel on the Si-face are $N_s = (1.2 \pm 0.3) \times 10^{12}$ cm^{-2} and $\mu = 794 \pm 80$ cm^{2}V^{-1}s^{-1}. The effective mass is $m^* = 0.027 \pm 0.02\, m_0$. Electrical (DC) Hall effect measurement revealed p-type conductivity with $N_s = (1.9 \pm 0.2) \times 10^{12}$ cm^{-2} and $\mu = 891 \pm 250$ cm^{2}V^{-1}s^{-1}. The correspondence between electrical and optical-Hall effect data is good. A complete accounting of best-match model parameters is given in table 4.1.

Table 4.1: Best-match Drude model parameters for epitaxial graphene on the C-face and Si-face of SiC. The last significant digit of each value is followed by the 90% confidence interval in parenthesis, e.g. 1.1 ± 0.1 is 1.1(1). A lack of a value is signified by (–), see text for details.

Parameter		C-face		Si-face	
		THz-OHE	DC-Hall	THz-OHE	DC-Hall
$N \times 10^{13}$	[cm^{-2}]	5.5(4)	3.0(5)	1.2(3)	1.9(2)
μ	[cm^2/Vs]	1521(52)	3407(250)	794(80)	891(250)
m^*	[m_0]	0.035	–	0.027(2)	–
$N \times 10^{13}$	[cm^{-2}]	3.4(6)	–	–	–
μ	[cm^2/Vs]	18(4)	–	–	–
m^*	[m_0]	0.19[a]	–	–	–

[a] In addition the second layer in C-face graphene exhibited an effective mass field dependence of $(-0.08)\sqrt{B}$.

4.4 Conclusions

The hole-channel mobility, density, and effective mass in epitaxial graphene grown on Si- and C-face 6H-SiC substrates was determined using THz- and MIR-SE and THz-OHE measurements at room temperature. A two-channel and a single-channel conduction process was identified for the graphene grown on C-face and Si-face SiC, respectively. The dual-channel nature of graphene grown on C-face SiC can be explained by changes in the band structure induced by coupling between graphene layers. Electrical Hall effect data are found to be in very good agreement with the optical measurements, validating mid-infrared-THz SE and optical Hall effect as a measurement tool for free charge carrier properties in epitaxial graphene. If epitaxial graphene is to reach the performance of suspended and exfoliated graphene, substrate effects will have to be nullified. Research into these effects will require non-contact and non-destructive measurement of the graphene transport properties.

Chapter 5

Optical Properties of Epitaxial Graphene on SiC Polytypes

Graphene has shown potential for new electronic devices, but harnessing graphene for commercial use requires further development of epitaxial growth processes and a better understanding of the electronic and structural relationships in epitaxial graphene [12, 110]. Currently there is only a limited understanding of the influence of the substrate on the electrical properties of epitaxial graphene. Growth of epitaxial graphene on different polytypes of silicon carbide may provide insight into the various interactions between the substrate and graphene. Graphene growth on the 4H and 6H polytypes of silicon carbide (SiC) was reported on numerous occasions [11, 92, 111–113], and observations showed that both structural and electronic properties of graphene layers differ drastically. Ellipsometry spectra contain unique fingerprints of the electronic properties of semiconductor materials, and are suitable for characterization of electronic band structure parameters [114]. After the fitting process the resulting dielectric functions can be used for monitoring structure-related properties such as strain, as well as for quality control during production.

Presently knowledge of the dielectric function of epitaxial graphene grown on various substrate is not exhaustive. Theoretical calculations predict a van Hove singular-

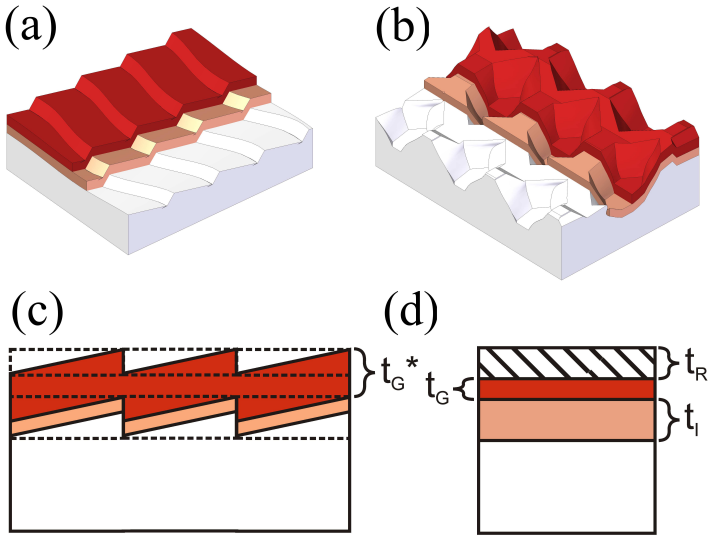

Figure 5.1: (a): Illustration of typical graphene growth on the Si face of 4H SiC. White coloring represents the resulting SiC surface morphology after thermal treatment. Orange coloring represents the interface layer. Red coloring represents graphene. (b): Illustration of graphene growth on the C face of 4H SiC. (c): Illustration of graphene growth on an off-cut axis substrate. Solid lines represent the divisions between the graphene and the void, the graphene and buffer layer, and the buffer layer and the substrate. Dotted lines indicate the plane parallel layers assumed by the ellipsometer. The thickness t_G* is the true thickness of the graphene. (d): Illustration of the final optical model with effective ellipsometric thickness parameters t_R, t_G, and t_I.

ity within the two dimensional Brillouin zone along the six fold degenerate directions between symmetry points **K** and **K'** [19]. Historically absorption around ~4.5 eV has been attributed to the van Hove singularity in highly ordered pyrolytic graphite (HOPG) [115], exfoliated graphene [116, 117], and graphene grown by chemical vapor deposition [118]. It is the goal of this work to explore how the ellipsometric spectra, and hence the dielectric function and critical-point, of graphene grown by high-temperature sublimation of silicon from SiC are changed by the polytype of the underlying SiC.

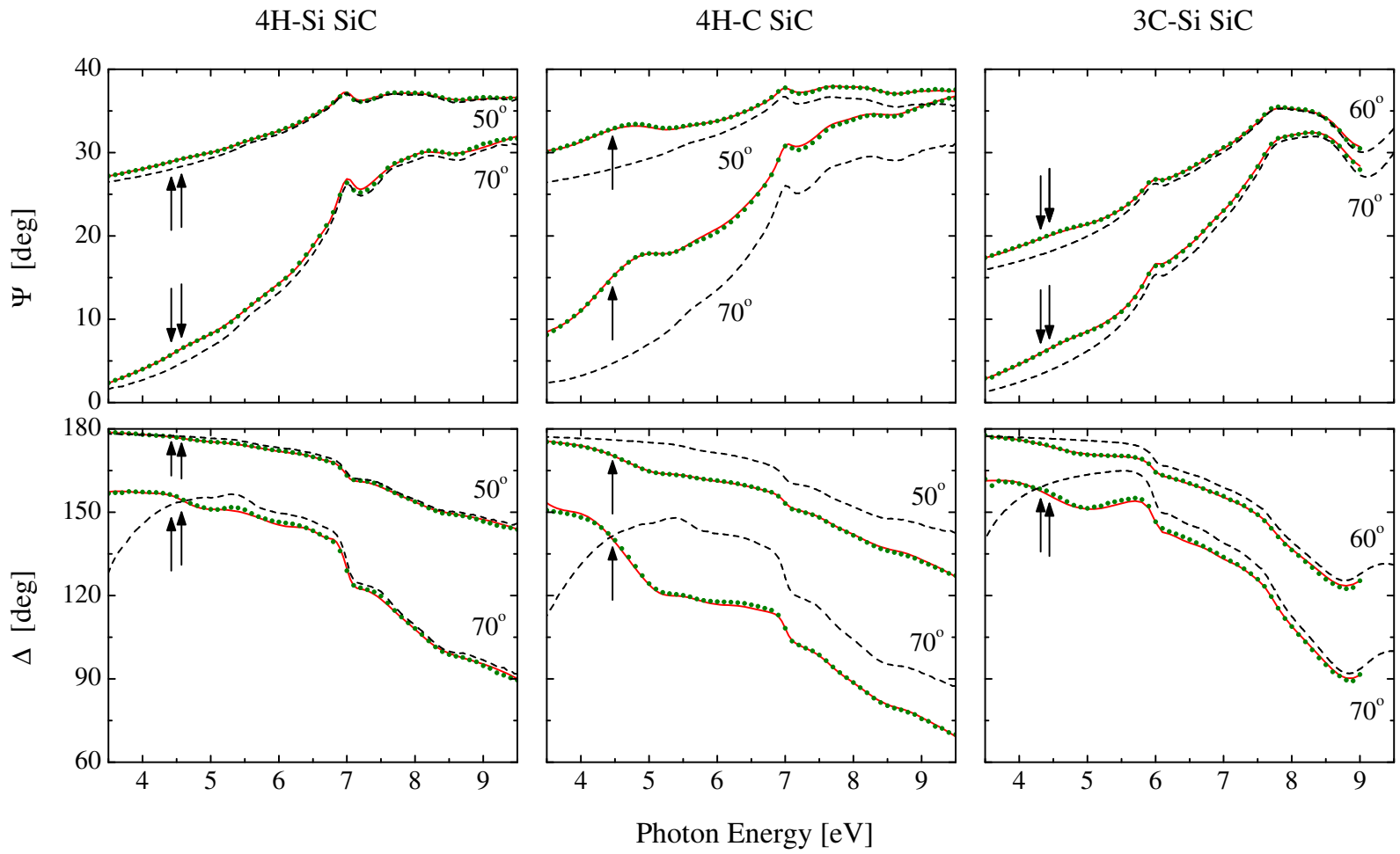

Figure 5.2: Experimental (dotted lines; green) and best-match model calculated (solid lines; red) Ψ and Δ spectra for graphene grown on 4H and 3C SiC compared to bare SiC substrates (dashed lines; black) at incidence angles Φ_a =50°, Φ_a =60°, and Φ_a =70°. Vertical arrowed lines represent the best-match model oscillator energies for each polytype.

5.1 Experiments

The epitaxial graphene samples were grown on 3C, 4H silicon-face, and 4H carbon-face silicon carbide substrates. The dielectric functions for graphene on each SiC polytype are obtained from standard spectroscopic ellipsometry measurements (see section 2.1.4) and subsequent best match model analysis (section 2.1.7). Traditional physical model line shape analysis procedures provide quantitative model parameters for the band-to-band transition characteristics of graphene in the ultra-violet region. We observe that these parameters vary between the different polytypes, and discuss possible causes.

The samples investigated here were formed by high temperature sublimation epitaxy [119] of silicon on the Si (0001) and C $(000\bar{1})$ terminated faces of a 4H SiC substrate (4H-Si and 4H-C). Similarly, epitaxial graphene was formed on a thick epitaxial 3C SiC layer, with the 3C SiC layer grown on the Si face of a 6H SiC substrate [120]. This 3C sample is has a (111) orientation and is Si terminated (3C-Si). Samples were stored in normal ambient after growth and not treated further. Standard spectroscopic ellispometry measurements were carried out on the 4H-Si, 4H-C, and 3C-Si samples before and after epitaxial graphene growth. Bare 3C and 4H substrates were measured to determine the dielectric response of the silicon carbide polytypes without graphene. All measurements were performed upon reflection of the sample, on a J.A. Woollam VUV-302 VASE ellipsometer in a nitrogen-purged environment. Measurements were performed in the visible to ultra-violet spectrum with photon energies from 3.5 to 9.5 eV, in increments of 0.05 eV, at 50°, 60°, and 70° angles of incidence. As mentioned in section 2.1.6 the VUV-302 ellipsometer is capable of measurements down to 0.75 eV. Experimental results for the 0.75 to 3.5 eV spectral region are not reported here due to an inability to correctly model the

SiC substrates in this region. Silicon carbide is a uniaxial material, and the slight difference between the on- and off-axis dielectric functions creates a noticeable change in the reflected polarization in the transparent portion of the SiC spectrum. In this spectral region the probe beam of the ellipsometer can penetrate the entire thickness of the substrate, creating a change in the polarization related to the wavelength being measured. For an example of this behavior see reference 121, where below 3.5 eV the dielectric function appears to oscillate with respect to the wavelength. The effect on the dielectric function is subtle and extremely difficult to model.

Standard spectroscopic ellipsometry determines the ratio ρ of the complex-valued Fresnel reflection coefficients r_p and r_s and is commonly presented by parameters Ψ and Δ where $\rho = r_p/r_s = \tan(\Psi)e^{i\Delta}$ as will be done here. Figure 5.2 depicts experimental and best-match model calculated Ψ and Δ spectra from all investigated samples. The experimental data reveal large differences between the Si and C faces of the 4H SiC sample, whereas bare substrate measurements yielded matching Ψ spectra for both Si and C faces. The differences exhibited in figure 5.2 between the Si and C faces are due only to the expitaxial graphene properties, including thickness. While this influence is seen most strikingly at the critical-point peak caused by the van Hove singularity, occuring here at photon energies around 4.5 eV, graphene influences the entire spectroscopic response from 3.5 to 9.5 eV. Note that the 3C spectra in figure 5.2 are limited due to lack of reflected light intensity above 9 eV.

5.2 Optical Model and Analysis

A stratified layer optical model composed of a substrate, an interface layer between the substrate and the graphene, a graphene layer, and a roughness layer between the graphene and air (see figure 5.1) is used here to analyze the ellipsometric data. All

layers are treated isotropically in our model since ellipsometry has no sensitivity to the out-of-plane polarizability of ultra-thin layers [16, 52]. The uniaxial nature of SiC can be ignored at photon energies above the transparent region and treated isotropically. Experimental Ψ and Δ spectra, obtained from bare 4H and 3C SiC substrates, were analyzed by utilizing a sum of broadened harmonic oscillator lineshapes as the model dielectric function. The best-match model dielectric functions are equivalent to those reported previously for 4H [122, 123] and 3C [121] SiC, but are omitted here for brevity. The best-match model dielectric function parameters were then used in the analysis of the epitaxial graphene samples but were not further varied. The graphene model dielectric function is composed of Lorentzian and Gaussian oscillators such that $\varepsilon = 1 + \varepsilon^L + \varepsilon^G$ [118]:

$$\varepsilon^L(E) = \frac{A_L \gamma_L}{{E_L}^2 - E^2 - \mathrm{i}\gamma_L E}, \tag{5.1}$$

$$\Im\{\varepsilon_2^G(E)\} = A_G \left[\mathrm{e}^{-\left(\frac{E-E_G}{\sigma}\right)^2} + \mathrm{e}^{-\left(\frac{E+E_G}{\sigma}\right)^2} \right] \quad \text{with} \quad \sigma = \frac{\gamma_G}{2\sqrt{\ln(2)}}, \tag{5.2}$$

$$\Re\{\varepsilon_1^G(E)\} = \frac{1}{\pi}\mathcal{P}\int \frac{\varepsilon_2^G(E')}{E' - E}\,\mathrm{d}E', \tag{5.3}$$

where $A_{L,G}$, $E_{L,G}$, and $\gamma_{L,G}$ denote the amplitude, the critical-point transition energies, and the broadening of the Lorentzian and Gaussian oscillators, respectively, and $\mathcal{P}$ denotes the cauchy principal value.

On 4H-Si and 3C-Si sublimation of silicon first forms a carbon buffer layer whose atoms are strongly bonded to the substrate and form a $(6\sqrt{3} \times 6\sqrt{3})\mathrm{R}30^\circ$ surface reconstruction [13, 124, 125], while on 4H-C there is no unique surface reconstruction [126]. In the optical model used here the interface layer accounts for this buffer layer, and also the roughness of the substrate surface, an effect of the slight off-axis cut

of the SiC substrate and non-uniform sublimation of silicon from the SiC substrate. A Bruggeman effective medium approximation (EMA) comprised of 50% substrate and 50% graphene was used to create a suitable model dielectric function for the combined effect of the buffer layer and surface roughness in a single interface layer. This is shown graphically in figure 5.1. The only varied parameter during the data analysis that was unique to the interface layer was its thickness (t_I). Likewise, a surface roughness layer modeled with another Bruggeman EMA comprised of 50% graphene and 50% ambient was implemented with a thickness t_R. During data analysis, the thicknesses of the surface roughness layer (t_R), epitaxial graphene layer (t_G), and the interface layer (t_I), and the graphene model dielectric function parameters are varied until best-match between experimental and model calculated Ψ and Δ spectra is achieved. Best-match model parameters for each surface are presented in table 5.1. We note that the resulting graphene layer thickness for 4H-Si and 3C-Si are closer to the ideal graphene monolayer thickness than 4H-C, which forms multilayer graphene (see table 5.1).

5.3 Results and Discussion

Figure 5.3 presents the imaginary part (ε_2) of the best-match model dielectric function obtained here for graphene on 3C and 4H SiC in comparison with theoretical results obtained by Yang *et al.* [127] for graphene and graphite. The ε_2 spectra are dominated by the critical-point transition [116–118]. Comparing the critical-point peak energies* of graphene (4.53 eV) and graphite (4.37 eV) in figure 5.3 reveals that 4H-Si has a best-match model energy closest to that of graphene, with a value of 4.51 eV. This observation is corroborated by the E_G and γ_G parameters, which are proportional to

*The critical point peak energies of which are located between E_L and E_G were determined using the numerical derivative of ε_2 spectra in figure 5.3.

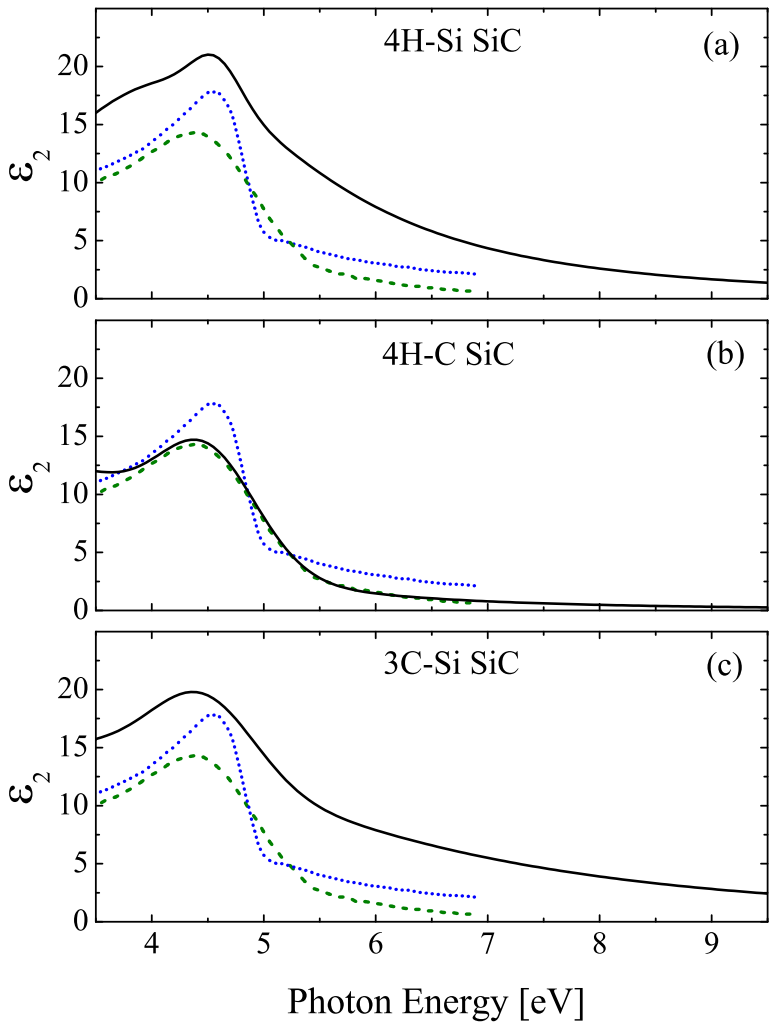

Figure 5.3: Imaginary part of the dielectric function for epitaxial graphene relative to substrate polytype (solid lines; black) with theoretical graphene- (dotted lines; blue) and graphite- (dashed lines; green) exciton enhanced dielectric functions from Yang *et al.* [127].

the critical-point peak energies, and show agreement between the 3C-Si and 4H-C samples while the 4H-Si sample shows a higher E_G and lower γ_G. Together these parameters show that while the carbon film on 3C-Si is thin (mono- or bi-layer), it has an electronic structure similar to graphite. This is attributed to the relatively high defect density on the as-grown 3C substrate, which leads to the formation of thick graphite-like islands during the sublimation (see chapter 7 and reference 128). It is noteworthy that the 3C-Si sample exhibits the dielectric function of graphite and is far from that of amorphous carbon [129]. All of the samples studied here required only one critical-point peak energy between 3.5 and 9.5 eV, in contrast to predictions by Trevisanutto *et al.* [130] of an exitonic resonance between 8.3 and 9.6 eV. Similarly, Pellagrino, Angilella, and Pucci predict multiple critical-points with shifting energies for graphene under strain, suggesting that none of the investigated samples have significant strain to alter the optical conductivity [131].

Examination of figure 5.3(a,c) shows a heightened polarizability throughout the spectrum for the 4H-Si and 3C-Si samples in contrast to figure 5.3(b) for the 4H-C sample. This increased polarizability can be attributed to either the $(6\sqrt{3}\times 6\sqrt{3})$R30° surface reconstructed carbon buffer layer of the 4H-Si and 3C-Si samples, or a charge transfer from the SiC substrate predicted by Varchon *et al.*[132] In order for doping to affect the model dielectric function above 3.5 eV uniformly, both the mobility and free charge carrier concentration must be extraordinarily large, which suggests the cause of the increased polarizability is not due to free charge affects. Note that the current model dielectric function does not include affects from plasmons or changes in the Fermi level, and that these could also cause the observed changes in the dielectric function.

The graphene thickness parameter for the 4H-Si and 3C-Si samples is smaller than the 0.35 nm value given by Varchon *et al.* [132] for monolayer graphene. This may be

due to the fact that the actual surface morphology is influenced by substrate defects and uneven Si sublimation, and is not accounted for in the plane parallel layer model employed here. Surface morphology illustrations are presented in figure 5.1(a,c) as described in reference 133. Morphology considerations then also explain the large thickness of the interface layer (t_I) for 4H-C and 3C-Si, as the true graphene thickness is partially hidden in the ellipsometric interface thickness parameter t_I. An illustration of this concept is shown in figure 5.1(b,c).

Table 5.1: Best-match model parameters of graphene on SiC substrates. The error limits given in parenthesis denote the uncertainty of the last significant digit (90% reliability). Film thicknesses are listed in physical order from ambient to substrate. The peak energy of the critical point is designated as CP Peak.

Parameter		3C-Si	4H-Si	4H-C
A_L	–	13(5)	18(1)	11.7(1)
E_L	(eV)	4.3(3)	4.44(5)	3.37(2)
γ_L	–	6.2(5)	3.3(1)	2.17(5)
A_G	–	6(3)	3.5(5)	9.6(2)
E_G	(eV)	4.46(5)	4.58(2)	4.486(6)
γ_G	–	1.1(1)	0.50(7)	1.06(2)
CP Peak	(eV)	4.37	4.51	4.38
t_R	(nm)	0.2(3)	0.09(5)	0.075(6)
t_G	(nm)	0.1(2)	0.14(9)	2.04(3)
t_I	(nm)	0.8(7)	0.4(1)	2.90(9)

5.4 Conclusions

In this chapter spectroscopic ellipsometry measurements performed on epitaxial graphene grown on the 4H and 3C polytypes of SiC were presented. The best-match model dielectric functions for the graphene layer on each growth surface exhibited a critical-point peak which allowed comparison to theoretical predictions for the di-

electric function of graphene and graphite, and determination of graphene quality, morphology, and strain. Epitaxial graphene grown on 4H-Si exhibited a model dielectric function closest to that of theoretical graphene, while graphene grown on 3C-Si and 4H-C exhibited a model dielectric function similar to graphite, despite a 3C-Si graphene thickness indicative of monolayer graphene, which is most likely due to defects in the 3C-SiC epilayer. The carbon buffer layer present on the 3C-Si and 4H-Si samples produces an increased polarizability throughout the visible to ultra-violet spectrum. None of the samples investigated exhibited multiple critical-points in the model dielectric function indicative of graphene under strain.

Chapter 6

A Band Structure Based Model Dielectric Function for Graphene and Graphite

Ellipsometry has proven a valuable technique for determining the optical properties and thickness of thin films [17], making it a natural choice for determining the properties of graphene and graphite. While several methods have been used to analyze ellipsometric data of graphene and graphite, no method has yet given accurate optical properties and provided physically relevant information about the sample measured. In this chapter we endeavor to provide a model dielectric function which allows accurate reproduction of both graphene and highly ordered pyrolytic graphite (HOPG) optical properties from the near-infrared to the vacuum ultra-violet spectra with a physically relevant parameterization.

As graphite has been a subject of considerable research since the first band structure calculations in the 1947 [134, 135], it would seem prudent to start with an accepted model dielectric function for HOPG and work towards an understanding of graphene. However, the optical properties of HOPG have yet to be completely determined, the most recent addition to the literature coming in 2007 [136]. HOPG optical properties have yet to be fully reconciled with band structure calculations, with many scaling the calculations such that the $\pi - \pi^*$ transition matches the ob-

served ~4.6 eV optical absorption peak [115, 137–145]. There are several issues with this interpretation. First, this scaling should produce a second absorption peak from $\sigma - \sigma^*$ transitions well below the observed ~14 eV peak seen in reflection experiments [115, 140, 146]. Second, attempts to broaden the asymptotic peak calculated from the saddle point in the band structure reduce the peak amplitude well to below the observed value [144]. Finally, this interpretation predicts that the number of peaks and their resonant energies due to saddle points in the band structure should change between HOPG and graphene, yet both show the same absorption peak at the same resonant energy. [117, 118, 147–149]

Previous analysis methods of ellipsometry and optical absorption experiments on graphene include the constant conductivity model [107, 150–153], numerical inversion of the optical properties with a presumed thickness [116], two harmonic oscillators used as the model dielectric function [118, 128, 147, 154], implementation of a B-spline as the model dielectric function [117], use of the configuration interaction function as an absorption model [148, 149], and implementation of the standard critical point model [155]. Each of these methods has unique advantages and disadvantages but none meet the desired criteria. Numerical inversion can produce reliable optical properties but requires a generalized ellipsometry experiment to account for the material anisotropy and does not provide insight to the optical features found. Utilization of a model dielectric function allows sensitivity to the optical thickness by unifying the real and imaginary parts of the dielectric response via the Kramers-Krönig transform. Both the dual-oscillator model dielectric function and the B-spline model dielectric function thus allow sensitivity to the optical thickness, but neither gives insight into the physical causes of the spectral features described and neglects anisotropy in the material. In addition, the dual-oscillator model has difficulty reproducing the characteristically asymmetric absorption seen in the graphene spectrum at ~4.6 eV, and

fails to address the shoulder peak seen in both HOPG and graphene ~6 eV [137, 156].

Chae *et al.* made the first advancement in understanding the underlying causes of graphene's absorbance features by using the asymmetric configuration interaction function as a model for exciton based absorption. Mak *et al.* verified this approach in the visible spectrum and improved upon it by adding an inter-band transition outside the experimental spectrum. Both articles suggest that a van Hove singularity, in this case a $2D - M_1$ critical point should exist at a higher energy, leading to the development of a standard critical point model for graphene [155]. Using a $2D - M_1$ critical point modified with the configuration interaction function both the asymmetric ~4.6 eV and ~6 eV shoulder peaks can be described, with the high energy critical point responsible for the shoulder peak. This critical point model fails at lower energies due to the vanishing band gap of graphene, where it predicts an infinite inter-band absorption at a static electric field and is therefore not useful for modeling optical data in the mid-IR, far-IR, and THz spectral regions, where the free-charge carrier based Drude model has been effective [45].

6.1 Theory

Presented here is a complete set of functions that will allow efficient numeric computation of the graphene dielectric function for the purpose of fitting ellipsometric data while staying consistent with all previously reported results for graphene. The electronic band structure of graphene based on next-neighbor electron interaction between π-bonds can be described by a simple formula first derived by Wallace [135], which is reproduced in equation 6.1,

$$E = \pm t \left[1 + 4\cos\left(\frac{3k_x a}{2\sqrt{3}}\right)\cos\left(\frac{k_y}{2}\right) + 4\cos^2\left(\frac{k_y a}{2}\right)\right]^{\frac{1}{2}}, \tag{6.1}$$

where t is the next neighbor hopping energy and a is the lattice constant (1.42 Å). In this case t is the next neighbor hopping energy as described by the Hubbard model, minus the typical term describing on-site repulsion (U). The joint density of states per unit cell can then be calculated for graphene by the integration over constant energy contours of the inverse gradient of equation 6.1, which has been expressed in a more convenient format by Stauber *et al.* [19] and retains the dependence on t;

$$J_{cv}(E) = \frac{4E}{t^2\pi^2} \begin{cases} \dfrac{1}{\sqrt{F(E/t)}} K\left(\dfrac{4E/t}{F(E/t)}\right), & 0 < E < t \\ \dfrac{1}{\sqrt{4E/t}} K\left(\dfrac{F(E/t)}{4E/t}\right), & t < E < 3t \end{cases} \tag{6.2}$$

where the functions $K(m)$ and $F(x)$ are defined as

$$F(x) = (1+x)^2 - \frac{(x^2-1)^2}{4} \text{ , and} \tag{6.3a}$$

$$K(m) = \int_0^1 [(1-x^2)(1-mx^2)]^{-\frac{1}{2}} \mathrm{d}x \text{ .} \tag{6.3b}$$

Equation 6.3b is the complete elliptic integral of the first kind and thus can be easily evaluated numerically via the arithmetic-geometric mean. Recognizing that the line-shape generated by equation 6.3b is similar to $|\ln(E - E_0)|$ which describes ε_2 for an electronic saddle point in a 2D material in the critical point model [114], it is tempting to forgo the integration entirely. However since the joint density of states is proportional to the energy E and acquires a factor of $1/E^2$ the critical point model results in $\varepsilon_2 \propto 1/E$ and more specifically $\varepsilon_2(0) = \infty$. Under the assumption of a constant conductivity for graphene in the visible spectrum we would expect that $\varepsilon_2 \propto 1/E$, but in general we require that interband transitions cease as the incident photon energy approaches zero. Part of this requirement is that the critical

point model relies upon the Kramers-Krönig relations to compute ε_1 from ε_2, and an infinite value for ε_2 anywhere in the spectrum is not only unphysical but produces infinite values for ε_1 over the entire spectrum. Enforcement of $\varepsilon_2(0) = 0$ (neglecting free charge carriers) is achieved by introducing Fermi's golden rule as applied to optical inter-band transitions. Kim *et al.* [157] have provided a useful variation of the formula that correctly implements broadening by folding the transition rate with a broadening function, which is reproduced in equation 6.4;

$$\varepsilon(E) = 1 - \frac{8\pi\hbar^2 e^2}{m^2} \sum_{c,v} \int J_{cv}(E') \left(\frac{P_{cv}(E')}{E'} \right)^2 B(E') \, \mathrm{d}E' \tag{6.4}$$

where m is the free electron mass, $B(E')$ is a spectroscopic broadening function, and $P_{cv}(E')^2$ is the momentum matrix element. The summation is between all bands whose energy gap is within the spectral range of the ellipsometer. Aside from allowing equation 6.2-6.3b to be used directly, other advantages granted by using equation 6.4 are inherent Kramers-Krönig consistency and the ability to include absorption from alternative sources, for example the free charge carriers in chapter 4, by adding the requisite terms to equation 6.4. The broadening function $B(E')$ is given by the integrals in equation 6.5.

$$B(E') = \int_0^\infty e^{is[E-E'+i\gamma(s)]} \mathrm{d}s - \int_0^\infty e^{is[E+E'+i\gamma(s)]} \mathrm{d}s \tag{6.5}$$

where i is the imaginary unit and $\gamma(s)$ is a function which can be expanded in terms of a Taylor series. Expansion to the first two terms yields $\gamma(s) = \Gamma + 2\sigma^2 s$. When $\gamma(s) = \Gamma$ the broadening is said to be Lorentzian and equation 6.5 reduces to a simple harmonic oscillator, where $B(E')$ becomes

$$B(E') = \frac{1}{\pi} \left(\frac{1}{E - E' - i\Gamma} - \frac{1}{E + E' - i\Gamma} \right) . \tag{6.6}$$

If $\gamma(s) = 2\sigma^2 s$ then the broadening is said to be Gaussian, and the terms of the broadening integrals in equation 6.5 can be rearranged by completing the square into the form:

$$B(E') = \left(e^{-(E-E')^2/8\sigma^2} \int_{-i(E-E')/2\sqrt{2}\sigma}^{\infty} e^{-u^2} \mathrm{d}u \right) - \left(e^{-(E+E')^2/8\sigma^2} \int_{-i(E+E')/2\sqrt{2}\sigma}^{\infty} e^{-u^2} \mathrm{d}u \right), \tag{6.7}$$

where the substitution $u = \sqrt{2}\sigma s - i(E \mp E')/2\sqrt{2}\sigma$ results in the Faddeeva plasma dispersion function. The complex error function can be numerically computed with an expansion to an accuracy of 10^{-9} or less [158].

It has been shown in several articles (for example, references 127, 148, 149) that the absorption seen in graphene at ~4.5 eV is not an inter-band transition at the $2\mathrm{D} - \mathrm{M}_1$ critical point (M-point) described by equation 6.2 – which should occur close to ~6 eV – but is instead a many-body effect with a line-shape described by the configuration interaction [159]. Here we consider the many-body effect to be a two dimensionally confined Wannier-Mott exciton series with resonant energies $E_e = 2t - E_b(n + \frac{1}{2})^{-2}$, where E_b is the binding energy of the exciton. The exiton series is implemented as a perturbation, as described in the appendix of reference 159, where each exciton state independently interacts with the background continuum of available states and is influenced by the probability that the electron and hole are found in the same unit cell ($|\Phi_0|^2$), such that $|\Phi_0|^2 = 2V_0(\pi a^3(n + \frac{1}{2})^3)^{-1}$ [114, 160, 161]. Note that in equation 6.8a we normalize by the probability $|\Phi_0|$ such that the volume (or area) of the unit cell (V_0) and the Bohr radius of the exciton (a) become inconsequential. This is done so that when the photon energy E is zero equation 6.8a is equivalent to one, preserving the constant conductivity model at low photon energies. The result is the following formula specific to 2D Wannier-Mott exciton states located at the M-point

in the band structure of graphene,

$$\left(\frac{P_{cv+e}(E)}{P_{cv}(E)}\right)^2 = \sum_{n=0}^{\infty}\left(\frac{|\Phi_0|^2}{|\Phi_0|^2_{E=0}}\right)\frac{(q+\epsilon)^2}{1+\epsilon^2} \quad \text{where} \tag{6.8a}$$

$$\epsilon = \frac{E - E_e - T(E_e)}{\frac{1}{2}\Gamma_f(E_e)} \qquad \text{and} \tag{6.8b}$$

$$T(E_e) = \mathcal{P}\int \frac{\Gamma_f(E')}{2\pi(E_e - E')}dE' \ , \tag{6.8c}$$

which can be used to directly modify the momentum matrix element in equation 6.4. In equation 6.8a q represents the ratio of two probabilities; that of a transition to a modified exciton state to that of a transition to a continuum of states of width Γ_f. The function $\Gamma_f(E)$ is broadening associated with the strength of the configuration interaction and $T(E)$ is a shift in the resonant energy experienced when Γ_f changes rapidly with energy, and is zero when Γ_f is a constant. Note the similarity between the derived dependence of $T(E)$ on $\Gamma_f(E)$ and the Kramers-Krönig transform, which suggests that $T(E)$ and $\Gamma_f(E)$ are the real and imaginary parts of a single complex function. As per reference 159 we expect $\Gamma_f(E)$ to change in proportion to the resonant energies of the exciton series, and thus be relatively parabolic. Rather than numerically computing the Cauchy principal value integral in equations 6.8 we choose $\Gamma_f(E)$ so that the integration can be analytically solved. Both of these requirements can be met with a simple harmonic oscillator function $L(E_e)$ such that;

$$L(E_e) = \frac{A_f B_f (2t - E_b)}{(2t - E_b)^2 - E_e^2 + B_f^2/4 - iB_f E_e}, \tag{6.9a}$$

$$\frac{1}{2}\Gamma_f(E_e) = \Im[L(E_e)] = \frac{16 A_f B_f^2 (2t - E_b) E_e}{\prod_{\pm}[B_f^2 + 4(2t - E_b)^2 \pm 8(2t - E_b)E_e + 4E_e^2]}, \quad \text{and} \tag{6.9b}$$

$$T(E_e) = \Re[L(E_e)] = \frac{4A_f B_f (2t - E_b)[4(2t - E_b)^2 - 4E_e^2 + B_f^2]}{\prod_{\pm}[B_f^2 + 4(2t - E_b)^2 \pm 8(2t - E_b)E_e + 4E_e^2]}, \tag{6.9c}$$

where A_f is the amplitude of the harmonic oscillator function and B_f is the broadening term that dictates the decrease in Γ_f as n increases. Note that due to the placement of the $n = 0$ exciton as the center energy, it experiences no energy shift [$T(E_e|_{n=0}) = 0$]. Because only the ratio of probabilities is known, P_{cv}^2 is not entirely canceled by equation 6.8, and can be moved outside the integration as a constant. We then combine constants into the amplitude parameter $A = 8(\hbar e P_{cv})^2/(m^{*2} A_c)$, with the area of the graphene unit cell A_c added to convert J_{cv} from states per unit cell to states per square area. The result is that eqs. 6.2-6.9 can be used over a wide spectral range at the expense of the ability to separate the different elements of A, such as P_{cv} and the effective mass m. All of the previous equations can be combined into equation 6.10, which has free parameters A, t, q, E_b, A_Γ, B_Γ, and either Γ or σ, with the high energy pole parameters A_p and E_p, and the free charge absorption parameters of resistivity (ρ) and mean scattering time (τ):

$$\varepsilon(E) = 1 \underbrace{- \sum_{c,v} A \int \frac{J_{cv}(E')}{E'^2} \left(\frac{P_{cv+e}(E')}{P_{cv}(E')} \right)^2 B(E') \, \mathrm{d}E'}_{\text{interband transitions with excitons}} \underbrace{+ \frac{A_p E_p^2}{E_p^2 - E^2}}_{\text{high energy pole}} \underbrace{- \frac{\hbar^2}{\varepsilon_0 \rho (\tau E^2 + i\hbar E)}}_{\text{free charge}} \cdots \tag{6.10}$$

For the purpose of numeric computation equation 6.3b is evaluated via the arithmetic-

geometric mean with a tolerance of 10^{-3}, and the integral in equation 6.10 is computed with adaptive two-point Gaussian quadrature with a relative tolerance of 10^{-6}. These values were chosen for acceptable accuracy with minimum compute time, resulting in the computation of a single Ψ and Δ spectrum quickly enough to be used in established Levenburg-Marquardt fitting procedures. For the purposes of fitting the ellipsometric data we assume that the next-nearest neighbor hopping energy $t' = 0$, or that the π and π^* bands are symmetric around the Fermi level, which is located at the Dirac point. In the case of graphene equation 6.10 is then complete over the 0-9 eV spectral range, and the summation can be discarded as only one set of conduction and valence bands is considered. As more layers are added the π bands split for each layer, eventually degenerating into four π bands in HOPG [108, 139, 142, 143, 162–164]. For HOPG the model as described in equation 6.10 is physically incorrect as t no longer represents the next-neighbor hopping energy but the difference between the highest valence band and one of the conduction bands at the M-point. This splitting results in a band separation at the K-point, which can be accounted for with a $1\mathrm{D} - \mathrm{M}_0$ critical point model, shown in equation 6.11,

$$J_{gap}(E) = \begin{cases} 0, & E < E_g \\ \dfrac{A_g}{\sqrt{E - E_g}}, & E_g < E < E_c \end{cases} \tag{6.11}$$

where E_g is the associated energy gap between π^* bands at the K-point and E_c is the cutoff energy. A_g is an amplitude parameter which is set such that $J_{cv}(E_c) = J_{gap}(E_c)$. The choice of a 1D critical point model is further discussed in section 6.3.

Graphene and HOPG are considered uniaxial materials, with the extraordinary optical axis perpendicular to the sample surface. In the case of graphene the extraordinary dielectric function (in terms of the sample coordinate system, $\varepsilon_1^z(E)$) is

unity, as there is no possible optical transition to the fused silica substrate until higher photon energies than those in the measured spectral range. Optical transitions between Van der Waals bonded graphene sheets in HOPG are allowed at lower energies, but not low enough to exist inside the measured spectral range. For this reason we use the same approach as Kravets *et al.*, such that for HOPG $\varepsilon_2^z(E) = 0$ and the real part of the dielectric function follows a Cauchy dispersion, where $n_e(E) = \sqrt{\varepsilon_1^e(E)} = A_n + B_n E^2(0.65) + C_n E^4(0.423)$, with conversion factors to wavelength in µm given in parenthesis.

6.2 Experiments

Standard ellipsometry experiments as described in section 2.1.4 were conducted on both graphene and HOPG. A spectral range of 0.75 - 9 eV was used on a J.A. Woollam VUV-302 ellipsometer in a nitrogen purged atmosphere. The VUV spectral range was chosen to produce the largest change in the ellipsometric parameter Δ, which is proportional to the ratio of the film thickness to the wavelength of light used. Angles of incidence with respect to the sample normal were set at 65°, 70°, and 75° for graphene with an additional angle of 80° for HOPG. It is assumed that the sample normal is aligned with the c crystal axis and the z sample axis for all experiments and subsequent analyses in this work. Experiment data for ellipsometric parameters Ψ and Δ for both CVD graphene and HOPG are presented in fig. 6.1 alongside a best-match model as defined in sec. 6.1.

Graphene was grown via chemical vapor deposition on 25 µm Cu foil and transferred by the wet method described in reference 3 to an optical quality fused silica substrate. Fused silica was chosen as the graphene substrate because SiO_2 on Si substrates are the most common substrates transferred to, partially because the graphene

can be visually identified easily on a 300 nm thermal SiO_2 layer due to contrast [165]. A SiO_2 on Si substrate was not used for the ellipsometry experiments as the thermal SiO_2 layer causes significant interference effects and because ε_2 of Si is non-zero throughout the spectral range, thus any absorption might be attributed to a combination of these effects and not graphene. Choosing a pure fused silica substrate allows any absorption to be attributed directly to the graphene layer.

High quality HOPG was provided by Arthur Moore formerly of Union Carbide, and was mechanically cleaved prior to measurement. Additional ellipsometry data for HOPG was taken from Jellison *et al.* (reference 136) in order to demonstrate the cause and effect of different modeling decisions in section 6.3.3.

6.3 Results and Discussion

6.3.1 Experiment and Model Error

Experimental data are fit with equation 6.10 by iteratively adjusting the free parameters in sec. 6.1 until a minimum error between data and model is achieved. The resulting set of free parameters is referred to as the best-match model, and are shown in table 6.1. Figure 6.1 plots the experimental Ψ and Δ data values against the best-match model calculations, with excellent agreement. As seen in table 6.1, the mean square error (MSE) between best-match model calculation and experimental data is close to one for both analyses, indicating that the difference between the best match model and experimental data is close to to the experimental standard deviation between rotations of the analyzing polarizer. The average standard deviation in Ψ and Δ values between analyzer rotations is less than half of a degree for both experiments, with $\bar{\sigma}_{rot} = 0.477$ for graphene and $\bar{\sigma}_{rot} = 0.294$ for HOPG. Low experimental error confirms the existence of the high energy shoulder peak first observed by Greenaway

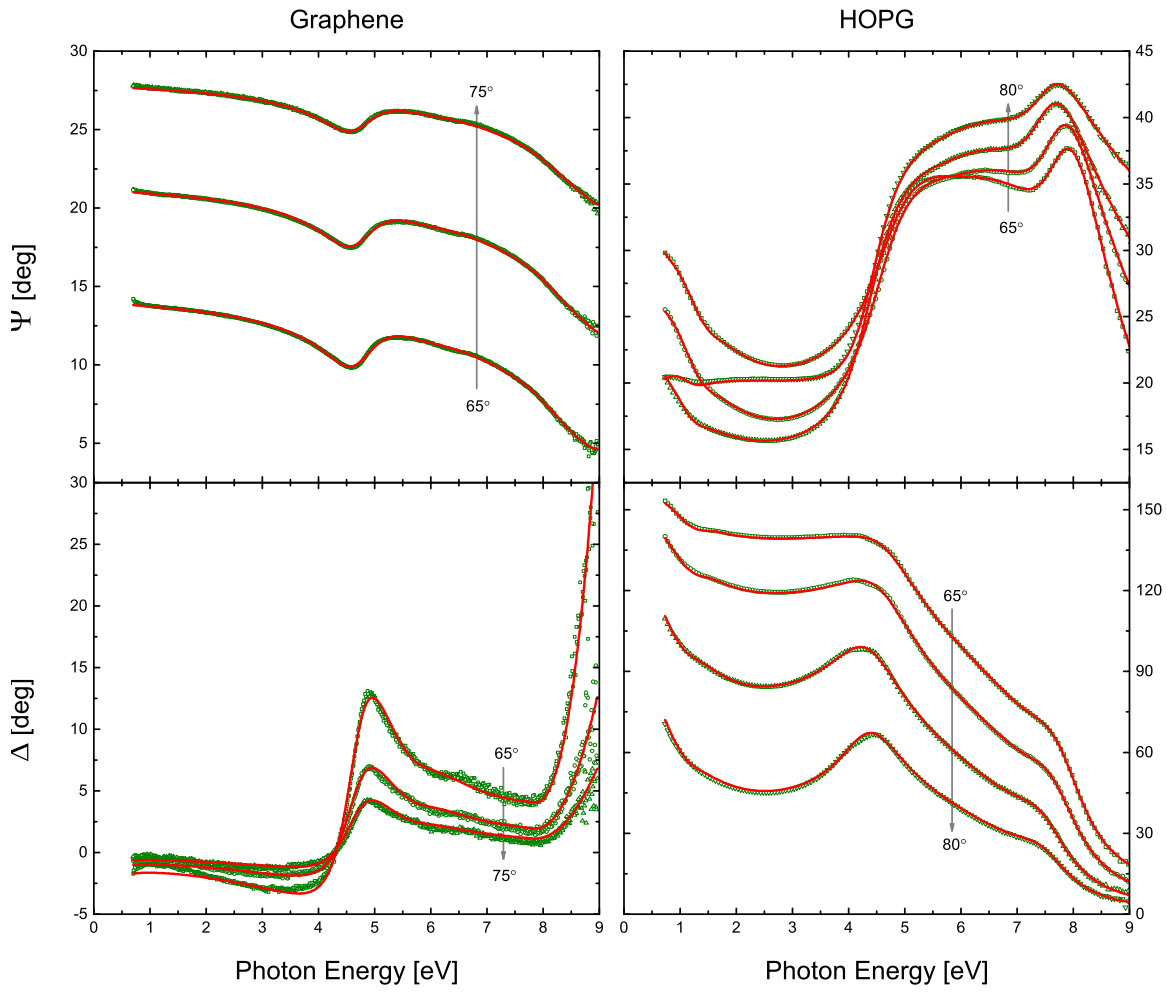

Figure 6.1: Experimental Ψ and Δ values for graphene and HOPG from 0.7 to 9 eV (green symbols) plotted behind best-match model calculations (red lines). Data was taken at 65°, 70°, and 75° incident angles for graphene and 65°, 70°, 75°, and 80° incident angles for HOPG. Symbols are not sized with respect to error as the data would be too small to be visible.

et al. in HOPG, visible as five and seventy degree magnitude features for graphene and HOPG respectively in the Δ spectrum of fig. 6.1. The larger standard deviation for the CVD graphene experiment is attributed to the eight to nine eV spectral range in which the graphene becomes transparent and the fused silica substrate becomes opaque.

6.3.2 The Graphene Dielectric Function

Best-match model parameters in table 6.1 can be used with equations 6.2-6.11 to generate the best-match in-plane model dielectric function for both graphene and HOPG as shown in fig. 6.3. For graphene, the in-plane dielectric function ε_2^{xy} follows the constant conductivity model based on the fine structure constant from the near-IR to ~1.5 eV. Theoretically graphene should have a conductivity of $\pi\alpha$ while the joint density of states from equation 6.2 is linear with respect to energy. We would then expect the constant conductivity model to be valid through the next-neighbor hopping energy t, which is ~3 eV (see references [19, 166–168] and others). Instead we observe a departure from $\pi\alpha$ attributed to increasing excitonic absorption. Above ~1.5 eV our best-match model dielectric function is in excellent agreement with the results of Kravets *et al.* in reference 116, who implement a similar modeling approach. The model used by Kravets *et al.* differs from that presented in this work by the thickness of the graphene sheet. Here a finite thickess is assumed as part of the layered ellipsometry model, while Kravets *et al.* utilize an ideal 2D sheet. The result is a slight offset in ε_1^{xy}, with an otherwise identical dispersion. Our best-match model dielectric function is also in agreement with that of Nelson *et al.* below ~5 eV [118], above which the limitations of the dual-oscillator based model dielectric function become apparent. As shown in equation 6.4, model dielectric functions can be completely assembled out

Table 6.1: Best-match in-plane model parameters for graphene and HOPG. The error limits given in parenthesis denote the uncertainty of the last significant digit (90% reliability). Values with no parenthesis are fixed. Units for each parameter are shown in brackets.

Parameter		Graphene	HOPG	
		$\pi - \pi^*$	$\pi - \pi_1^*$	$\pi - \pi_2^*$
MSE	–	0.609	1.123	
d	[Å]	3.34(4)	–	–
A	[eV]	305(4)	91(4)	120(4)
t	[eV]	2.907(9)	3.056(3)	3.350(4)
q	–	−2.40(1)	−5.6(3)	−4.49(6)
E_b	[eV]	0.423(4)	0.438(9)	0.501(2)
A_f	[eV]	1.38(1)	1.42(6)	0.305(8)
B_f	[eV]	28.3(3)	0.25(1)	0.25
Γ	[eV]	0.211(4)	0.64(3)	0.248(8)
A_p	–	0.31(1)	1.571(9)	
ρ	[Ω-cm]	–	$6.45(6) \times 10^{-6}$	
τ	[s]	–	$4.96(5) \times 10^{-16}$	
E_g	[eV]	–	–	0.8051(8)
E_c	[eV]	–	–	1.533(4)

of a summation of harmonic oscillators. It is then tempting to add a third oscillator to the model dielectric function proposed by Nelson *et al.* in order to improve the asymmetry of the ~4.6 eV absorption and include the ~6 eV shoulder peak. Such a model would require nine free parameters with an amplitude, resonant energy, and broadening for each harmonic oscillator. The model proposed in section 6.1 accomplishes the same task with only seven free parameters (not including the amplitude parameter A), which improves the accuracy with which free parameters can be determined from fitting to experimental data. An identical argument can be made against the model dielectric function proposed by Gray *et al.* [169] The B-spline model dielectric function implemented by Weber *et al.* requires ten spline knots in order to fit

the ellipsometry data and yet still fails to reproduce the graphene dielectric function accurately [117]. Sensitivity to the presumed thickness, or equivalently layer count, of a graphene film in reference to Weber *et al.* will be discussed further in section 6.3.5.

As a check of our own model dielectric function we can compare the next neighbor hopping energy t against angle resolved photoemission spectroscopy (ARPES) measurements for graphene grown by silicon sublimation from silicon carbide (SiC) at high temperature. Bostwick *et al.* fit the tight binding band structure of equation 6.1 against ARPES measurements and found $t = 2.82$ eV for $t' = 0$ in reference 166 and $t = 3.28$ eV for $t' = 0.0425$ eV in reference 167, values below and above the best-match model 2.907 eV respectively. As ellipsometry can only probe the difference between highest valence and select conduction bands, we neglect the overlap parameter t' in our model, which effectively increases the amplitude of the π or π^* band while decreasing the other proportionally and thus has little influence on the fitted value $|2t|$. It is possible to account for the discrepancy between values of t with uniform strain caused by different thermal expansion of graphene and the underlying SiC substrate [170] which can have large effects on t [171] and thus the optical conductivity [131]. Excellent agreement is achieved with Kravets *et al.*, who extracted a value of $t = 2.9$ eV from exfoliated graphene.

Absorption in the graphene layer calculated from best-match model parameters is presented in fig. 6.2. The best-match model from this work on CVD graphene compares favorably to that of CVD graphene from reference 118 and exfoliated graphene from references 148 and 149 up to ~4 eV. Above ~5 eV the bare harmonic oscillator model implemented by Nelson *et al.* cannot match the sharp asymmetry produced in the absorption spectrum as measured in this work and that of Mak *et al.* and Chae *et al.* Excellent agreement is achieved with the results of Mak *et al.*, even when the best-match model is extrapolated into the IR spectrum. The inset of fig. 6.2 shows

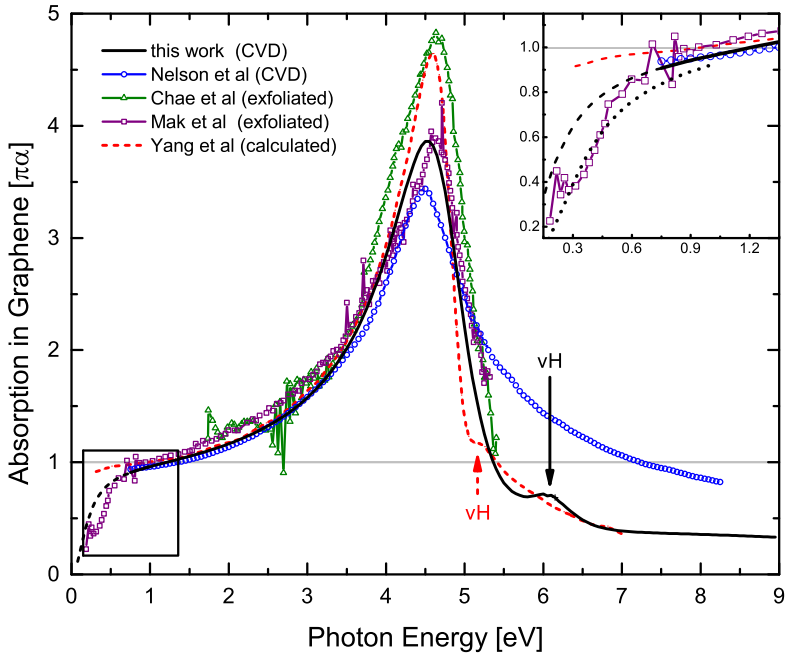

Figure 6.2: Absorption in graphene at normal incidence. Units have been normalized to $\pi\alpha$, as described by the constant conductivity model (grey line). Van Hove singularities are marked with the symbol 'vH'. The inset includes an extrapolation from the best-match model (black, dashed line) and a projection with no absorption below 0.2 eV (black, dotted line).

both the directly extrapolated model and an extrapolation with absorption blocking caused by a rise in the Fermi level. At low photon energies the Lorentz broadening (Γ) forces ε_2 to zero, resulting in a decrease in the absorption. If the Fermi level is raised, transitions are effectively blocked, and the drop off in absorbtion occurs at a higher energy, as seen in the inset of figure 6.2. Yang *et al.* predicted a similar line-shape using Bethe-Salpeter GW-DFT calculations, but predicted a lower energy for the $\pi - \pi^*$ critical point.

The analysis of CVD graphene spectra required additional free parameters from those produced in equation 6.10. The fused silica substrate was modeled with an isotropic Tauc-Lorentz dispersion typically used for amorphous materials [172], with

an amplitude of $A = 187(4)$ eV, peak energy of $E_0 = 10.45(5)$ eV, band gap energy of $E_g = 7.86(2)$ eV, and a broadening value of $C = 5.12(5)$ eV, with 90% confidence limits given in parenthesis. A band gap of 7.86 eV and a resonant energy of 10.45 eV are in good agreement with reported values for silica glass [173].

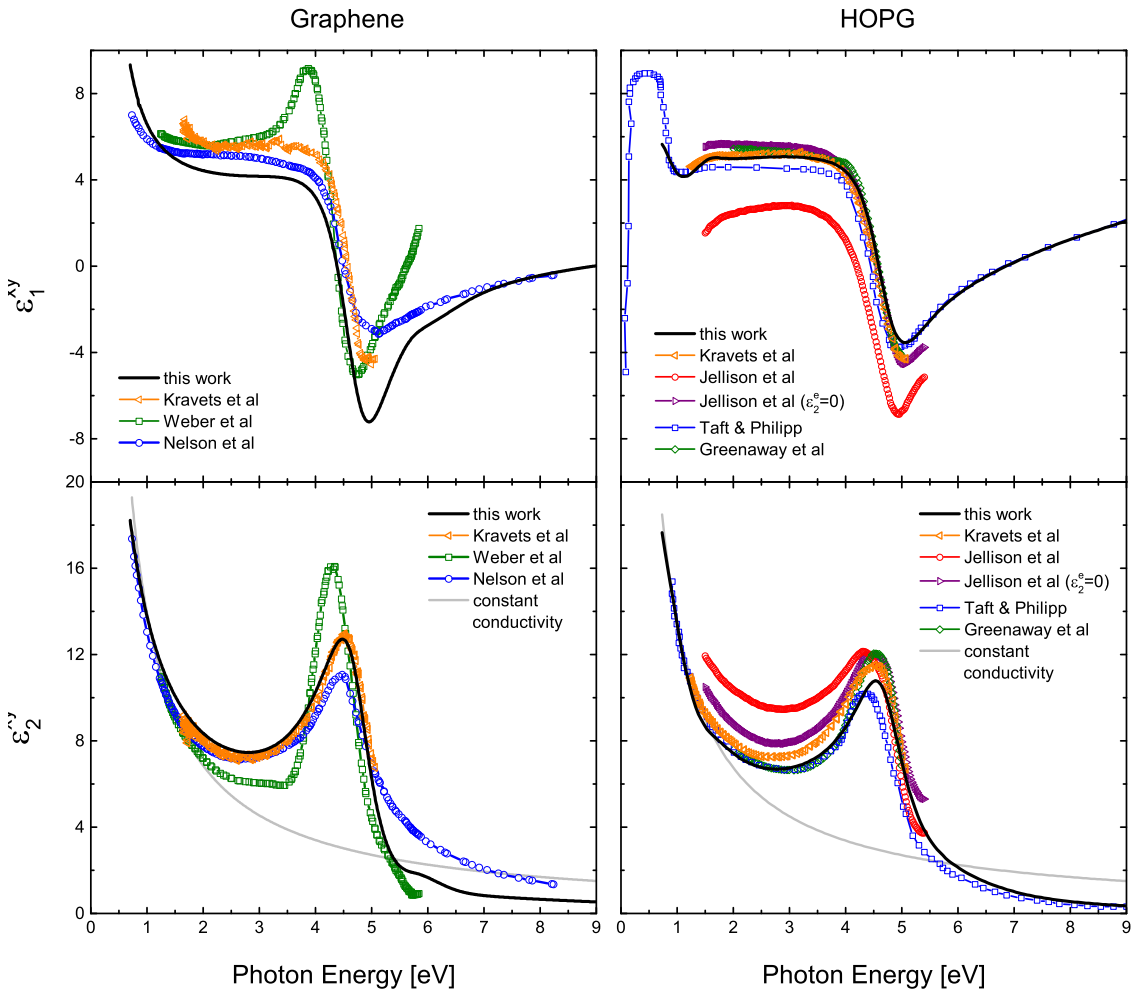

Figure 6.3: Dielectric functions for graphene and HOPG in plane (ordinary axes).

6.3.3 The HOPG Dielectric Function

The in-plane dispersion for HOPG presented in figure 6.3 is agreement with the majority of the literature, including excellent agreement with the only other experiment to measure in a similar spectrum [115]. As lower energies are reached, ε_1^{xy} should peak and then descend into the negative at zero eV. Much like figure 6.2, the peak shape in ε_1^{xy} is dictated by the overall broadening parameter Γ and the Drude free-charge carrier absorption in the infrared. In contrast the out-of-plane dispersion (ε^z) has been the subject of much debate due to the inability to polish the prism planes $\left\{10\bar{1}0\right\}$ for direct measurement [116, 136–140, 143, 145, 146]. As described in sec. 6.1, we implement a Cauchy model dispersion with best-match model parameters $A_n = 1.655(9)$, $B_n = 0.0023(4)$, and $C_n = 1.4(1) \times 10^{-4}$. This model places us in agreement with the results of references 137, 138, 140, 145 and 116, which assert that there is no absorption for light polarized along the z axis below 9 eV in HOPG. Most likely this is due to insufficient interaction between layers to allow optical transitions between π and σ bands at photon energies lower than 9 eV, as posited by Painter and Ellis. Our evidence for this is two-fold. First, if the results of Ahuja *et al.* are considered accurate we would expect to see two sharp absorption features at 0.8 eV and 1 eV, the first corresponding to the band separation between π and π^* at the **K** point and the second the onset of $\pi - \sigma$ absorption. It is clear from figure 6.1 that no such feature exists at 1 eV. Second, the out-of-plane dispersion must change the in-plane dispersion considerably for any particular HOPG ellipsometry experiment. In order to highlight this change we have analyzed the results of Jellison *et al.* in two distinct ways, both of which are shown for HOPG in figure 6.3. While Jellison *et al.* did not publish their data directly, the pseudo-dielectric-functions $\langle\varepsilon_1\rangle$ and $\langle\varepsilon_2\rangle$ in figure 1 of reference 136 are directly associated with the Ψ and Δ ellipsometry

experimental data, and can be inverted to find the data values. An analysis based on a biaxial model can then be performed, leading to new results. First we assume that the ε^z dispersion is given by a linear extrapolation of the two-modulator generalized ellipsometry microscope measurements found in reference 136. With the z axis fixed ε^{xy} is allowed to float for each photon energy during the fitting procedure. The resulting in-plane dielectric function is presented for HOPG in figure 6.3 in red circles. Alternatively, the same constraint can be made when the Cauchy model from section 6.1 is implemented as the ε^z dispersion (purple triangles). Two new observations can then be made from figure 6.3, that the visible spectrum measurement performed by Jellison *et al.* is in excellent agreement with the data presented in figure 6.1, ruling out experimental error as the difference between analyses, and that $\varepsilon_2^{xy}(E < 3\text{eV})$ is similar for graphene and HOPG only if $\varepsilon_2^z(E < 3\text{eV}) = 0$. This last consideration is quite important, as the constant conductivity model for absorption in the visible spectrum has been demonstrated for graphene stacked through five layers [107], for thin film HOPG [116], and for HOPG [151]. In order to maintain agreement with all experimental results and with the majority of analyses, the dielectric function of HOPG must be close to the constant conductivity model for graphene in the visible spectrum, causing $\varepsilon_2^z = 0$ to become a requirement for the model. Note that this does not invalidate the results of reference 174, as the slightly amorphous sample with numerous small domains would be expected to behave much differently than bulk HOPG.

Comparison of the best-match model HOPG results with those of Kravets *et al.* and Greenaway *et al.* in figure 6.3 show fair agreement, and surprisingly excellent agreement with the results of Taft and Philipp. Kravets *et al.* performed their analysis on a thin sample of HOPG (~1 µm), and their results are expected to lie between those of our bulk HOPG sample and graphene. The excellent agreement between

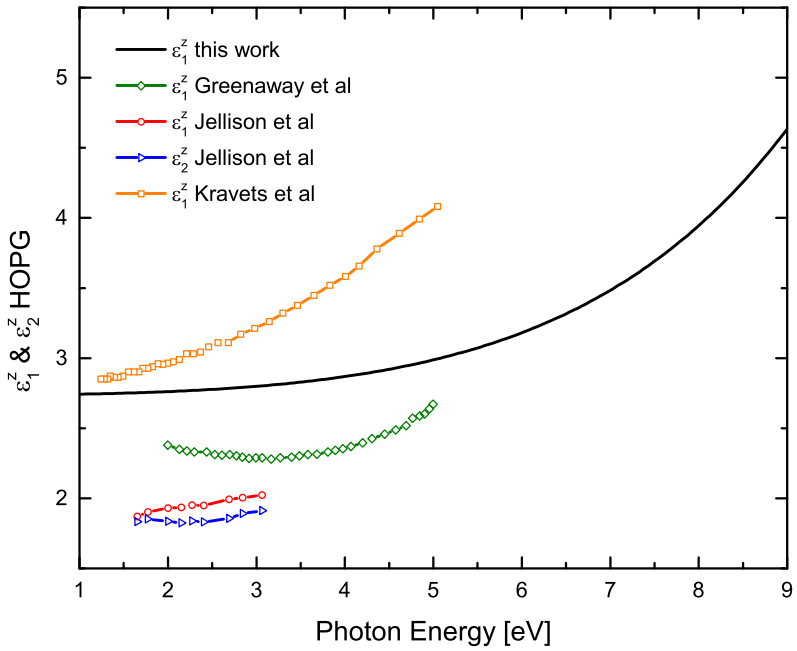

Figure 6.4: Model dielectric functions for HOPG in the z direction from multiple sources [116, 136, 137].

all references in the zero crossing of ε_1^{xy} at ~4.9 eV coupled with a large discrepancy in peak magnitude in ε_2^{xy} suggest that these experiments differ only in the purity of the sample surface, with a larger peak in ε_2 indicating a cleaner sample surface [136]. Results for off axis Greenaway *et al.* and Ergun found values of $n_e = 1.55$ and $n_e = 1.81$ [175] with $k_e = 0$ at $E = 2.28$ eV, in fair agreement with the value of $n_e = 1.66$ reported here. Drude absorption due to free charge carriers in HOPG had a best-match model resistivity of $\sim 6 \times 10^{-6}$ Ω-cm, a value which is an order of magnitude lower than expected from literature [176]. This discrepancy is probably caused by the band gap at the K-point between the π bands, which produces a sharp absorption at $E_g = 0.805$ eV and interferes with the Drude term. The exact nature of the absorption cannot be determined from this measurement which is limited in the IR to E>~0.75 eV. As discussed in sec. 6.1, a 1D band gap was chosen for this absorption,

as a 2D unit-step based critical point was not sharp enough to reproduce the feature between ~0.75 and ~1.5 eV in ε_1^o. As to the exact nature of the 1D absorption we cannot be certain, as it might be one of three possibilities. It is possible that the π^* band at the K-point is flat enough in the K-M and K-H directions compared to the K-Γ direction to form a natural 1D van-Hove singularity, as can be identified in reference 142. Alternatives possibilities include a stacking fault which can create 1D channels within the band structure [177], or a 2D critical point accompanied by a sharp exciton absorption as described by Pedersen *et al.* [178]

6.3.4 Effect of the Universal Broadening Parameter (Γ or σ)

As demonstrated in section 6.1, the broadening function can be implemented as either a simple harmonic oscillator (also known as Lorentzian broadening) or a Gaussian function. Note that unlike reference 157, the harmonic oscillator function in equation 6.6 includes a normalization factor of π. This is required for the integrated area of the imaginary part of the oscillator to equal one. From inspection of equation 6.4, it is evident that the limit of the imaginary dielectric function as either Γ or σ go to zero should be the exact joint density of states function. Furthermore, the Gaussian broadening solution naturally includes a normalization factor of $2\sqrt{\pi}\sigma$ which results in an area of one. Without the normalization the Lorentzian and Gaussian styles produce drastically different amplitudes for the dielectric function and cannot be directly compared.

HOPG and CVD graphene data were analyzed with both Lorentzian and Gaussian broadening styles. While HOPG showed no preference for a specific broadening style, graphene showed a clear preference for Lorentzian style broadening, with a ~20% increase in the mean squared error when using Gaussian broadening. In addition σ is

forced to a value of zero during the fitting procedure, resulting in a complete loss of the shoulder peak assigned to the π-π^* transition. Typically Lorentzian broadening has been associated with energy overlap with neighboring electrons while Gaussian broadening has been associated with thermal or Doppler broadening [179]. Thus σ was altered to increase with increasing photon energy indicative of a underlying Maxwell-Boltzmann thermal distribution, with no improvement. Gaussian broadening may also be caused by significant statistical variation in the local electron environment [16], in which case a preference for Lorentzian broadening is indicative of a highly uniform graphene sample. Further development of the model in section 6.1 to include a broadening function capable of seamlessly transitioning between Lorentzian and Gaussian oscillator styles may point towards an easily accessible metric for epitaxial graphene quality.

6.3.5 Film Thickness and the Amplitude Parameter (A)

In the analysis of Kravets *et al.* significant effort was spent developing a two dimensional optical model for graphene. While useful in the context of analyzing an individual graphene layer, it is not easily scalable to few-layered graphene or HOPG. Typical ellipsometry analysis requires a finite thickness for each layer of the optical model. One obstacle to this approach is the correlation between the amplitude parameter (A) established in section 6.1 and the thickness parameter (d). Normally the correlation between the thickness of a thin film and the magnitude of its dielectric function is broken by taking several angles of incidence, where the resulting difference in path length can cause a significant phase shift in the ellipsometric angles Ψ and Δ. For a mono-atomic film like graphene even vacuum ultraviolet wavelengths are too large to incur a significant phase shift, and the magnitude of the dielectric function

becomes highly correlated with the graphene thickness.

Instead this correlation must be broken by predetermining a value for the amplitude parameter. A reasonable starting point is the universal optical conductance model, which simply states that graphene has an optical conductance of $G = 6.08 \times 10^{-5}\ \Omega^{-1}$ [151]. The optical conductivity can then be determined with the assumption that the conductivity is spread uniformly through a unit cell with thickness $d = 3.35$ Å. Since the cross section normal to the current is always a function of the thickness, the conductivity will scale uniformly regardless of the length of the lattice parameter (typically $a = 1.42$ Å) so long as there is no uniaxial strain. The optical conductivity is directly related to the imaginary part of the dielectric function by the angular frequency, such that $\varepsilon_2 = \sigma/\omega$. For an angular frequency equivalent to a photon energy of 1 eV the value of $\varepsilon_2 = G/d\omega|_{E=1} = 13.500$. Assuming that the real part of the dielectric function is unchanged leads to the following simplistic model dielectric function for graphene:

$$\varepsilon(E) = 1 + \frac{13.5i}{E}\ . \tag{6.12}$$

Alone this result is useful for a narrow spectral region in which the photon engery is too large for any free charge carrier effects and too small to be affected by the exciton absorption peak. The constant optical conductance model is based on the linear band structure for graphene around the **K**-point, and by replacing the joint density of states given in equation 6.2 with linear version $J_{cv} = (2A_c|E|)/(\pi\nu_F^2)$ where A_c is the area of the unit cell and ν_F is the Fermi velocity [168], the model dielectric function presented in section 6.1 can be directly tested. Under idealized circumstances Lorentzian broadening is assumed and Γ approaches zero, leading to the following model dielectric function:

$$\begin{aligned}\varepsilon(E) &= \lim_{\Gamma\to 0}\left\{1 - A\int\left(\frac{2A_c|E'|}{\pi\nu_F^2}\right)\frac{1}{\pi E'^2}\left(\frac{1}{E-E'-i\Gamma}-\frac{1}{E+E'-i\Gamma}\right)\mathrm{d}E'\right\} \\ &= 1 + A\left(\frac{2A_c}{\pi\nu_F^2}\right)\frac{i}{E}\ .\end{aligned} \tag{6.13}$$

From inspection of equations 6.12 and 6.13 it is clear that $A(2A_c|E|)/(\pi\nu_F^2)$ must equal 13.5. Both the area of the unit cell ($A_c = 3\sqrt{3}a^2/2$) and the Fermi velocity ($\nu_F = 3ta/2$) are known and well documented values (see reference 168 for example), allowing the amplitude parameter to be estimated as $A = 330$. It is important to note that the relative dielectric function should always remain dimensionless, and by performing the previous substitutions for the area of the unit cell and the Fermi velocity the lattice parameter cancels and the next neighbor hopping energy t is given in eV. If one wishes to use the commonly quoted Fermi velocity $\nu_F = 10^6\ \mathrm{m\,s^{-1}}$, a conversion factor from eV to Joules must also be included. Recalculating equation 6.13 without the limit on broadening and with the estimation of A results in a dielectric function more useful than that found in equation 6.12, as the inclusion of broadening provides Kramers-Krönig consistency such that;

$$\begin{aligned}\varepsilon(E) &= 1 - A\int\left(\frac{2A_c|E'|}{\pi\nu_F^2}\right)\frac{1}{\pi E'^2}\left(\frac{1}{E-E'-i\Gamma}-\frac{1}{E+E'-i\Gamma}\right)\mathrm{d}E' \\ &= 1 + \frac{13.5i}{E-i\Gamma}\ ,\end{aligned} \tag{6.14}$$

where E is still given in photon energy. Though equation 6.14 does not include free charge carrier absorption it can easily be added with a Drude term in the style of equation 6.10, allowing equation 6.14 to be a powerful tool for analyzing graphene spectra below ~2 eV.

While equation 6.14 can indeed be useful for low photon energies, the more comprehensive model presented in section 6.1 is required for the visible and vacuum ultraviolet spectral ranges. The value for the amplitude parameter found previously ($A = 330$) could still be used but assumes a value for the Fermi velocity, and by extension also assumes a value for the next-neighbor hopping energy t. To avoid said assumption the amplitude parameter can be calculated directly from $A = 8(\hbar e P_{cv})^2/(m^{*2}A_c)$, but requires several alternative assumptions to be made. First it must be understood that the mathematical definition for A is pulled from references 180 and 157, which use Gaussian units for everything other than energy, which has been adapted to the eV scale here. Also while reference 157 defines m as simply the electron mass, inspection of the derivation in reference 180 and a similar derivation in chapter 6 of reference 114 clearly show the parameter m is based on the momentum operator acting within the material, and should therefore be the effective electron mass m^*. However, for graphene the effecive mass within the linear band region is said to be zero since the typical definition of the effective mass is $\mathrm{d}^2\epsilon/\mathrm{d}\epsilon^2$, where ϵ is the electron energy band. Alternatively it can be shown that a more appropriate definition of the effective mass is $m^* = \sqrt{\pi n}/\nu_F$, which is also the cyclotron effective mass, where n is the free charge carrier concentration [168, 181]. Reference 182 shows that the intrinsic carrier concentration can be calculated in terms of the Fermi velocity such that $\sqrt{n_i} = \sqrt{\pi/6}(kT/\hbar\nu_F)$, where k is the Boltzmann constant and T is the ambient temperature. Finally the leftover momentum matrix element P_{cv} must be estimated. It is assumed that the graphene sample is epitaxial, and with both CVD and Si sublimation techniques epitaxial graphene consists of many randomly oriented domains. Thus rather than attempt to compute the incoming polarization orientation with respect to a graphene crystal orientation, the probability is averaged over all angles such that:

$$\langle |P_{cv}|^2 \rangle = \frac{|\langle c|\hat{e}x|v\rangle|^2 + |\langle c|\hat{e}y|v\rangle|^2 + |\langle c|\hat{e}z|v\rangle|^2}{3} = \frac{2}{3} \, , \tag{6.15}$$

where it is assumed that transitions within the x-y plane of the graphene layer will absorb near perfectly and no absorption will occur normal to the graphene layer. The final result is that the amplitude parameter can be estimated entirely as a function of known constants and the next-neighbor hopping energy such that $A = 4.2735\ t^4$. For a value of $t = 2.907$ eV the amplitude parameter $A = 305$, as reported in table 6.1, and has fair agreement with the previously calculated value of 330. With the correlation between the thickness and amplitude parameter broken, the model dielectric function presented here can be used to determine the number of epitaxial graphene layers present as multiples of the HOPG interlayer distance.

6.3.6 Exciton Dimensionality

Excitons are modeled as either three dimensional, with energies $E_e = 2t - E_b/n^2$, or two dimensional, with energies $E_e = 2t - E_b/(n + \frac{1}{2})^2$, where E_b is the binding energy and $2t$ is the energy difference between the π and π^* bands at the M-point in the graphene band structure [160, 161]. The probability that an electron and hole are found in the same unit cell is similarly affected, with $|\Phi_0|^2 = 2V_0(\pi a n^3)^{-1}$ for 3D excitons and $|\Phi_0|^2 = 2V_0(\pi a[n+\frac{1}{2}]^3)^{-1}$ for 2D excitons. In the summation over all the exciton states n, the lowest value of n is one for 3D excitons and zero for 2D excitons. The result is that the entire perturbation is heavily dependent on the dimensionality of the exciton series, and thus should be determinable by the ellipsometry experiment. However, the 2D and 3D models were tested on both HOPG and CVD graphene, with no obvious preference seen in the lowest mean squared error. For graphene the

lowest mean squared error for the 2D and 3D models were within 5% of one another. When the mean squared error figure of merit is calculated with the Ψ and Δ spectra weighted by the experimental error, as presented in equation 2.39, the 3D exciton model has a lower mean squared error. Without the error weighting the 2D model performs better.

Ultimately a metric other than the mean squared error was required to determine the best model. The model presented in section 6.1 is the 2D model, as the majority of the best-match model parameters agreed with theoretical predictions, as shown in table 6.2. Note the excellent illustration of the relationship between the thickness and the magnitude of the dielectric constant discussed in section 6.3.5. Each parameter for the 3D model in table 6.2 is possible, or even probable for strained graphene with a shifted next-neighbor hopping energy [131, 170, 171, 183]. However, the exciton binding energy of almost two electron volts required for the 3D model to fit the CVD graphene data is difficult to explain when a much more reasonable solution is available.

Table 6.2: Best-match in-plane model parameters for graphene comparing the 2D and 3D excitonic models. Units for each parameter are shown in brackets.

Parameter		Ideal	2D exciton	3D exciton
d	[Å]	3.35[a]	3.34(4)	3.13(4)
$\varepsilon_2\|_{E=1}$	–	13.5[b]	13.8	18.1
t	[eV]	2.8 - 3.0[c]	2.907(9)	3.262(4)
E_b	[eV]	0.37 - 0.42[d]	0.423(4)	1.945(7)

[a] The established thickness estimate of a graphene monolayer.
[b] See section 6.3.5.
[c] See references 19, 166–168.
[d] See reference 148.

6.4 Conclusions

There have been many spectroscopy experiments performed on graphene and HOPG, with results similar to those presented here. However, none have accurately described the origin of both absorption features found in the visible and ultraviolet spectral regions with a compelling optical model until now. The tight-binding band structure based model dielectric function accurately describes the 2D van Hove singularity expected from $\pi - \pi^*$ transitions at the **M**-point in the graphene band structure with physically relevant parameterization. With the addition of an excitonic perturbation to the optical transition probability, the model dielectric function can also account for the asymmetric peak at ~4.6 eV, which has historically been confused with the $\pi - \pi^*$ transition. Lorentzian style broadening and two dimensionally confined excitons are preferred for the CVD grown eptiaxial graphene measured here. Determination of the preferred broadening style may be an indication of the quality of the measured graphene sample, with heavy Gaussian broadening indicating a non-uniform graphene layer. The model dielectric function, while physically correct for graphene, can be phenomenologically extended to HOPG when a 1D band gap at the **K**-point is added to one of the π bands. Absorption along the z-axis in HOPG has been long debated, but was found incompatible with the band structure compliant model dielectric function presented here.

Chapter 7

Characterization of Epitaxial Graphene on 3C-SiC

Epitaxial graphene grown by sublimation epitaxy on silicon carbide (SiC) holds great promise for large-scale production of next generation fast electronic devices [11, 14, 89, 184–187]. Despite significant progress and intense research efforts in the field, state-of-the-art epitaxial graphene shows electronic mobility parameters that are still orders of magnitude lower than those found in exfoliated graphene. Understanding the physical origin of the substantially different transport properties of epitaxial graphene and exfoliated graphene remains one of the major issues, and prevents further technological advances. The key point is to identify and control how the substrate affects epitaxial graphene uniformity, thickness, layer stacking and carrier mobility properties. Of particular interest is to monitor and control the thickness where epitaxial graphene can be composed of single layer graphene, few, or multiple layer graphene. While epitaxial graphene on the hexagonal polytypes of SiC has been extensively studied, knowledge about growth and properties of epitaxial graphene on cubic 3C-SiC substrates is not exhaustive. Few studies on graphene growth on the Si-face of 3C-SiC(111) on Si have been performed, and terrace growth of epitaxial graphene with domain sizes of a few micrometers and limited homogeneity was reported [13]. 3C-SiC offers a number of advantages over the piezoelectric poltytypes of SiC because of its isotropic and un-

polarized growth surfaces and the reported performance improvement of SiC-based electronic devices.

The growth mechanisms and kinetics as well as the electronic and transport properties of epitaxial graphene grown on the two (Si and C) polar faces of the hexagonal poltypes of SiC (0001) are significantly different [98, 188]. For example, on the Si-face of 4H-SiC and 6H-SiC a buffer layer is typically formed before the growth of graphene. The buffer layer, which is strongly bonded to the substrate, represents a $(6\sqrt{3} \times 6\sqrt{3})$R30° surface reconstruction. While this bonding was not addressed in the model development in chapter 6, it is assumed here that it can be accounted for within ellipsometry experiments by an effective medium approximation. In the case of epitaxial graphene grown on the C-face, the first layer is believed to be only weakly bonded to the substrate. Much larger domains with uniform epitaxial graphene thickness of single layer graphene and sizes of several hundreds of micrometers are obtained on the Si-face of 4H-SiC and 6H-SiC [11]. However, on the large scale necessary for industrial applications, epitaxial graphene on Si-face still shows certain nonuniformity. Epitaxial graphene on C-face shows smaller domains with sizes up to several tens of micrometers where the control of thickness down to single layer graphene or few layer graphene is difficult. The simultaneous mapping of these properties presents a significant challenge due to the varying domain structure of epitaxial graphene and the fact that characterization techniques with different spatial resolution are typically employed. In order to provide in-depth characterization of epitaxial graphene grown on 3C-SiC we employ here a large-scale mapping approach of structural and electronic properties. Our approach identifies functional correlations between structural, electronic and transport properties, and may be further used to reveal their interrelations with the influence of the substrate. Identifying these functional characteristics may ultimately enable device technologies.

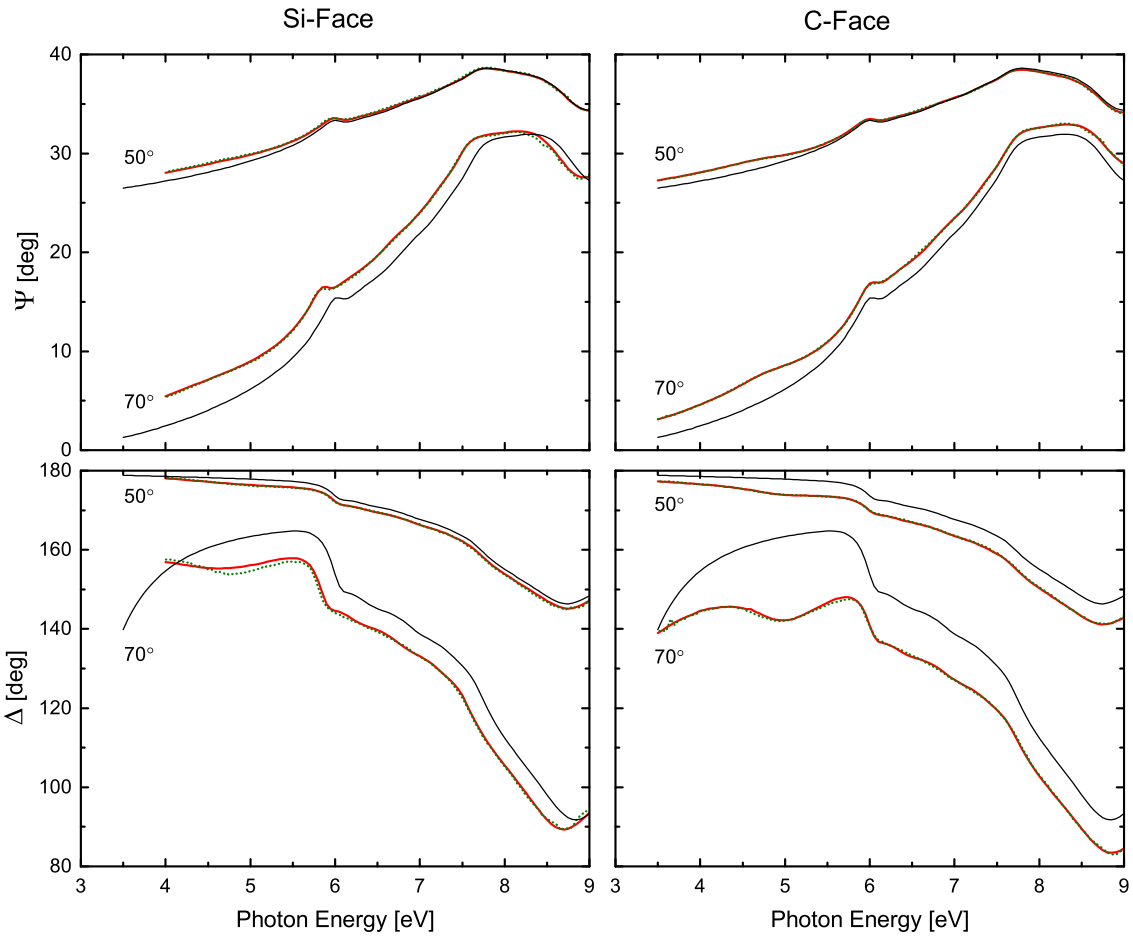

Figure 7.1: Experimental visible to ultra-violet ellipsometry data from the Si- and C-faces of 3C-SiC (green, dotted lines), along with best-match model results (red, solid lines). Bare 3C-SiC data is also presented (black, solid lines).

7.1 Experiments

Ellipsometry experiments provide a method to measure the optical constants, and through analysis of the dielectric function, also provide information on the electronic structure of the material. Spectroscopic ellipsometry in the near-infrared-visible-ultraviolet region was used to study epitaxial graphene obtained by different techniques [118, 147, 189–191], expfoliated graphene [116, 117], as well as for *in-situ* monitoring of graphene growth on metals [192]. Imaging ellipsometry was used to de-

termine thickness of small flakes of exfoliated graphene [7, 193, 194]. As discussed in chapter 5, the visible to vacuum ultra-violet dielectric functions of epitaxial graphene grown on different polytypes of SiC were found, and a parameterized dielectric function model for graphene was developed [147]. This model was further developed in chapter 6, and both models will be of use here. Despite the numerous publications focused on graphene, large-area mapping of epitaxial graphene thickness and electronic properties using micro-focal spectroscopic ellipsometry (μ-SE) has not been reported yet.

This chapter focuses on the disadvantages of optical graphene characterization with a large beam-spot size, and how these disadvantages can be mediated with novel large-area μ-SE mapping techniques. First, broad spectrum visible to vacuum ultra-violet ellipsometry measurements similar to those in chapter 6 are carried out on bare thick bulk-like 3C-SiC(111). Subsequent measurements after high-temperature silicon sublimation growth of epitaxial graphene are taken for both the Si- and C-face of 3C-SiC. A second set of ellipsometry measurements was conducted using μ-SE mapping in the near infrared to visible spectrum. Finally, complementary low-energy electron microscopy (LEEM) and micro-low-energy electron diffraction (μ-LEED) measurements were used to probe morphology, thickness and the surface structure of the epitaxial graphene in selected sample locations to confirm the conclusions draw from ellipsometry data.

Epitaxial graphene samples were grown by high temperature sublimation in Ar_2 atmosphere under optimized conditions on the Si- and C-face of 3C-SiC (111). The thick (few hundreds of micrometers) 3C-SiC layers were grown by sublimation epitaxy on 6H-SiC (0001) with our in-house-built reactor [120]. Standard spectroscopic ellipsometry measurements were carried out in the visible to ultra-violet spectral range at 50° and 70° angles of incidence, with the percentage of depolarization measured

simultaneously (as described in section 2.1.6), on a J.A. Woollam VUV-302 ellipsometer. The μ-SE mapping of circular areas with diameter of 0.5 cm for photon energies from 1.25 eV to 5.45 eV was performed with a J.A. Woollam M2000 multi-channel ellipsometer equipped with focusing optics allowing for measurement spot size of approximately 25×50 µm^2. LEEM and μ-LEED measurements were performed on selected locations on the samples with resolution of 10 nm. The number of layers can be extracted from the number of minima in the electron reflectivity spectra extracted from energy series of LEEM images [195]. The LEEM image contrast taken at a given electron energy reveals information on the number of layers and domain structure. The field of view used for LEEM (50 µm) matches approximately with the μ-SE spot size and results obtained by LEEM and μ-SE allow for comparative conclusions.

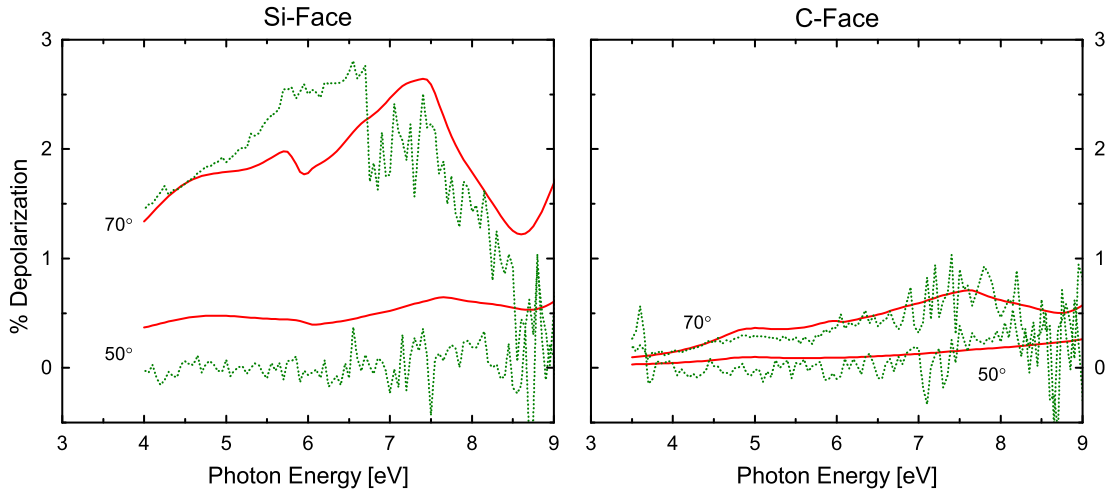

Figure 7.2: Depolarization spectra for graphene grown on the Si- and C-face of 3C-SiC (green, dotted lines) along with a best-match model generated by patterning (red, solid lines).

7.2 Model Dielectric Functions & Optical Models

A stratified layer optical model composed of substrate, interface layer between the substrate and graphene, and graphene layer is used here. The interface layer accounts for a buffer layer (if present), roughness of the substrate surface (an effect of the slight off-axis cut of the SiC substrate), and non-uniform sublimation of silicon from the SiC substrate. The model dielectric function of the 3C-SiC substrate, as determined in chapter 5 and published in reference 147, was implemented with no further changes. Both ellipsometry experiments were analyzed with this optical model, with the exception of layer patterning. For the visible to ultra-violet data, patterning was included for the interface layer on the silicon face, and the graphene layer for the carbon face. Patterning is implemented by generating data with and without the layer, then mixing the resulting Mueller matrices. A patterning percentage of 0% implies that the layer is a complete thin film, while a percentage of 100% implies that the layer is entirely missing from the optical model. This type of analysis is highly suited to the concept of depolarization described in section 2.1.6.

The visible to ultra-violet ellipsometry experiment was analyzed with the graphene model dielectric function introduced in chapter 6, while the μ-SE mapping experiment was analyzed with the oscillator model used in chapter 5. This was done for a variety of reasons. First, the highest photon energy reached by the M2000 ellipsometer is 5.45 eV, not high enough to contain the shoulder peak attributed to the van Hove singularity. This renders the band structure based model useless, as the typically varied parameters would have to be fixed or would correlate. Second, the band structure based model takes several seconds to produce a single spectrum rendering it unrealistic for analysis of several hundred individual μ-SE experiments. Finally, by analyzing the same samples with both model dielectric functions it is possible to

compare the effectiveness of each. In addition to the dual oscillator functions, the μ-SE model dielectric function contains a free-charge carrier contribution in the form of the classical Drude function

$$\varepsilon_{FC} = \varepsilon_{\infty} - \frac{i4\pi\hbar^2}{\rho(\hbar\lambda + i\lambda^2\tau)}, \tag{7.1}$$

where ρ, λ, and τ are the resistivity, the wavelength and the free-charge carrier scattering time. The free-charge carrier scattering time is related to the optical mobility parameter by $\tau = m^*\mu/q$, where m^*, μ and q are the free-charge carrier effective mass, mobility and charge. By reducing the free-charge parameters to ρ and τ complications arising from the effective mass can be ignored.

The interface layer model dielectric function was treated as an effective mixing of the 3C-SiC and graphene dielectric response, using the Bruggeman effective medium approximation (EMA). When analyzing the μ-SE data the thickness of the interface layer was fixed at 3.5 Å(the inter-layer distance in HOPG) without further variation during the analysis, but its constituents percentage was allowed to vary between 0% and 100%. An EMA with a SiC constituent percentage of 100% implies a smooth interface between the substrate and the garphene. In contrast, an intermediate EMA of 50% graphene and 50% SiC would indicate an interface layer that is randomly rough. The parameters of the graphene model dielectric function (Lorentzian and Gaussian oscillator amplitudes, energies and broadenings, free-charge-carrier scattering time and resistivity), the graphene layer thickness, and the interface-layer SiC percentage were varied until the experimental and calculated data matched. Excellent agreement between experimental and best-match calculated Ψ and Δ spectra is achieved in all points of the maps with a typical mean squared error below 0.1. For the visible to ultra-violet experiment performed on the carbon face of 3C-SiC, the EMA percentage

was fixed at 50%. This is a common practice for thin layers in which the thickness and EMA constituent percentages tend to correlate because the difference between index and thickness cannot be resolved [61, 109].

7.3 Results and Discussion

Initial visible to ultraviolet experiments on 3C-SiC resisted analysis with either the general oscillator model developed in chapter 5 or the band structure based model developed in chapter 6. Neither model could accurately fit the Ψ and Δ spectra shown in figure 7.1, regardless of what parameters were entered into the effective medium approximation layer. Looking at figure 7.2, it becomes obvious that non-idealities were causing the established models significant problems. Since the same VUV-302 ellipsometer was used successfully in chapter 6, depolarization caused by the system was assumed to be low. An acceptable fit to the visible to ultra-violet spectra was established when layer patterning was used to model the depolarization data taken alongside the Ψ and Δ spectra. Patterning was applied to the interface layer on the Si-face and to the multi-layer graphene grown on the C-face, as it was assumed that non-idealities within the sample structure would be present as substrate flaws on the Si-face and as extraneous graphene grown on the C-face. This optical model was successful in describing both the Ψ and Δ spectra and the depolarization spectra. The mean squared error for fitting both the Si- and C-face ellipsometry spectra was excellent, with a value of 0.561. Silicon and carbon face experiments went through the fitting procedure simultaneously in order to account for any surface roughness of the 3C-SiC before graphene growth. Best-match model parameters are given in table 7.1. Parameters varied during the analysis are identical to those used in chapter 6, namely the amplitude parameter A, the next-neighbor hopping energy t, the exciton affinity

q, the exciton binding energy E_b, the Fano based exciton broadening parameters A_f and B_f, the overall broadening parameter Γ, and the high energy pole amplitude A_p. Exceptions are the graphene and interface layer thicknesses (d_G and d_I) and patterning percentages (P_G and P_I), and the percentage of graphene within the effective medium approximation of the interface layer ($\%_G$). Best-match model parameters suggest that graphene growth on the Si-face produces a mono-layer normally, but in some places produces an extremely rough and thick epitaxial layer. This is inferred from the patterning of the interface layer, which is 85 Åthick but only present across only 7% of the measured surface area. Interestingly the surface roughness of the substrate was found to be only about ~1 Åthick, so the almost 9 nm interface layer is a result of the graphene growth process. In contrast the C-face requires only a 4.9 Åinterface layer to accurately model the ellipsometry spectra, but requires a thick 18.9 Ågraphene layer. The nine mono-layer graphene is present across about ~70 percent of the measured surface, with the remaining surface area possessing no graphene layer.

Figure 7.3 shows the best-match model imaginary dielectric functions for graphene grown on the Si- and C-faces of 3C-SiC, as compared to the best-match models for CVD graphene and HOPG from chapter 6. On the Si-face the graphene possesses both the exciton peak and the higher energy shoulder peak attributed to the van Hove singularity, showing an overall structure very similar to the CVD graphene in chapter 6. The difference is the massively increased broadening parameter Γ, which at a value of 0.78 is almost four times larger than required for CVD graphene. This large broadening suggests that the 3C-SiC Si-face graphene contains many individual domains, each with slightly different band structure properties. Graphene grown on the C-face shows a markedly different imaginary dielectric function. Like HOPG no shoulder peak is evident graphically, but unlike HOPG the 4.5 eV peak only reaches

Table 7.1: Best-match in-plane model parameters for epitaxial graphene on the Si and C faces of 3C-SiC. The error limits given in parenthesis denote the uncertainty of the last significant digit (90% reliability). Values with no parenthesis are fixed. Units for each parameter are shown in brackets.

Parameter		Si-Face	C-Face
d_G	[Å]	2.5(6)	18.9(5)
A	[eV]	370(19)	134.4(5)
t	[eV]	3.05(4)	2.368(2)
q	–	−3.3(2)	−0.83(2)
E_b	[eV]	0.47(2)	0.24(4)
A_f	[eV]	0.94(4)	3.4(6)
B_f	[eV]	42(1)	42(1)
Γ	[eV]	0.78(2)	0.22(2)
A_p	–	2.20(9)	1.59(3)
P_G	[%]	0	28(1)
d_I	[Å]	85(13)	4.9(3)
P_I	[%]	93(2)	0
$\%_G$	[%]	95(2)	50

a value of about four. Part of the difficulty in determine the graphene and HOPG optical properties is that the asymmetric exciton peak at 4.5 eV occurs at the same energy as the band gap of amorphous carbon [196]. In fact the peak in the imaginary dielectric function of amorphous carbon is about four, matching the dielectric function in figure 7.3 quite closely. The conclusion that the epitaxial growth on the C-face is closer to amorphous carbon than graphene is reinforced by the best-match model parameters in table 7.1, which are quite different than both the Si-face and graphene grown by CVD.

Figure 7.4 shows best-match model calculated maps of graphene layer thickness, interface-layer SiC percentage, and free charge carrier scattering time parameters obtained from μ-SE data. The thickness maps in figure 7.4(a) reveal large homogeneous areas $\sim 2 \times 2$ mm^2 with mono-layer graphene on the Si-face. In addition, few islands of

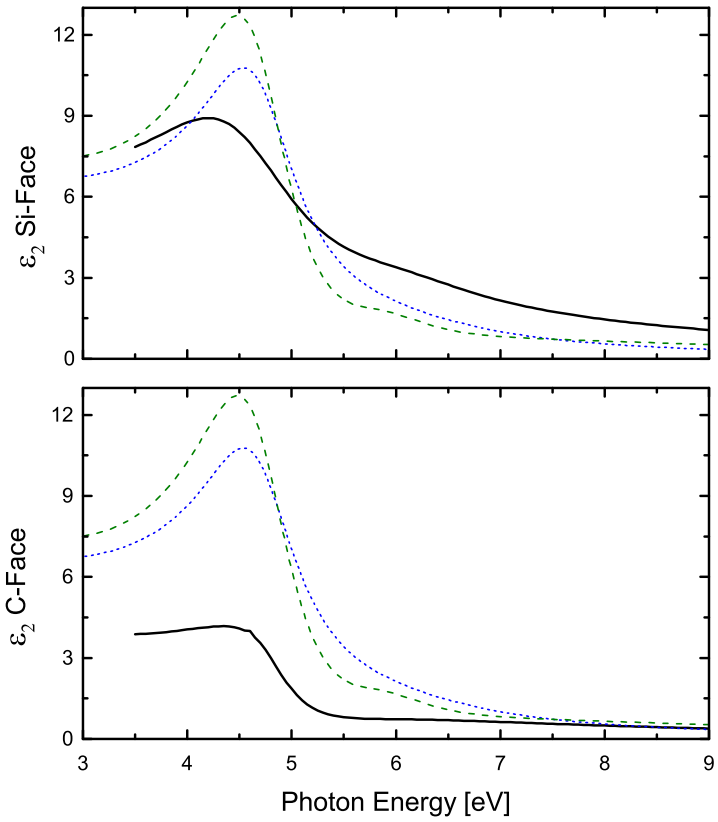

Figure 7.3: The imaginary part of the dielectric function for graphene grown on the Si- and C-face of 3C-SiC, as generated by the best-match model (black, solid lines). Comparison to ε_2 of graphene grown by chemical vapor deposition and HOPG from chapter 6 are also shown (green, dashed lines and blue, dotted lines respectively).

multi-layer graphene of several hundred micrometer size occur where the carbon has accumulated on the surface of the substrate. Both of these results match the analysis of the visible to ultra-violet ellipsometry experiment. Figure 7.4(b) depicts a uniform and large interface-layer SiC percentage within the same regions where mono-layer graphene was found on Si-face, which is indicative of a very smooth substrate surface. However, beneath the thick islands the interface layer was found to consist of approximately ~50% SiC indicative of significant surface roughness. In principle, this can be related to defects in the substrate surface. It is well known that defects in the

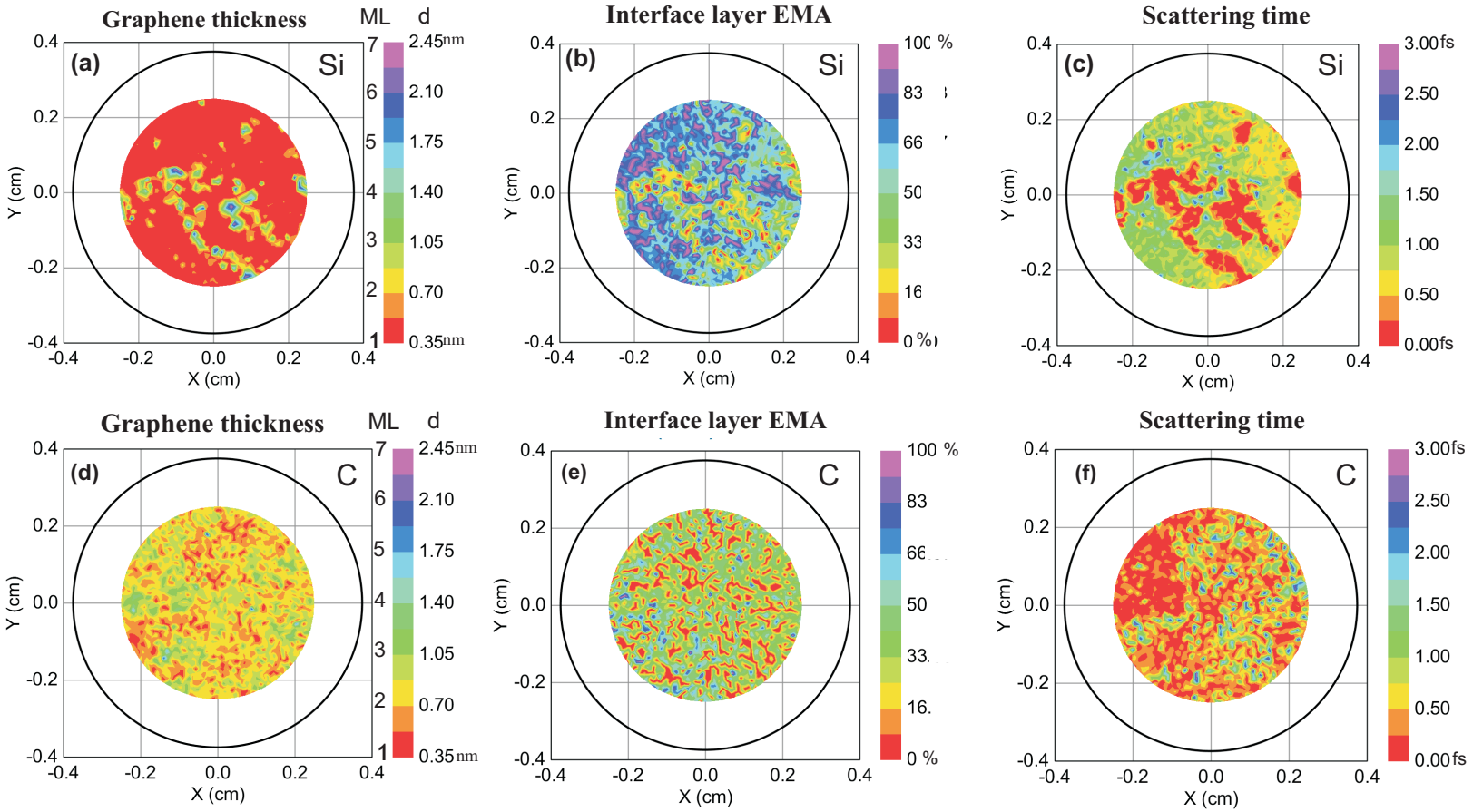

Figure 7.4: μ-SE maps of best-match model parameters for graphene layer thickness (a,d), interface-layer SiC percentage (b,e) and free-charge-carrier scattering time (c,f) for epitaxial graphene grown on Si-face and C-face of 3C-SiC.

SiC substrate serve as preferential centers for enhanced Si sublimation [197]. Thus, a higher growth rate of graphene could be expected around these defects, which may explain the formation of such graphite-like islands.

The areas with homogeneous graphene layer thickness in figure 7.4(d) for C-face 3C-SiC are much smaller than on the Si-face, where the thickness varies mostly between 1 to 3 monolayer graphene, and the formation of large multi-layer graphene islands is not detected. It has been shown that the growth of mono-layer graphene on the C-face of the hexagonal SiC polytypes is very challenging due to the much higher sublimation rate of silicon and usually growth of multi-layer graphene is reported for these surfaces. Although mono-layer graphene growth on the C-face is achieved here, the domain size depicted in figure 7.4(d) remains rather small. Figure 7.4(e) depicts an interface layer SiC percentage indicative of high substrate surface roughness and small uncorrelated islands of large graphene content. These results for 3C-SiC indicate that the interface structure of epitaxial graphene on C-face differs distinctively from Si-face.

Figure 7.5(a) shows an exemplary LEEM image for a region of the Si-face sample where a graphene thickness of approximately mono-layer graphene was found from the μ-SE maps. Large areas with a bright contrast occur, which can be associated with mono-layer graphene, and a few small regions occur with a darker contrast and which can be related to two mono-layers of graphene. The LEEM image confirms the highly homogeneous growth of mono-layer graphene in excellent agreement with the μ-SE result. Figure 7.5(c) shows LEED pattern taken from a mono-layer graphene region, and reveals the 1×1 diffraction spots associated with mono-layer graphene surrounded by the $6\sqrt{3} \times 6\sqrt{3}$-R30° diffraction spots associated with the SiC surface. These results suggest that a buffer layer similar to the one found on Si-face 4H-SiC and 6H-SiC is formed on the smooth surface areas of the Si-face 3C-SiC.

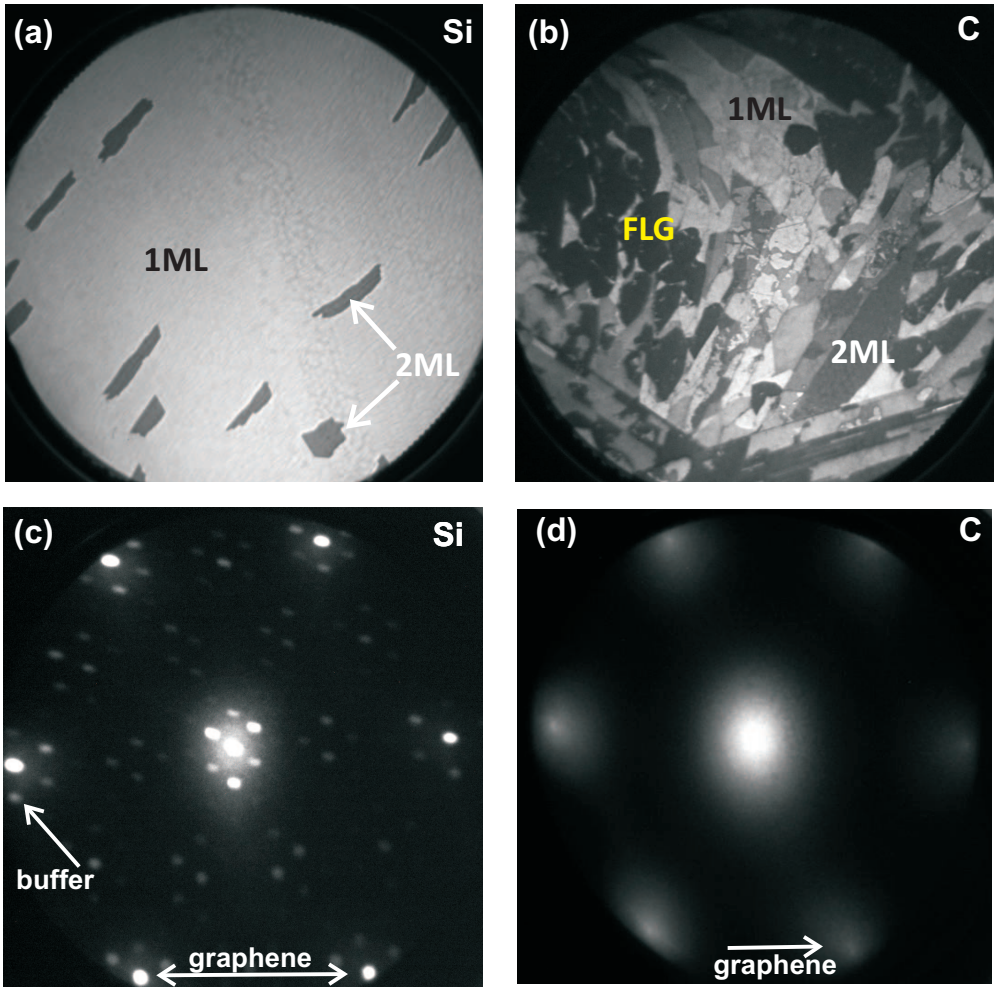

Figure 7.5: LEEM images from selected sample areas for epitaxial graphene on Si-face (a) and C-face 3C-SiC (b) (field of view 50 μm). Domains with 1, 2 and few monolayer (FML: 3 and 4 monolayers) graphene are indicated on the LEEM images. μ-LEED pattern from a 1LG (ML) area of the Si-face (c) and C-face (d) taken at 40 and 44 eV, respectively

.

Figure 7.5(c) shows an exemplary LEEM image for a region of the C-face sample. The image shows domains of one to four mono-layers of graphene with dimensions below the resolution for the μ-SE mapping. The much smaller domains of homogeneous graphene layers observed by LEEM [figure 7.4 (d)] may be related to the high substrate surface roughness found for C-face in figure 7.4(e). Figure 7.4(d) presents a LEED pattern taken from a mono-layer graphene region on the C-face sample. Only diffraction spots due to graphene occur, and no superstructure related to a specific SiC surface reconstruction is detected. This indicates a very different interface structure compared to the Si-face epitaxial graphene. Recent studies indicate that the predominant type of defects on the C-face of 3C-SiC is different from the twin boundaries found in Si-face 3C-SiC. On the C-face small inclusions occur, each associated with 6H-SiC formed around a screw dislocation [198]. The distribution of these 6H-SiC polytype defects is reminiscent of that of the small islands of high graphene coverage revealed in the interface layer map in figure 7.4(e).

Figures 7.4(a), (c), (d), and (f) reveal a significant correlation between the graphene layer thickness and the free charge carrier scattering time. While areas of predominantly mono-layer graphene reflect long scattering times, shorter scattering times correspond to the thick graphite-like islands. The reduction of scattering time indicates lower mobility across these areas and may be due to scattering across grain boundaries and (or) scattering between the different graphene sheets.

7.4 Conclusions

In summary, visible to ultra-violet ellipsometry, large-area μ-SE mapping, and LEEM/μ-LEED investigations revealed critical correlations between surface reconstruction, graphene layer thickness, and electronic properties of epitaxial graphene grown on Si-face

and C-face 3C-SiC. While complete characterization can be achieved using only the ellipsometry measurements, the conclusions are validated here by the LEEM and μ-LEED results. The visible to ultra-violet ellipsometry results are essentially an average over several growth regimes, limiting the effectiveness of the band structure based model developed in chapter 6. This shortcoming is alleviated by subsequent measurement with the μ-SE mapping technique.

Growth of single mono-layer graphene is demonstrated on both the Si- and C-face where large homogeneous domains with size up to $\sim 2 \times 2$ mm^2 are achieved on the Si-face. On the C-face the domains with homogeneous thickness are considerable smaller. The interface layer in this case also shows a distinctively different picture, with small uncorrelated nucleation sites that have high graphene coverage within the interface layer. These sites may be associated with small pit defects on the C-face substrate that represent 6H-SiC spiral growth inclusions. Furthermore, the maps of the free carrier scattering time show that the carrier mobility in the homogeneous areas of mono-layer epitaxial graphene is higher than the mobility in the thicker graphite islands. The analysis suggests that the interaction between epitaxial graphene and the substrate is stronger for the Si-face material. These results are consistent with our LEED observations indicating the formation of a $6\sqrt{3} \times 6\sqrt{3}$-R30 buffer layer on the Si-face and absence of any specific reconstruction on the C-face samples.

Chapter 8

Summary and Outlook

Spectroscopic ellipsometry was introduced as a valuable tool to characterize thin films, and has been shown throughout this work to be a valuable tool for characterizing graphene, silicon carbide, silicon, and highly ordered pyrolytic grapite specifically. Terahertz to near-infrared spectroscopic ellipsometry is equally effective at determining the electrical properties of micron scale doped layers of silicon in chapter 3 as it is those of atomically thin graphene, which was demonstrated in chapters 4, 6, and 7. Magneto-optic generalized ellipsometry is capable of determining not only the free charge carrier density and mobility, but also the effective mass within epitaxial graphene layers. From chapter 6 it is apparent that this ability is not only useful for determining the speed at which a potential graphene transistor might operate, but is also required for determining the optical properties in the visible to ultra-violet spectral ranges, as it directly impacts the value of the amplitude of the imaginary dielectric response. Unlike four-point probe, spreading resistance, or traditional Hall effect measurements, ellipsometry requires no contact with the sample, allowing it to be used directly in industrial production facilities as a quality metric.

Standard ellipsometry measurement tools are already found in almost every laboratory and thin film industrial production line, begging the question, why would

silicon carbide and graphene be neglected by these techniques? The answer is that while ellipsometry is a powerful measurement technique, much of the sensitivity to useful parameters is established by creating physically accurate optical models and model dielectric functions. In both chapters 3 and 6 sensitivity to useful parameters, like the thickness of individual layers, is established by constraining the model dielectric function with the physical consequences of the varied parameters. In chapter 3 the free charge carrier density on either side of an iso-type homojunction is directly related to the size of the diffusion region by the Poisson equation, such that the consequences of a charge carrier density change are immediately understood by the computer during the fitting procedure. Similarly, any change in the next neighbor hopping energy t of an epitaxial graphene layer changes the energy of the exciton series and the effective mass associated with it. Ultimately any set of best-match model parameters generated by these models is guaranteed to be physically self-consistent. This limits the size of the parameter space, allowing enough flexibility to fit even non-ideal samples like those in chapter 7 with enough rigidity to keep parameter correlation to a minimum.

Even with tailored model dielectric functions, ellipsometric characterization is at its best when multiple measurements can be combined into one analysis. Ideally a single measurement system would be capable of performing broad spectrum generalized ellipsometry measurements with a beam focused to any desired size at any location on the sample. Realistically several instruments are needed to achieve this level of functionality and choosing an appropriate model to suit the advantages and disadvantages of each instrument is required. The results of chapter 7 are an excellent example, as the visible to ultra-violet results are confusing without the micro-focal ellipsometry results included. By combining these two techniques it was possible to characterize the growth of epitaxial graphene on the Si-face of 3C-SiC, which shows

large areas of mono-layer growth next to smaller graphite-islands. Establishing consistent characterization techniques is the first step towards alleviating problems in the epitaxial graphene growth process.

Perhaps the most important discovery made in this work is in the identification and accurate modeling of the graphene and HOPG dielectric function, including which features are attributed to which causes. For HOPG in particular, band structure calculations had been at odds with the optical absorption results since the 1930's. It is now clear from both CVD epitaxial graphene and HOPG ellipsometry experiments that the feature at 4.5 eV is due to absorption from a series of excitons located at the M-point in the graphene band structure, energetically below the saddle. The high-energy shoulder to this peak is the actual two dimensional saddle point between the π and π^* bands. For low energy optical measurements, this arrangement can be modeled using the joint density of states produced by the π bands with a perturbation to the probability of an optical transition due to the presence of excitons.

As successful as some of the analysis is at describing real samples, the work presented here is not entirely complete. In the case of aniso-type homojunctions presented in chapter 3, a simple depletion region is used as the model. While this is accurate enough to match the ellipsometry experiments performed, a complete model would include diffusion into the depletion region, which can clearly be seen in the complementary spreading resistance profile. Chapters 5 and 7 require the lower half of the visible to ultra-violet ellipsometry measurement to be discarded due to an inability to model the silicon carbide substrate as it becomes transparent. Some progress has been made on this problem, but no model is currently able to account for the changes in polarization induced by the anisotropic semi-transparent material upon backside reflection. Chapter 6 spends a great deal of effort modeling the in-plane dielectric response of graphene. However, it mostly neglects the out-of-plane response. For

this reason it is impossible to tell just how much the underlying substrate affects the dielectric response of graphene. In order to solve this problem significant challenges in both the measurement and modeling of two dimensional materials will need to be overcome.

References

[1] K. S. Novoselov, A. K. Geim, S. V. Morozov, D. Jiang, M. I. Katsnelson, I. V. Grigorieva, S. V. Dubonos, and A. A. Firsov, Nature **438**, 197 (2005).

[2] J. D. Caldwell, T. J. Anderson, J. C. Culbertson, G. G. Jernigan, K. D. Hobart, F. J. Kub, M. J. Tadjer, J. L. Tedesco, J. K. Hite, M. A. Mastro, R. L. Myers-Ward, C. R. Eddy, P. M. Campbell, and D. K. Gaskill, ACS Nano **4**, 1108 (2010), pMID: 20099904.

[3] X. Liang, B. A. Sperling, I. Calizo, G. Cheng, C. A. Hacker, Q. Zhang, Y. Obeng, K. Yan, H. Peng, Q. Li, X. Zhu, H. Yuan, A. R. Hight Walker, Z. Liu, L.-m. Peng, and C. A. Richter, ACS Nano **5**, 9144 (2011).

[4] Y. Zhang, Y. Tan, H. L. Stormer, and P. Kim, Nature **438**, 201 (2005).

[5] K. Novoselov, Z. Jiang, Y. Zhang, S. Morozov, H. Stormer, U. Zeitler, J. Maan, G. Beobinger, P. Kim, and A. Geim, Science (2007).

[6] F. Molitor, J. Guttinger, C. Stampfer, D. Graf, T. Ihn, and K. Ensslin, Phys Rev B (2007).

[7] O. Albrektsen, R. L. Eriksen, S. M. Novikov, D. Schall, M. Karl, S. I. Bozhevolnyi, and A. C. Simonsen, Journal of Applied Physics **111**, 064305 (2012).

[8] B. N. Szafranek, G. Fiori, D. Schall, D. Neumaier, and H. Kurz, Nano Letters **12**, 1324 (2012).

[9] E. Rollings, G.-H. Gweon, S. Zhou, B. Mun, J. McChesney, B. Hussain, A. Fedorov, P. First, W. de Heer, and A. Lanzara, J. Phys. Chem. Solids **67**, 2172 (2006), sMEC 2005, Study of matter under extreme conditions.

[10] J. Hass, W. A. de Heer, and E. H. Conrad, J. Phys.: Condens. Matter **20**, 323202 (2008).

[11] C. Virojanadara, M. Syvaejarvi, R. Yakimova, L. I. Johansson, A. A. Zakharov, and T. Balasubramanian, Phys. Rev. B **78** (2008).

[12] D. K. Gaskill, G. G. Jernigan, P. M. Campbell, J. L. Tedesco, J. C. Culbertson, B. L. VanMil, R. L. Myers-Ward, C. R. Eddy, J. J. Moon, D. Curtis, M. Hu, D. Wong, *et al.*, ECS TRANS. **19**, 117 (2009).

[13] A. Ouerghi, A. Kahouli, D. Lucot, M. Portail, L. Travers, J. Gierak, J. Penuelas, P. Jegou, A. Shukla, T. Chassagne, and M. Zielinski, Applied Physics Letters **96**, 191910 (2010).

[14] W. A. de Heer, C. Berger, M. Ruan, M. Sprinkle, X. Li, Y. Hu, B. Zhang, J. Hankinson, and E. Conrad, Proceedings of the National Academy of Sciences **108**, 16900 (2011).

[15] R. M. A. Azzam, in *Handbook of Optics* (McGraw-Hill, New York, 1995), vol. 2chap. 272nd, ed.

[16] H. Thompkins and E. A. Irene, eds., *Handbook of Ellipsometry*, (William Andrew Publishing, Highland Mills, 2004).

[17] H. Fujiwara, *Spectroscopic Ellipsometry*, (John Wiley & Sons, New York, 2007).

[18] M. Schubert, *Infrared Ellipsometry on semiconductor layer structures: Phonons, plasmons and polaritons*, vol. 209 of *Springer Tracts in Modern Physics*, (Springer, Berlin, 2004).

[19] T. Stauber, N. M. R. Peres, and A. K. Geim, Phys. Rev. B **78**, 085432 (2008).

[20] E. Hecht, *Optics*, (Addison-Wesley, Reading MA, 1987).

[21] D. W. Berreman, J. Opt. Soc. Am. **62**, 502 (1972).

[22] M. Schubert, Phys. Rev. B **53**, 4265 (1996).

[23] R. M. Azzam and N. M. Bashara, *Ellipsometry and Polarized Light*, (North-Holland Publ. Co., Amsterdam, 1984).

[24] M. Schubert, in *Handbook of Ellipsometry*, edited by E. Irene and H. Tompkins (William Andrew Publishing, 2004).

[25] R. C. Jones, J. Opt. Soc. Am. **31**, 488 (1941).

[26] A. Gerrard and J. Burch, *Introduction to Matrix Methods in Optics*, Dover Books on Physics (Dover, 1994).

[27] D. Goldstein and D. Goldstein, *Polarized Light, Revised and Expanded*, Optical Engineering - Marcel Dekker (Taylor & Francis, 2011).

[28] A. Röseler, *Infrared Spectroscopic Ellipsometry*, (Akademie-Verlag, Berlin, 1990).

[29] E. S. Fry and G. W. Kattawar, Appl. Opt. **20**, 2811 (1981).

[30] W. S. Weiglhofer and A. Lakhtakia, *Introduction to Complex Mediums for Optics and Electromagnetics*, (SPIE, Bellingham, 2003).

[31] E. Hall, American Journal of Mathematics **2**, 287 (1879).

[32] P. Drude, Physikal. Zeitschr. **1**, 161 (1900).

[33] T. Hofmann, M. Schubert, and C. M. Herzinger, Proc. SPIE **4779**, 90 (2002).

[34] T. Hofmann, M. Grundmann, C. M. Herzinger, M. Schubert, and W. Grill, MRS Proceedings **744**, M5.32 (2002).

[35] T. Hofmann, M. Schubert, C. M. Herzinger, and I. Pietzonka, Appl. Phys. Lett. **82**, 3463 (2003).

[36] M. Schubert, T. Hofmann, and C. M. Herzinger, J. Opt. Soc. Am. A **20**, 347 (2003).

[37] M. Schubert, T. Hofmann, and C. M. Herzinger, Thin Solid Films **455-456**, 563 (2004).

[38] S. Schöche, T. Hofmann, V. Darakchieva, N. B. Sedrine, X. Wang, A. Yoshikawa, and M. Schubert, J. Appl. Phys. **113**, 013502 (2013).

[39] T. Hofmann, T. Chavdarov, V. Darakchieva, H. Lu, W. J. Schaff, and M. Schubert, Phys. Stat. Sol. (c) **3**, 1854 (2006).

[40] T. Hofmann, U. Schade, K. C. Agarwal, B. Daniel, C. Klingshirn, M. Hetterich, C. M. Herzinger, and M. Schubert, Appl. Phys. Lett. **88**, 42105 (2006).

[41] T. Hofmann, M. Schubert, G. Leibiger, and V. Gottschalch, Appl. Phys. Lett. **90**, 182110 (2007).

[42] T. Hofmann, V. Darakchieva, B. Monemar, H. Lu, W. Schaff, and M. Schubert, Journal of Electronic Materials (2008).

[43] S. Schöche, J. Shi, A. Boosalis, P. Kühne, C. M. Herzinger, J. A. Woollam, W. J. Schaff, L. F. Eastman, M. Schubert, and T. Hofmann, Appl. Phys. Lett. **98**, 092103 (2011).

[44] T. Hofmann, C. M. Herzinger, J. L. Tedesco, D. K. Gaskill, J. A. Woollam, and M. Schubert, Thin Solid Films **519**, 2593 (2011), 5th International Conference on Spectroscopic Ellipsometry (ICSE-V).

[45] T. Hofmann, A. Boosalis, P. Kühne, C. M. Herzinger, J. A. Woollam, D. K. Gaskill, J. L. Tedesco, and M. Schubert, App. Phys. Lett. **98**, 041906 (2011).

[46] P. Kühne, T. Hofmann, C. M. Herzinger, and M. Schubert, Thin Solid Films **519**, 2613 (2011), 5th International Conference on Spectroscopic Ellipsometry (ICSE-V).

[47] M. Schubert, Annalen Der Physik **15**, 480 (2006).

[48] T. Hofmann, C. Herzinger, A. Boosalis, T. Tiwald, J. Woollam, and M. Schubert, Rev. Sci. Instrum. **81**, 023101 (2010).

[49] P. Kühne, V. Darakchieva, R. Yakimova, J. D. Tedesco, R. L. Myers-Ward, C. R. Eddy, D. K. Gaskill, C. M. Herzinger, J. A. Woollam, M. Schubert, and T. Hofmann, Phys. Rev. Lett. **111**, 077402 (2013).

[50] P. Hauge, Surf. Sci. **96**, 108 (1980).

[51] R. W. Collins, Rev. Sci. Instrum. **61**, 2029 (1990).

[52] M. Schubert, B. Rheinländer, J. A. Woollam, B. Johs, and C. M. Herzinger, J. Opt. Soc. Am. A **13**, 875 (1996).

[53] P. S. Hauge and F. H. Dill, Opt. Commun. **14**, 431 (1975).

[54] P. S. Hauge, Surf. Sci. **56**, 148 (1976).

[55] D. E. Aspnes and P. S. Hauge, J. Opt. Soc. Am. **66**, 949 (1976).

[56] P. S. Hauge, J. Opt. Soc. Am. **68**, 1519 (1978).

[57] J. Lee, J. Koh, and R. W. Collins, Review of Scientific Instruments **72**, 1742 (2001).

[58] R. W. Collins and J. Koh, J. Opt. Soc. Am. A **16**, 1997 (1999).

[59] C. Herzinger, S. Green, and B. Johs, 6,795,184 B1 (2004).

[60] P. Kühne, *The Optical-Hall Effect in Two- and Three-Dimensional Materials*, PhD thesis, University of Nebraska-Lincoln (2014), eTD collection for University of Nebraska - Lincoln. Paper AAI3618595.

[61] G. E. Jellison, Thin Solid Films **313-314**, 33 (1998).

[62] W. H. Press, *Numerical Recipes 3rd Edition: The Art of Scientific Computing*, (Cambridge University Press, 2007).

[63] C. M. Herzinger, H. Yao, P. G. Snyder, F. G. Celii, Y.-C. Kao, B. Ohs, and J. A. Woollam, J. Appl. Phys. **77**, 4677 (1995).

[64] C. M. Herzinger, P. G. Snyder, B. Johs, and J. A. Woollam, J. Appl. Phys. **77**, 1715 (1995).

[65] B. Johs, Thin Solid Films **234**, 395 (1993).

[66] R. G. Mazur and D. H. Dickey, Journal of The Electrochemical Society **113**, 255 (1966).

[67] G. Bracco and B. Holst, eds., *Surface Science Techniques*, (Springer, 2013).

[68] P. Bright, Ars Technica **July 15th** (2015).

[69] A. Schulze, A. Florakis, T. Hantschel, P. Eyben, A. S. Verhulst, R. Rooyackers, A. Vandooren, and W. Vandervorst, Applied Physics Letters **102**, 052108 (2013).

[70] A. Vandooren, D. Leonelli, R. Rooyackers, A. Hikavyy, K. Devriendt, M. Demand, R. Loo, G. Groeseneken, and C. Huyghebaert, Solid-State Electronics **83**, 50 (2013), selected Papers from the 6th International SiGe Technology and Device Meeting (ISTDM 2012).

[71] D. Schmidt, A. C. Kjerstad, T. Hofmann, R. Skomski, E. Schubert, and M. Schubert, J. Appl. Phys. **105**, 113508 (2009).

[72] D. Schmidt, B. Booso, T. Hofmann, E. Schubert, A. Sarangan, and M. Schubert, Appl. Phys. Lett. **94**, 011914 (2009).

[73] D. Schmidt, B. Booso, T. Hofmann, E. Schubert, A. Sarangan, and M. Schubert, Optics Letters **34**, 992 (2009).

[74] T. Hofmann, D. Schmidt, A. Boosalis, P. Kühne, R. Skomski, C. M. Herzinger, J. A. Woollam, M. Schubert, and E. Schubert, Appl. Phys. Lett. **99**, 081903 (2011).

[75] M. Herrmann, M. Tani, K. Sakai, and R. Fukasawa, J. Appl. Phys. **91**, 1247 (2002).

[76] M. van Exter and D. Grischkowsky, Appl. Phys. Lett. **56**, 1694 (1990).

[77] T. Tiwald, D. Thompson, J. Woollam, W. Paulson, and R. Hance, Thin Solid Films **313-314**, 661 (1998).

[78] T. E. Tiwald, D. W. Thompson, and J. A. Woollam, J. Vac. Sci. Technol. B **16**, 312 (1998).

[79] T. Hofmann, C. M. Herzinger, T. E. Tiwald, J. A. Woollam, and M. Schubert, Appl. Phys. Lett. **95**, 032102 (2009).

[80] N. Haegel and A. White, Infrared Phys. **29**, 915 (1989).

[81] P. E. Schmidt, M. Octavio, R. C. Callarotti, and H. K. Henisch, J. Appl. Phys. **53**, 4996 (1982).

[82] Z. T. Kuznicki, J. Appl. Phys. **69**, 6526 (1991).

[83] R. F. Pierret, *Semiconductor Device Fundamentals*, (Prentice Hall, 1996).

[84] T. Hofmann, C. M. Herzinger, C. Krahmer, K. Streubel, and M. Schubert, Phys. Status Solidi (a) **205**, 779 (2008).

[85] C. Jacoboni, C. Canali, G. Ottaviani, and A. A. Quaranta, Solid-State Electron. **20**, 77 (1977).

[86] M. Schubert, T. Hofmann, and J. Šik, Phys. Rev. B **71**, 35324 (2005).

[87] F. G. Allen and G. W. Gobeli, Phys. Rev. **127**, 150 (1962).

[88] T. Clarysse, P. De Wolf, H. Bender, and W. Vandervorst, Journal of Vacuum Science & Technology B **14**, 358 (1996).

[89] C. Berger, Z. Song, T. Li, X. Li, A. Y. Ogbazghi, R. Feng, Z. Dai, A. N. Marchenkov, E. H. Conrad, P. N. First, and W. A. de Heer, The Journal of Physical Chemistry B **108**, 19912 (2004).

[90] Y.-M. Lin, C. Dimitrakopoulos, K. A. Jenkins, D. B. Farmer, H.-Y. Chiu, A. Grill, and P. Avouris, Science **327**, 662 (2010).

[91] J. S. Moon, D. Curtis, S. Bui, M. Hu, D. K. Gaskill, J. L. Tedesco, P. Asbeck, G. G. Jernigan, B. L. VanMil, R. L. Myers-Ward, C. R. Eddy Jr., P. M. Campbell, and X. Weng, IEEE Electron Device Lett. **31**, 260 (2010).

[92] W. A. de Heer, C. Berger, X. Wu, P. N. First, E. H. Conrad, X. Li, T. Li, M. Sprinkle, J. Hass, M. L. Sadowski, M. Potemski, and G. Martinez, Solid State Commun. **143**, 92 (2007), exploring graphene - Recent research advances.

[93] K. I. Bolotin, K. J. Sikes, Z. Jiang, M. Klima, G. Fudenberg, J. Hone, P. Kim, and H. L. Stormer, Solid State Commun. **146**, 351 (2008).

[94] K. Bolotin, F. Ghahari, M. Shulman, H. Stormer, and P. Kim, Nature (2009).

[95] J. Heo, H. J. Chung, S.-H. Lee, H. Yang, D. H. Seo, J. K. Shin, U.-I. Chung, S. Seo, E. H. Hwang, and S. Das Sarma, Phys. Rev. B **84**, 035421 (2011).

[96] J. L. Tedesco, B. L. VanMil, R. L. Myers-Ward, J. M. McCrate, S. A. Kitt, P. M. Campbell, G. G. Jernigan, J. C. Culbertson, C. R. Eddy Jr., and D. Gaskill, Appl. Phys. Lett. **95**, 122102 (2009).

[97] D. W. Koon, Review of Scientific Instruments **60**, 271 (1989).

[98] J. L. Tedesco, G. G. Jernigan, J. C. Culbertson, J. K. Hite, Y. Yang, K. M. Daniels, R. L. Myers-Ward, C. R. Eddy, J. A. Robinson, K. A. Trumbull,

M. T. Wetherington, P. M. Campbell, and D. K. Gaskill, Appl. Phys. Lett. **96**, 222103 (2010).

[99] T. Hofmann, U. Schade, W. Eberhardt, C. M. Herzinger, P. Esquinazi, and M. Schubert, Rev. Sci. Instrum. **77**, 63902 (2006).

[100] C. M. Wolfe, N. Holonyak, and G. E. Stillmann, *Physical Properties of Semiconductors*, (Prentice Hall, New Jersey, 1989).

[101] C. Pidgeon, in *Handbook on Semiconductors*, edited by M. Balkanski (North-Holland, Amsterdam, 1980).

[102] M. K. Yakes, D. Gunlycke, J. L. Tedesco, P. M. Campbell, R. L. Myers-Ward, C. R. Eddy, D. K. Gaskill, P. E. Sheehan, and A. R. Laracuente, Nano Lett. **10**, 1559 (2010).

[103] T. E. Tiwald, J. A. Woollam, S. Zollner, J. Christiansen, R. B. Gregory, T. Wetteroth, S. R. Wilson, and A. R. Powell, Phys. Rev. B **60**, 11464 (1999).

[104] L. Patrick and W. J. Choyke, Phys. Rev. B **2**, 2255 (1970).

[105] Y. Peng, X. Xu, X. Hu, K. Jiang, S. Song, Y. Gao, and H. Xu, J. Appl. Phys. **107**, 093519 (2010).

[106] Y.-M. Lin, C. Dimitrakopoulos, D. B. Farmer, S.-J. Han, Y. Wu, W. Zhu, D. K. Gaskill, J. L. Tedesco, R. L. Myers-Ward, J. Charles R. Eddy, A. Grill, and P. Avouris, Appl. Phys. Lett. **97**, 112107 (2010).

[107] R. R. Nair, P. Blake, A. N. Grigorenko, K. S. Novoselov, T. J. Booth, T. Stauber, N. M. R. Peres, and A. K. Geim, Science **320**, 1308 (2008).

[108] F. Zhang, B. Sahu, H. Min, and A. H. MacDonald, Phys. Rev. B **82**, 035409 (2010).

[109] K. Rodenhausen and M. Schubert, Thin Solid Films **519**, 2772 (2011), 5th International Conference on Spectroscopic Ellipsometry (ICSE-V).

[110] P. N. First, W. A. de Heer, T. Seyller, C. Berger, J. A. Stroscio, and J.-S. Moon, MRS Bull. **35**, 296 (2010).

[111] J. Hass, R. Feng, J. E. Millán-Otoya, X. Li, M. Sprinkle, P. N. First, W. A. de Heer, E. H. Conrad, and C. Berger, Phys. Rev. B **75**, 214109 (2007).

[112] K. V. Emtsev, A. Bostwick, K. Horn, J. Jobst, G. L. Kellogg, L. Ley, J. L. McChesney, T. Ohta, S. A. Reshanov, J. Rohrl, E. Rotenberg, A. K. Schmid, D. Waldmann, H. B. Weber, and T. Seyller, Nature Mat. **8**, 203 (2009).

[113] F. Hiebel, P. Mallet, F. Varchon, L. Magaud, and J.-Y. Veuillen, Phys. Rev. B **78**, 153412 (2008).

[114] P. Yu and M. Cardona, *Fundamentals of Semiconductors*, (Springer, Berlin, 1999).

[115] E. A. Taft and H. R. Philipp, Phys. Rev. **138**, A197 (1965).

[116] V. G. Kravets, A. N. Grigorenko, R. R. Nair, P. Blake, S. Anissimova, K. S. Novoselov, and A. K. Geim, Phys. Rev. B **81**, 155413 (2010).

[117] J. W. Weber, V. E. Calado, and M. C. M. van de Sanden, Appl. Phys. Lett. **97**, 091904 (2010).

[118] F. J. Nelson, V. K. Kamineni, T. Zhang, E. S. Comfort, J. U. Lee, and A. C. Diebold, App. Phys. Lett. **97**, 253110 (2010).

[119] R. Yakimova, C. Virojanadara, D. Gogova, M. Syväjärvi, D. Siche, K. Larsson, and L. I. Johansson, Mat. Sci. Forum **645**, 565 (2010).

[120] R. Vasiliauskas, M. Marinova, M. Syväjärvi, R. Liljedahl, G. Zoulis, J. Lorenzzi, G. Ferro, S. Juillaguet, J. Camassel, E. Polychroniadis, and R. Yakimova, Journal of Crystal Growth **324**, 7 (2011).

[121] S. Logothetidis and J. Petalas, **80**, 1768 (1996).

[122] S. Zollner, J. G. Chen, E. Duda, T. Wetteroth, S. R. Wilson, and J. N. Hilfiker, **85**, 8353 (1999).

[123] O. P. A. Lindquist, K. Järrendahl, S. Peters, J. T. Zettler, C. Cobet, N. Esser, D. E. Aspnes, A. Henry, and N. V. Edwards, **78**, 2715 (2001).

[124] A. Charrier, A. Coati, T. Argunova, F. Thibaudau, Y. Garreau, R. Pinchaux, I. Forbeaux, J.-M. Debever, M. Sauvage-Simkin, and J.-M. Themlin, Journal of Applied Physics **92**, 2479 (2002).

[125] G. M. Rutter, N. P. Guisinger, J. N. Crain, E. A. A. Jarvis, M. D. Stiles, T. Li, P. N. First, and J. A. Stroscio, Phys. Rev. B **76**, 235416 (2007).

[126] J. Hass, F. Varchon, J. E. Millán-Otoya, M. Sprinkle, N. Sharma, W. A. de Heer, C. Berger, P. N. First, L. Magaud, and E. H. Conrad, Phys. Rev. Lett. **100**, 125504 (2008).

[127] L. Yang, J. Deslippe, C.-H. Park, M. L. Cohen, and S. G. Louie, Phys. Rev. Lett. **103**, 186802 (2009).

[128] V. Darakchieva, A. Boosalis, A. A. Zakharov, T. Hofmann, M. Schubert, T. E. Tiwald, T. Iakimov, R. Vasiliauskas, and R. Yakimova, Applied Physics Letters **102**, 213116 (2013).

[129] J. Wagner and P. Lautenschlager, Journal of Applied Physics **59**, 2044 (1986).

[130] P. E. Trevisanutto, M. Holzmann, M. Côté, and V. Olevano, Phys. Rev. B **81**, 121405 (2010).

[131] F. M. D. Pellegrino, G. G. N. Angilella, and R. Pucci, Phys. Rev. B **81**, 035411 (2010).

[132] F. Varchon, R. Feng, J. Hass, X. Li, B. N. Nguyen, C. Naud, P. Mallet, J.-Y. Veuillen, C. Berger, E. H. Conrad, and L. Magaud, Phys. Rev. Lett. **99**, 126805 (2007).

[133] B. L. VanMil, R. L. Myers-Ward, J. L. Tedesco, C. R. E. Jr., G. G. Jernigan, J. C. Culbertson, P. M. Campbell, J. McCrate, S. Kitt, and D. K. Gaskill, Materials Science Forum **615 - 617**, 211 (2009).

[134] C. A. Coulson, Nature **159**, 265 (1947).

[135] P. R. Wallace, Phys. Rev. **71**, 622 (1947).

[136] G. E. Jellison, J. D. Hunn, and H. N. Lee, Phys. Rev. B **76**, 085125 (2007).

[137] D. L. Greenaway, G. Harbeke, F. Bassani, and E. Tosatti, Phys. Rev. **178**, 1340 (1969).

[138] G. S. Painter and D. E. Ellis, Phys. Rev. B **1**, 4747 (1970).

[139] L. G. Johnson and G. Dresselhaus, Phys. Rev. B **7**, 2275 (1973).

[140] R. Klucker, M. Skibowski, and W. Steinmann, physica status solidi (b) **65**, 703 (1974).

[141] A. Zunger, Phys. Rev. B **17**, 626 (1978).

[142] R. C. Tatar and S. Rabii, Phys. Rev. B **25**, 4126 (1982).

[143] R. Ahuja, S. Auluck, J. M. Wills, M. Alouani, B. Johansson, and O. Eriksson, Phys. Rev. B **55**, 4999 (1997).

[144] T. G. Pedersen, Phys. Rev. B **67**, 113106 (2003).

[145] A. G. Marinopoulos, L. Reining, A. Rubio, and V. Olevano, Phys. Rev. B **69**, 245419 (2004).

[146] H. Venghaus, physica status solidi (b) **71**, 609 (1975).

[147] A. Boosalis, T. Hofmann, V. Darakchieva, R. Yakimova, and M. Schubert, Applied Physics Letters **101**, 011912 (2012).

[148] D.-H. Chae, T. Utikal, S. Weisenburger, H. Giessen, K. v. Klitzing, M. Lippitz, and J. Smet, Nano Letters **11**, 1379 (2011).

[149] K. F. Mak, J. Shan, and T. F. Heinz, Phys. Rev. Lett. **106**, 046401 (2011).

[150] L. Benfatto, S. G. Sharapov, and J. P. Carbotte, Phys. Rev. B **77**, 125422 (2008).

[151] A. B. Kuzmenko, E. van Heumen, F. Carbone, and D. van der Marel, Phys. Rev. Lett. **100**, 117401 (2008).

[152] M. Bruna and S. Borini, Applied Physics Letters **94**, 031901 (2009).

[153] D. E. Sheehy and J. Schmalian, Phys. Rev. B **80**, 193411 (2009).

[154] A. Boosalis, T. Hofmann, V. Darakchieva, R. Yakimova, T. Tiwald, and M. Schubert, MRS Proceedings **1407** (2012).

[155] A. Boosalis, R. Elmquist, M. Real, N. Nguyen, M. Schubert, and T. Hofmann, MRS Proceedings **1505** (2013).

[156] W. Li, A. Boosalis, N. Nguyen, and D. Gundlach, App. Phys. Lett. **In Preparation.** (2014).

[157] C. C. Kim, J. W. Garland, H. Abad, and P. M. Raccah, Phys. Rev. B **45**, 11749 (1992).

[158] J. Weideman, SIAM J. Numer. Anal. **31**, 1497 (1994).

[159] U. Fano, Phys. Rev. **124**, 1866 (1961).

[160] R. J. Elliott, Phys. Rev. **108**, 1384 (1957).

[161] S. Adachi, Phys. Rev. B **41**, 1003 (1990).

[162] B. Feuerbacher and B. Fitton, Phys. Rev. Lett. **26**, 840 (1971).

[163] J.-C. Charlier, X. Gonze, and J.-P. Michenaud, Phys. Rev. B **43**, 4579 (1991).

[164] A. Grüneis, C. Attaccalite, L. Wirtz, H. Shiozawa, R. Saito, T. Pichler, and A. Rubio, Phys. Rev. B **78**, 205425 (2008).

[165] K. S. Novoselov, D. Jiang, F. Schedin, T. J. Booth, V. V. Khotkevich, S. V. Morozov, and A. K. Geim, Proceedings of the National Academy of Sciences of the United States of America **102**, 10451 (2005).

[166] A. Bostwick, T. Ohta, T. Sellyer, K. Horn, and E. Rotenberg, Nat. Phys. **3**, 36 (2007).

[167] A. Bostwick, T. Ohta, J. L. McChesney, T. Seyller, K. Horn, and E. Rotenberg, Solid State Communications **143**, 63 (2007), exploring graphene Recent research advances.

[168] A. H. Castro Neto, F. Guinea, N. M. R. Peres, K. S. Novoselov, and A. K. Geim, Rev. Mod. Phys. **81**, 109 (2009).

[169] A. Gray, M. Balooch, S. Allegret, S. De Gendt, and W.-E. Wang, Journal of Applied Physics **104**, 053109 (2008).

[170] N. Ferralis, R. Maboudian, and C. Carraro, Phys. Rev. Lett. **101**, 156801 (2008).

[171] R. M. Ribeiro, V. M. Pereira, N. M. R. Peres, P. R. Briddon, and A. H. C. Neto, New Journal of Physics **11**, 115002 (2009).

[172] G. E. Jellison and F. A. Modine, Applied Physics Letters **69**, 371 (1996).

[173] R. Kitamura, L. Pilon, and M. Jonasz, Appl. Opt. **46**, 8118 (2007).

[174] S. Zollner, W. Qin, R. B. Gregory, N. V. Edwards, K. Junker, and T. E. Tiwald, Journal of Applied Physics **101**, 053522 (2007).

[175] S. Ergun, Nature **213**, 135 (1967).

[176] Y. Koike, S. Morita, T. Nakanomyo, and T. Fukase, Journal of the Physical Society of Japan **54**, 713 (1985).

[177] K. F. Mak, J. Shan, and T. F. Heinz, Phys. Rev. Lett. **104**, 176404 (2010).

[178] T. G. Pedersen, A.-P. Jauho, and K. Pedersen, Phys. Rev. B **79**, 113406 (2009).

[179] D. D. S. Meneses, G. Gruener, M. Malki, and P. Echegut, Journal of Non-Crystalline Solids **351**, 124 (2005).

[180] H. Ehrenreich and M. H. Cohen, Phys. Rev. **115**, 786 (1959).

[181] V. Ariel and A. Natan, arXiv **1201.6100** (2012).

[182] T. Fang, A. Konar, H. Xing, and D. Jena, Applied Physics Letters **91**, 092109 (2007).

[183] V. M. Pereira, A. H. Castro Neto, and N. M. R. Peres, Phys. Rev. B **80**, 045401 (2009).

[184] C. Berger, Z. Song, X. Li, X. Wu, N. Brown, C. Naud, D. Mayou, T. Li, J. Hass, A. N. Marchenkov, E. H. Conrad, P. N. First, and W. A. de Heer, Science **312**, 1191 (2006).

[185] Y.-M. Lin, H.-Y. Chiu, K. A. Jenkins, D. B. Farmer, P. Avouris, and A. Valdes-Garcia, IEEE Electron. Device Letters **31**, 68 (2010).

[186] Y.-M. Lin, A. Valdes-Garcia, S.-J. Han, D. B. Farmer, I. Meric, Y. Sun, Y. Wu, C. Dimitrakopoulos, A. Grill, P. Avouris, and K. A. Jenkins, Science **332**, 1294 (2011).

[187] Y. Wu, K. A. Jenkins, A. Valdes-Garcia, D. B. Farmer, Y. Zhu, A. A. Bol, C. Dimitrakopoulos, W. Zhu, F. Xia, P. Avouris, and Y.-M. Lin, Nano Lett. **12**, 3062 (2012).

[188] X. Weng, J. A. Robinson, K. Trumbull, R. Cavalero, M. A. Fanton, and D. Snyder, Applied Physics Letters **100**, 031904 (2012).

[189] I. Santoso, P. K. Gogoi, H. B. Su, H. Huang, Y. Lu, D. Qi, W. Chen, M. A. Majidi, Y. P. Feng, A. T. S. Wee, K. P. Loh, T. Venkatesan, R. P. Saichu, A. Goos, A. Kotlov, M. Rübhausen, and A. Rusydi, Phys. Rev. B **84**, 081403 (2011).

[190] W. Strupinski, K. Grodecki, A. Wysmolek, R. Stepniewski, T. Szkopek, P. E. Gaskell, A. GrÃijneis, D. Haberer, R. Bozek, J. Krupka, and J. M. Baranowski, Nano Letters **11**, 1786 (2011), pMID: 21438581.

[191] M. Zhou, F. L. Pasquale, P. A. Dowben, A. Boosalis, M. Schubert, V. Darakchieva, R. Yakimova, L. Kong, and J. A. Kelber, Journal of Physics: Condensed Matter **24**, 072201 (2012).

[192] M. Losurdo, M. M. Giangregorio, P. Capezzuto, and G. Bruno, The Journal of Physical Chemistry C **115**, 21804 (2011).

[193] U. Wurstbauer, C. RÃűling, U. Wurstbauer, W. Wegscheider, M. Vaupel, P. H. Thiesen, and D. Weiss, Applied Physics Letters **97**, 231901 (2010).

[194] A. Matkovic, A. Beltaos, M. Milicevic, U. Ralevic, B. Vasic, and R. Gajic, Journal of Applied Physics **112**, 123523 (2012).

[195] H. Hibino, H. Kageshima, F. Maeda, M. Nagase, Y. Kobayashi, and H. Yamaguchi, Phys. Rev. B **77**, 075413 (2008).

[196] N. Savvides, Journal of Applied Physics **59**, 4133 (1986).

[197] N. Camara, G. Rius, J.-R. Huntzinger, A. Tiberj, L. Magaud, N. Mestres, P. Godignon, and J. Camassel, Applied Physics Letters **93**, 263102 (2008).

[198] R. Vasiliauskas, S. Juillaguet, M. SyvÃďjÃďrvi, and R. Yakimova, Journal of Crystal Growth **348**, 91 (2012).

List of Own Publications

The following articles have been published, submitted, or are in preparation for publication. References of these articles are partially included in the Bibliography.

[1] A. Boosalis, N. Nguyen, W. Li, R. Synowicki, T. Hofmann, and M. Schubert *"A Tight-Binding Band Structure Based Model Dielectric Function for Graphene and HOPG"*, Phys. Rev. B, *in preparation* (2015).

[2] R. Yakimova, T. Iakimov, G.R. Yazdi, C. Bouhafs, J. Eriksson, A. Zakharov, A. Boosalis, M. Schubert, and V. Darakchieva, *"Morphological and Electronic Properties of Epitaxial Graphene on SiC"*, 5th South African Conference on Photonic Materials (SACPM 2013), Physica B: Condensed Matter **439**, 54 (2014).

[3] P. Kühne, A. Boosalis, C. M. Herzinger, L. Nyakiti, V. Wheeler, R. Myers-Ward, C. J. Eddy, D. Gaskill, M. Schubert und T. Hofmann, *"Optical Hall Effect Measurement of Coupled Phonon Mode - Landau Level Transitions in Epitaxial Graphene on Silicon Carbide"*, MRS Proceedings **1505** (2013).

[4] V. Darakchieva, A. Boosalis, A. A. Zakharov, T. Hofmann, M. Schubert, T. E. Tiwald, T. Iakimov, R. Vasiliauskas, and R. Yakimova, *"Large-area Microfocal Spectroscopic Ellipsometry Mapping of Thickness and Electronic Properties of Epitaxial Graphene on Si- and C-face of 3C-SiC(111)"*, Appl. Phys. Lett. **102**, 213116 (2013).

[5] A. Boosalis, R. Elmquist, M. Real, N. Nguyen, M. Schubert, and T. Hofmann, *"A Model Dielectric Function for Graphene from the Infrared to the Ultraviolet"*, MRS Proceedings **1505** (2013).

[6] R. Yan, Q. Zhang, O. Kirillov, W. Li, J. Basham, A. Boosalis, X. Liang, D. Jena, C. Richter, A. Seabaugh, D. Gundlach, H. Xing, and N. V. Nguyen, *"Graphene as a Transparent Electrode for Direct Observation of Hole Photoemission from Silicon to Oxide"*, Appl. Phys. Lett. **102**, 123106 (2013).

[7] M. Zhou, F. Pasquale, P. Dowben, A. Boosalis, M. Schubert, V. Darakchieva, R. Yakimova, L. Kong, J. Kelber, *"Direct Graphene Growth on Co_3O_4 (111) by Molecular Beam Epitaxy"*, J. Phys.: Condens. Matter **24**, 072201 (2012).

[8] T. Hofmann, D. Schmidt, A. Boosalis, P. Kühne, C. Herzinger, J. Woollam, E. Schubert und M. Schubert, *"Metal Slanted Columnar Thin Film THz Optical Sensors"*, MRS Proceedings **1409** (2012).

[9] A. Boosalis, T. Hofmann, V. Darakchieva, R. Yakimova, T. Tiwald, M. Schubert, *"Spectroscopic Mapping Ellipsometry of Graphene Grown on 3C SiC"*, MRS Proceedings **1407** (2012).

[10] A. Boosalis, T. Hofmann, V. Darakchieva, R. Yakimova, and M. Schubert, *"Visible to Vacuum Ultraviolet Dielectric Functions of Epitaxial Graphene on 3C and 4H SiC Polytypes Determined by Spectroscopic Ellipsometry"*, Appl. Phys. Lett. **101**, 011912 (2012).

[11] T. Hofmann, A. Boosalis, P. Kühne, C. M. Herzinger, J. A. Woollam, D. K. Gaskill, J. L. Tedesco und M. Schubert, *"Hole-channel Conductivity in Epitaxial Graphene Determined by Terahertz Optical Hall-effect and Midinfrared Ellipsometry"*, Applied Physics Letters **98**, 041906 (2011).

[12] T. Hofmann, D. Schmidt, A. Boosalis, P. Kühne, R. Skomski, C. M. Herzinger, J. A. Woollam, M. Schubert und E. Schubert, *"THz Dielectric Anisotropy of Metal Slanted Columnar Thin Films"*, Appl. Phys. Lett. **99**, 081903 (2011).

[13] S. Schöche, J. Shi, A. Boosalis, P. Kühne, C. M. Herzinger, J. A. Woollam, W. J. Schaff, L. F. Eastman, M. Schubert, and T. Hofmann, *"Terahertz Optical Hall Effect Characterization of Two-Dimensional Electron Gas Properties in AlGaN/GaN High Electron Mobility Transistor Structures"*, Appl. Phys. Lett. **98**, 092103 (2011).

[14] A. Boosalis, T. Hofmann, J. Šik, and M. Schubert, *"Free-charge Carrier Profile of Iso- and Aniso-type Si Homojunctions Determined by Terahertz and Mid-infrared Ellipsometry"*, 5th International Conference on Spectroscopic Ellipsometry (ICSE-V), Thin Solid Films **519**, 2604 (2011).

[15] T. Hofmann, C. M. Herzinger, A. Boosalis, T. Tiwald, J. A. Woollam, and M. Schubert, *"Variable-wavelength Frequency-domain Terahertz Ellipsometry"*, Rev. Sci. Instrum. **81**, 023101-7 (2010).